2017-01-01

Electronic Structure Studies On Transition Metal Containing Endohedral Fullerenes, Carbon Onions And Zinc Sulfide Cages

Shusil Bhusal
University of Texas at El Paso, sbhusal@miners.utep.edu

ELECTRONIC STRUCTURE STUDIES ON TRANSITION METAL CONTAINING ENDOHEDRAL FULLERENES, CARBON ONIONS AND ZINC SULFIDE CAGES

SHUSIL BHUSAL

Doctoral Program in Materials, Science and Engineering

APPROVED:

Rajendra Zope, Ph.D., Chair

Tunna Baruah, Ph.D., Co-Chair

Devesh Misra, Ph.D.

Charles H. Ambler, Ph.D.
Dean of the Graduate School

Dedication

I dedicate my thesis work to my family. A special feeling of gratitude to my grandparents, Beduram Bhusal and Shubhadra Bhusal, my parents Dharma Bhusal and Ganga Bhusal, my wife Namuna Ghimire and my brothers Surya Bhusal and Nirmal Bhusal whose words of encouragement and push for tenacity ring in my ears.

ELECTRONIC STRUCTURE STUDIES ON TRANSITION METAL CONTAINING ENDOHEDRAL FULLERENES, CARBON ONIONS AND ZINC SULFIDE CAGES

by

SHUSIL BHUSAL, Ph.D.

DISSERTATION

Presented to the Faculty of the Graduate School of

The University of Texas at El Paso

in Partial Fulfillment

of the Requirements

for the Degree of

DOCTOR OF PHILOSOPHY

Materials, Science and Engineering

THE UNIVERSITY OF TEXAS AT EL PASO

December 2017

Acknowledgements

I would like to express my deepest appreciation to my committee chair, Dr. Rajendra Zope and committee member Dr. Tunna Baruah, who provided valuable help through every step of my study and research, making my scientific background stronger. Without their great support and guidance this dissertation would not have been possible.

I would also like to thank my committee member Dr. Devesh Misra for providing me his valuable time and great help.

In addition, a sincere thank to Dr. Luis Basurto and Dr. Yoh Yamamoto, who helped me a lot in this work. I also thank to Nakul Karle for the vibrational plots. I would also like to acknowledge the office of basic sciences, department of energy and department of physics for the financial support.

Abstract

We present the most stable structures for $V_XSc_{3-X}N@C_{2n}$ (where X=1-3 and 2n=70, 76, 78 and 80) using a systematic procedure that involves all possible isomers of the host fullerene cages. Subsequently, a detailed investigation of structural and electronic properties of the lowest energy isomers is performed using density functional theory in combination with large polarized Gaussian basis sets. The search procedure developed involved structural optimizations of thousands of fullerenes and correctly identifies the experimentally observed $VSc_2N@C_{80}$ and $V_2ScN@C_{80}$ isomer as the most stable structures. The structural analysis shows that a few V-doped endohedral fullerenes do not follow the isolated pentagon rule that dictates the stability of fullerenes. The V-doped fullerenes show interesting electronic and magnetic properties. We have also studied the electronic structure studies on $C_{60}@C_{240}$ onion at the DFT level using all electrons and large polarized Gaussian basis sets. The calculations indicate that the two nested fullerenes are weekly interacting and their electronic structure is essentially unperturbed. From the observed values of electron affinity and ionization potential, it can be inferred that the onion has not only high electron accepting capacity but also is rather stable against oxidation. We also present a density functional study on the structural and electronic properties of Zinc Sulfide cages Zn_xS_x [x = 12, 16, 24, 28, 36, 48, 108] and an onion-like structure $Zn_{96}S_{96}$. The study of energetics and stability, performed using large polarized Gaussian basis sets indicated that all structures to be energetically stable with similar binding energy of 5.5 - 5.6 eV per ZnS pair. Further computation of electronic properties showed that these cages have large vertical ionization energies and relatively low electron affinities in the range of 6.8-8.1 eV, and 1.7-3.0 eV, respectively. They have large HOMO-LUMO gaps between 2.5 to 3.3 eV and quasi-particle gaps vary from 6.2 eV for $Zn_{12}S_{12}$ to 4.19 for $Zn_{108}S_{108}$. The computed vibrational frequencies for

selected cages, i.e. $Zn_{12}S_{12}$, $Zn_{16}S_{16}$, $Zn_{28}S_{28}$ (O, S_4, and S_8 point groups), and $Zn_{36}S_{36}$ indicate that these cage structures correspond to local minima on the potential energy surface. Finally, the infrared spectra calculated using large basis sets is also reported.

Table of Contents

List of Tables

List of Figures

Chapter 1: Introduction

1.1 Endohedral Fullerenes

The carbon cages can serve as a robust container to accommodate some units inside it and the cages impregnated with the units like atoms, molecules and clusters are termed as endohedral fullerenes. Depending on the types of incorporated units, the endofullerenes can be classified as metal doped and non-metal doped fullerenes. Just after the great discovery of Buckminsterfullerene C_{60} in 1985 by Smalley and his group, the endohedral fullerene La@C_{60} was synthesized for the first time in the same year by the same group [1]. They used the laser vaporization of $LaCl_3$ along with graphite rod. Couple of years later, the endohedral nature of the metal atom in the endohedral fullerene was further illustrated by Weiss et al. from the indirect evidence in which they pointed out non reactive nature of LaC_{60} with H_2, O_2, NH_3 etc. [2] The deeper exploration on the endohedral fullerenes became possible only after the yield of fullerenes in macroscopic amount by Huffman and Kroto group in 1990 [3], in which they synthesized using resistive heating of graphite rod in He atmosphere.

Since then many reports of encapsulation of metal inside fullerenes and their properties were documented. [4] [5] [6] [7] [8] [9] [10] Still, the production of endohedral fullerenes was low and was about only 1% of the total production of empty cages of fullerenes. Some of the most promising synthesis methods are: vaporization of graphite using either of the method like laser ablation, arc discharge, plasma torch etc., implantation of the endohedral unit by breaking the wall of fullerene cage using one of the techniques: pressure treatment, bombardment of ions, explosion etc., and impregnation of endohedral unit using chemical path. [11] [12] [13] [14] [15] [16] . Among the methods mentioned above, more often, two synthesis methods: DC arc-discharge [17] and laser

vaporization method [18] [4] [19] are used, which are also known to generate the empty fullerenes equal importantly.

1.1.1 Synthesis Methods of Endohedral Fullerenes

In the laser-furnace method (Figure-1.1), laser is focused on a target rod which is composed of graphite/metal oxide in the high temperature furnace at 1200 °C. The target composite rod keeps on rotating to ensure a fresh surface under gas flow. Both Metallo-fullerenes and empty fullerenes are produced by the laser vaporization and flow down the tube along with the gas carrier and are finally trapped on the quartz tube wall near the end of the furnace. This method is known to have some characteristic advantages in terms of independent control over some of the physical parameters such as: reaction region temperature, gas pressure (i.e. He, Ar gas), laser fluence, etc. [18] and best suited to study the growth mechanism of the fullerenes and metallofullerenes but it is not cost effective due to the use of expensive laser source.

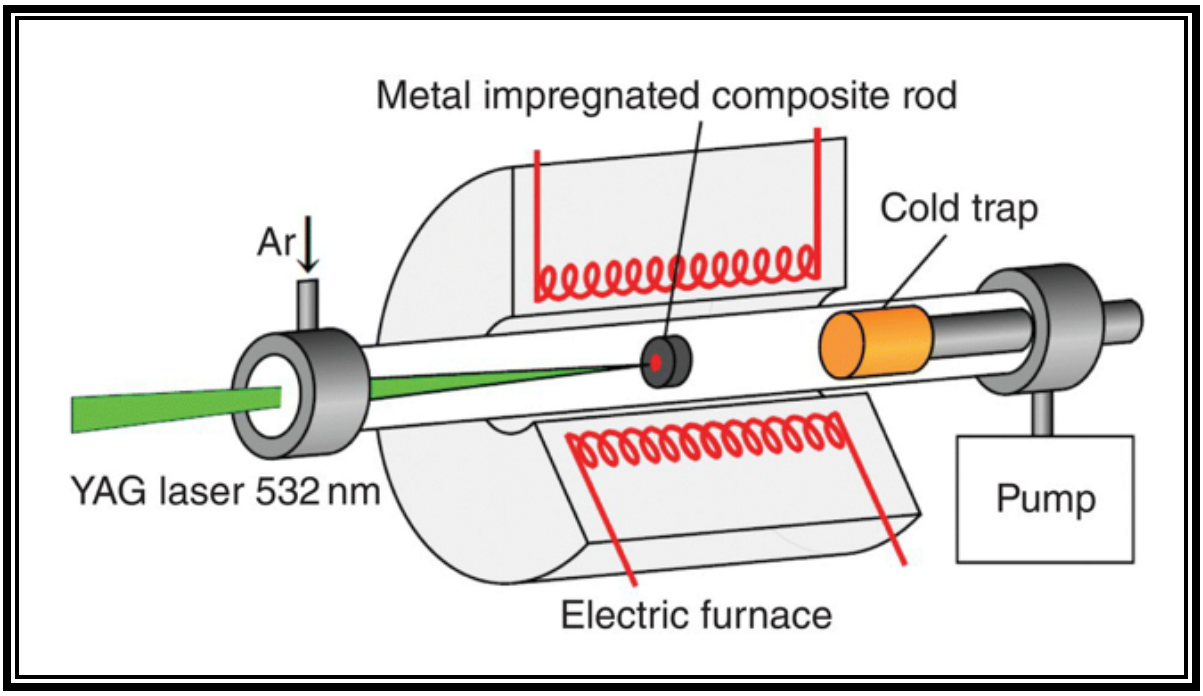

Figure 1.1: Schematic diagram of the high-temperature laser-furnace apparatus to produce fullerenes and metallofullerenes by laser vaporization of a rotating metal-impregnated graphite target in an electric furnace with flowing argon carrier gas. [20]

Dc arc discharge method is known for simple and higher production, which makes it a good bargain. It mainly consists of two chambers: production chamber and collection chamber. The anaerobic condition is preferred in the collection chamber in order to avoid the degradation of metallofullerenes in the primary soot due to moisture and air. The anode made up of metal-oxide/graphite composite treated at high temperature (i.e. above 1600 degree centigrade) lead to form the metal carbide, which is crucial in the efficient yield of the endohedral metallofullerenes. The yield can be further optimized using the variables such as: size of composite rod, DC current, and the arc gap of the two electrodes. [21] [22] A cross-sectional view of the third-generation DC arc- discharge apparatus is as shown in Figure-1.2.

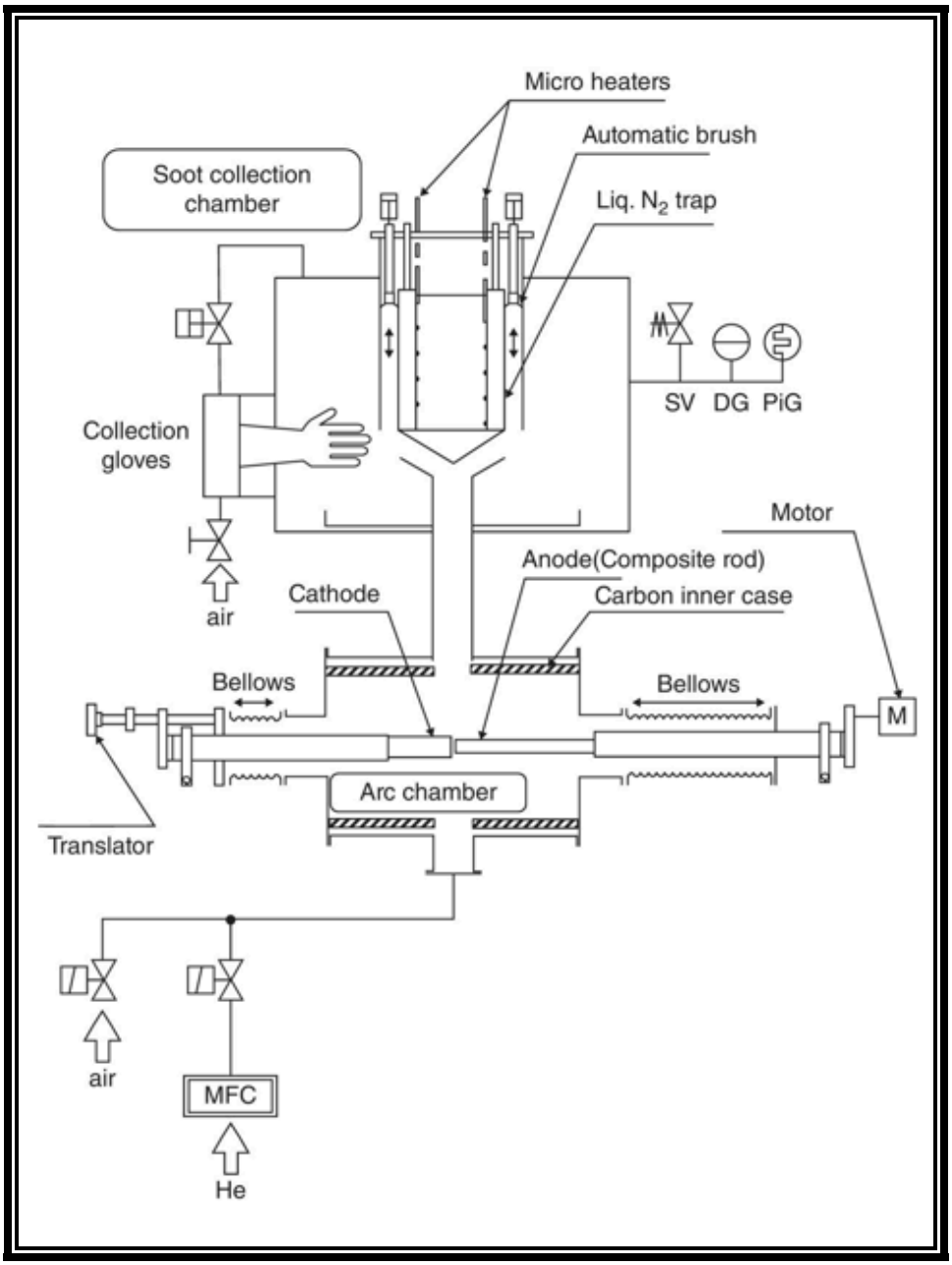

Figure 1.2: A cross-sectional view of the third-generation DC arc-discharge apparatus (the so-called Nagoya arc-discharge model) with an anaerobic collection and sampling mechanism. The produced metallofullerene-containing soot is effectively trapped by the liquid N_2 trap installed in the center of the collection chamber. Typical arc-discharge conditions: 40–100 Torr He flow, 300–500 A, and 25–30 V. [20]

The most important breakthrough in the metallofullerenes community was obtained with the inadvertently produced nitrite cluster fullerene $Sc_3N@C_{80}$, due to the leakage of N_2 gas in the Kratschmer Huffman arc generator, which greatly enhances the yield of endofullerene as reported by Harry Dorn and coworkers in 1999. The higher kinetic stability obtained from the opening of gap between the highest occupied molecular orbital (HOMO) and lowest unoccupied molecular orbital (LUMO) makes this nitride cluster fullerenes (NCFs) as a one of the most abundant fullerene after C_{60} and C_{70}. The leakage of nitrogen gas in the Kratschmer-Huffman generator, which was used for the vaporization of graphite, greatly enhances the yield of endohedral fullerene 3-5% [23]. Later on, this method was further refined and reactive gas atmosphere route gave a breakthrough, which pushes the relative yield of endohedral fullerenes overwhelmingly above 98%, even as compared with empty cages of fullerene for the first time [24].

1.1.2 Separation and Purification of Endohedral Fullerenes

In order to use in different applications, the endohedral fullerenes obtained from any of the synthesis method described above, need to be separated from the following: reactant species, by-products, and even from empty cages of fullerenes. Prominent solubility of the empty cages and endohedral fullerenes in some of the organic solvents established the solvent extraction method as one of the attractive methods in the first step of the separation from the soot, in which both pristine fullerenes and metallofullerenes are dissolved in solvents i.e. toluene, o-xylene, CS_2, pyridine and $_{1,2,4}$-trichlorobenzene etc. [25] [26] and is claimed to be best suited for the large scale extraction of fullerenes. The efficiency of solvent extraction can be increased using ultrasonic method. [27]

For the solvent free extraction of endohedral fullerenes, sublimation technique can be employed in which the raw soot containing metallofullerenes is heated at 400 °C in the He/vacuum environment and the sublimed metallofullerenes were collected in the cold trap leaving behind the primary soot.[28] [29] [30]

High performance liquid chromatography (HPLC) is one of the popular techniques for purification of both empty cages fullerenes and metallofullerenes, which utilizes difference in properties like: molecular weight, shape, size, boiling point, polarity, etc., between the separating groups and is claimed to be best suited for complete separation of endohedral metallofullerenes [31] [32]. The HPLC can also be employed to separate the structural isomers of the metallofullerenes.[33]

1.1.4 Potential Applications of Endohedral Fullerenes

Some of the attractive properties with potential use in different applications make the fullerenes and endohedral fullerenes as a one of the active areas of research. One of the attractive properties is the non-toxic behavior of carbon cage and the encaged atom, molecule or clusters are isolated from its surrounding environment makes the whole endohedral complex less toxic with higher stability and thus the endohedral fullerene based drugs are worthwhile in the medical applications[34]. In addition to non-toxic behavior, the large surface area in the cage also provides enough space to attach large number of drug molecules, which leads to the less amount of material requirement for effective dosing as compared to the conventional methods. Magnetic resonance imaging (MRI) is one of the popular methods that can be used to get the picture of organs. By the use of contrasting agents, it is possible to increase visibility of internal structures. Gadolinium based endohedral fullerenes are more common in use as contrasting agents, which were reported in various studies [35] [36] [33], in which its better performance is claimed with higher

relaxivities as compared with commercial MRI contrasting agent Gd-DTPA (DTPA diethylenetriamino-pentaacetic acid). In addition, endohedral fullerenes are also useful in the X-ray contrasting agent and anticancer activity [37] [38] [39]. Another attractive field of application is the use of endohedral fullerene as an acceptor component in the organic solar cell (OSC). The interest in OSC increased due to its low cost in manufacturing, ease in the fabrication, and compatibility with mass printing technique. One of the studies revealed that due to better-positioned LUMO level in an acceptor component $Lu_3N@C_{80}$-PCBH, which combined with low band gap donor polymer in polymeric solar cells was able to attain the efficiency over 10% [40].

1.1.4 Stability of Endohedral Fullerenes

In addition to NCFs, other endohedral fullerenes with novel units such as: metal carbide, methano-, oxide-, cyano-, sulfide-metal clusters were also reported in the various studies [41] [42] [43] [44]. This novel carbon material is reported to stabilize even some of the species mentioned above that cannot exist outside of the cage. The stability of the fullerenes is driven by the IPR rule. This rule is strictly followed by the empty cage fullerenes, and it grants the stability to only those fullerenes in which all the pentagonal sides are shared by hexagons. We point out that it is not possible for the C_{20}-C_{58}, C_{62}-C_{68} cages to satisfy the isolated pentagon rule. These carbon cages have high strain, and as a result, are unstable and difficult to isolate. In the endohedral form, however, the complexation releases large strain energy, which leads to form the stable structures. Before 2000, it was believed that only IPR fullerenes can be realized, but after the isolation of non IPR $Sc_2@C_{66}$ (4348) and $Sc_3N@C_{68}$ (6140) structures, interest grew over the non IPR fullerenes, as well. [45] [46]. An elucidation on stabilization of the endohedral fullerenes is reported by Salina et al. who proposed that there is change in aromaticity of the pentalene (two fused

pentagons) system moving from neutral to charged state. [47] This gain in aromaticity, due to charge transfer from endohedral moiety to the cage, enhances the stability of the whole complex.

As we have seen from the above discussion, the endohedral fullerene class is diverse in terms of isomers and selectivity of the endohedral unit. There are many theoretical studies carried out in order to understand the bonding of the cage with the endohedral unit and to explore the electronic structure of this diverse class of material. One of the interests could be to understand the factors that make the endohedral fullerene stable. High electron affinity of the fullerenes and the electro positivity of metals suggest the ionic bonding between the cage and endohedral component. This ionic model is further confirmed in a report by Johnson et al. in which it was observed that the spin density in $M@C_{82}$ is localized on the cage rather than in the endohedral unit, leading to conclusion of the transfer of valance electron to the cage [48]. The metallofullerenes in ionic model can be described of the type $M^{x+}@C_{2n}^{x-}$, where x represents the electrons transferred from the endohedral unit to the cage. The study of molecular orbital (i.e. orbital density plot) also leads to the similar conclusion of transfer of valance electrons from metal entity to the cage [49].

Very recently, Wei and coworkers [50] were successful in introducing the vanadium atom inside the fullerene cage. This work is the first report of encapsulation of group-VB transition metal in fullerene. To synthesize V containing endohedral fullerene, they used a DC- arch discharge technique with a mixture of Sc_2O_3, VC (or V_2O_5), graphite and 5% N_2. Using the X-ray crystallography, resultant molecular structures of $V_xSc_{3-x}N@(I_h)C_{80}$ (x=1,2) were determined to be I_h-C_{80} cage containing planar VSc_2N and V_2ScN clusters. The resultant structures were further characterized by UV-vis-NIR and ESR spectroscopies. Using these characterizations and electrochemical studies, they found that the electronic and magnetic properties of

$V_xSc_{3-x}N@(I_h)C_{80}$ (x=1,2) fullerenes can be tuned by tuning the number of V atoms. The vanadium ion can exist in different charge states from +2 to +5 and its ionic radius ranges from 0.46 °A for +5 to 0.79 °A for +2. The V atoms are found to be in the +3 charge state with two unpaired d electrons located on each V ion in the $VSc_2N@C_{80}$. [50] Therefore, the spin state of these clusters can be other than a singlet state. The present study computationally explores the possibility of forming similar endohedral fullerenes but with various sizes of host fullerenes: C_{70}, C_{76}, C_{78}, C_{80}, C_{82} along with different endohedral clusters: VSc_2N, V_2ScN and V_3N. Earlier in our group, we have also explored the possibility of hosting VSc_2N inside the C_{68} cage but the magnetic behavior of the VSc_2N inside the C_{68} cage was weak. In this work, we extend the scope by including various sizes of cages and computationally study the properties of those fullerenes with V_xSc_{3-x}(x=1,3) endohedral unit at the density functional level. We first find the energetically, most favorable isomers by examining a large set of promising isomers. More detailed calculations are performed to obtain the information about the electronic structure and excited states of the most stable isomers.

1.2 Carbon Onions

Carbon Onions or carbon Nano onions (CNOs) are the new allotropic form of carbon, which consists of concentric multi shell fullerene like carbon cages. The discovery of carbon onions was even before the fullerene [51] but remain in the shadow of other more popular and better-studied Nano carbon materials like graphene, fullerenes, and carbon Nano tubes etc. [52] [53] [54] [55] The potential use of CNOs in different fields such electronics, tribology, energy storage, biomedical devices etc., [56] [57] [58] [59] [60] makes this field of research as one of the attractive among carbon based materials. Here in our study we tried to explore the electronic structure of $C_{60}@C_{240}$ as one of the smallest onion cage using plot of density of states, molecular orbital etc. and also

present the transition spectra that can be useful in the experimental characterization of the Onion complex. The detail of CNOs is presented in Chapter-6.

1.3 Zinc Sulfide Cages

Zinc is mainly found in the form of sulfide in nature. ZnS shows the polymorphism with two forms: sphalerite or wurtzite. The more stable cubic form of ZnS is known as zinc blende or sphalerite where as the hexagonal form, which is less stable as compared with the former, one is better known by wurtzite. There were many studies have done in the hollow Nano particles including ZnS due to its potential application in different fields such as catalysis, delivery of drug, protection of biologically active agents, tribology etc. Here in this study we tried to explore the electronic structure calculation on different cage sizes Zn_xS_x [x = 12, 16, 24, 28, 36, 48, 96, and 108] along with their vibration frequencies, infrared spectra etc. The more detailed report is presented in Chapter-7.

Chapter 2: Theoretical and Computational Methodology

2.1 Introduction

The beauty of quantum mechanics is retained in the mathematical function termed as wave function that can describe the quantum state completely. Wave function contains all the information about a given system, thus the main goal is to get the appropriate wave function of that system. After getting it, one can operate on it with the corresponding operators to calculate various quantities of interest. All those can be achieved only after we get the appropriate wave function. Thus we need to solve the Schrodinger equation to get it but the Schrodinger equation is not solvable and straightforward except for some simple systems like hydrogen atom, a simple 2D square potential problem etc. For complex many body problems, we need to adopt the approximation methods. The density functional method is one of them to search for the approximate solution of the many body problems more efficiently and accurately. Before presenting the details of density functional theory it is better to have some discussion on some important approximation.

2.1.1 Born Oppenheimer Approximation

The Born-Oppenheimer approximation assumes that the motion of electrons and atomic nucleus can be treated separately which makes it possible to separate the total wave function of the system into electronic and nuclear components. Mathematically

$$\Psi_{total} = \psi_{electronic}\psi_{nuclear}$$

Since ions are moving slowly as compared to the electrons and the kinetic energy of electrons is much higher as compared with ions thus ions can be treated as classical particles moving in the potential created by the electrons and other nuclei. This approximation allows separating the

Schrodinger equation into electronic and nuclear parts. Within the Born-Oppenheimer approximation the Hamiltonian for the electronic system can be written as

$$\widehat{H} = -\sum_i \frac{\hbar^2}{2m_e}\nabla^2_{\boldsymbol{r}i} + \sum_i V_{ion(\boldsymbol{r_i})} + \frac{e^2}{2}\sum_{ij(i\neq j)} \frac{1}{|\boldsymbol{r_i} - r_j|} .$$

Even with this approximation the solution of the Schrodinger equation is not easy and straightforward due to the nature of electrons. This approximation does not include the effect due to the Pauli's exclusion principle, in which two electrons with parallel spin interact though their charge and spin. Furthermore if same spin electrons change their position the wave function changes the sign, which is also termed as exchange property. [61] In addition there is correlation interaction in which each electron's motion is affected by the other electrons present in the system.

2.1.2 Hartree and Hartree Fock Methods

The Hartree approximation is the simplest approach in which total wave function of the system is written as product of single electron's wavefunction. [62]

$$\Psi^H(\{r_i\}) = \phi_1(r_1)\phi_2(r_2) \dots\dots\dots \phi_N(r_N).$$

The treatment of the electronic problem in Hartree method is not appropriate due to improper description of the electronic problems such as indistinguishability between electrons, lack of inclusion of Pauli's exclusion principle. The fermionic description of the electronic problem is addressed with antisymmetric nature of wave function in Hatree-Fock approximation. The Hartree-Fock method is used to find the wave function and total energy of a system consisting of many particles in a stationary state. In this method the exact wave function of N-body interacting particles system can be approximated using single Slater determinant. [63] The total wave function (Hartree-Fock wave fuction) of the system can be found using N-coupled equations obtained

after applying the variational method, from which one can find the total energy of the system. Each electron feels the presence of the other electrons through the effective potential.

$$\Psi^{HF}(x_1 x_2 \dots\dots x_N) = \frac{1}{\sqrt{N!}} \begin{vmatrix} \phi_1(1)\phi_2(1) \dots\dots \phi_N(1) \\ \phi_1(2)\phi_2(2) \dots\dots \phi_N(2) \\ \dots \quad \dots \quad \dots \\ \dots \quad \dots \quad \dots \\ \dots \quad \dots \quad \dots \\ \dots \quad \dots \quad \dots \\ \phi_1(N)\phi_2(N) \dots\dots \phi_N(N) \end{vmatrix}$$

where N is the total number of electrons. $\phi_i(j)$ represents i[th] one-electron spin orbital with generalized coordinate j (i.e. the spatial and spin coordinates of electron j). The wave function due to the above determinant changes the sign by changing the coordinates as required by the Pauli's exclusion principle.

2.2 Density Functional Theory

DFT is the computational quantum mechanical method used to explore the electronic structure of the atoms, molecules, clusters, solids to nuclei and quantum fluids. This theory is popular among the computational chemists, physicists, and material scientists due to low cost of computation when compared with traditional methods (i.e. Hartree-Fock theory, Configuration interaction, Coupled cluster, Quadratic configuration interaction, Quantum chemistry composite methods etc.) and is considered to be accurate in the quantitative aspects. It is successfully employed to report various properties like molecular structure, ionization potential, electron affinity, atomization energies, absorption spectra, vibrational frequencies, electric and magnetic properties. The fundamental aspect of DFT is that the properties of a system with many interacting bodies are functional of electron density, which again depend on spatial variables and thus name derived as density functional. In short DFT along with Kohn Sham approach makes it possible to the development of independent particles approaches which able to incorporate the

effects of interactions and corrections among the particles, thus leading to report the properties of interacting system more closely and accurately.

2.2.1 Fundamental Basis of DFT

DFT is deeply rooted to the fundamental conceptual framework of two Hohenberg-Kohn theorems and Kohn-Sham equations. In quantum mechanics the primary goal is to find complex-valued probability amplitude i.e. wave function, which contains all the information of a system. The solution of the Schrodinger equation can report the appropriate wave function of the system, which consists of interacting nucleus, core and valance electrons. But it is only possible to solve the Schrodinger equation of the simple hydrogen like system and the complication added due to the mathematical constraint along with interacting electrons. Thus the primary goal in quantum mechanics is to get the wave function. After getting it, the average values of observables can be calculated using the expectation values of the corresponding operators and thus it is possible to explore the system along with its properties. By solving the Schrodinger equation, it is possible to probe the dynamics of state function (wave function) evolving in time.

Now, the Schrodinger equation for single electron, which is acted upon the external potential $v(\boldsymbol{r})$ (that is an attractive potential due to the nucleus) takes the form of

$$H\Psi(\mathbf{r}) = E\Psi(\mathbf{r})$$

$$\left[\frac{-\hbar^2}{2m}\nabla^2 + v(\boldsymbol{r})\right]\Psi(\boldsymbol{r}) = E\Psi(\boldsymbol{r})$$

where E is the energy eigenvalue, which can be obtained by operating the energy operator on the state function and m is the mass of the electron. For a system of N interacting electrons Schrodinger equation becomes

$\left[\sum_i^N \left[-\frac{\hbar^2}{2m}\nabla_i{}^2 + v(\boldsymbol{r_i})\right] + \sum_{i<j} U(\boldsymbol{r_i}, \boldsymbol{r_j})\right]\psi(\boldsymbol{r_1 r_2} \ldots\ldots \boldsymbol{r_N}) = E\psi(\boldsymbol{r_1 r_2} \ldots\ldots \boldsymbol{r_N})$ in which 1st term denotes the kinetic energy ($\hat{T}$) and remaining two are the potential energy terms. This is a 3N dimensional differential equation and due to the presence of nonlocal electron-electron interaction $\hat{U} = \sum_{i<j} U(\boldsymbol{r_i}, \boldsymbol{r_j}) = \sum_{i<j} \frac{q^2}{|\boldsymbol{r_i} - \boldsymbol{r_j}|}$ makes its solution more complicated. In such a situation the wave function must be approximated.

DFT provides the feasible way to solve the Schrodinger equation for the complex systems with many body problems even though there are other methods like diagrammatic perturbation theory, configuration interaction (CI) also reported in the literature but they are not efficient for the complex systems. DFT clearly tells us that a non-relativistic coulomb system can be differentiated from others only from potential term v(**r**) due to the interaction of electrons and pave a way to deal with the universal operators $\hat{T}$ and $\hat{U}$.

Hohenberg-Kohn Theorems

DFT is based on the two fundamental theorems of Hohenberg-Kohn,[64] [65]

The 1st theorem can be stated as the ground state density of a system of interacting particles that can be uniquely determined by the external potential.

Thus there is a one-to-one mapping between the ground state density and the external potential. This statement is insufficient to trace out the path to choose the true ground state density n(**r**) hence 2nd H-K theorem has been formulated,

2nd theorem states that total ground state energy of N-electrons system is a functional of ground state electron density.

From this statement it can be inferred that the true ground state electron density will be the one, which minimizes the total ground state energy. From H-K theorem the energy functional can be written as a function of single electron density and the expression for the energy functional is given by

$$E[n] = T[n] + V[n] + U[n].$$

In above expression 1st, 2nd and 3rd terms are respectively kinetic energy, potential energy due to coulomb interaction between electrons and nucleus, and potential energy due to electron-electron interaction. Even the Hohenberg-Kohn theorems provide a way to solve the many-body Hamiltonian but in real practice it encounters the problem owing to some of the terms that cannot be expressed as a functional of density.

Kohn-Sham Simplification

Kohn-Sham formulation further simplified the problem in which the system is modeled in such a way that the interacting electrons system is replaced by non-interacting fictitious particle system such that each particle experiences an average potential due to all the other electrons. This leads to the independent particle equations for non-interacting system. In addition, all the interactions like correlation between the particles and exchange interaction due to quantum effect are included in the exchange correlation functional, which is also a functional of density. By solving the equations, it is possible to find the ground state density and energy of the interacting system in which the accuracy relies on the approximation that has been made during the formulation of the exchange correlation functional. In this formulation the energy functional is expressed in terms of orbitals called Kohn-Sham orbitals, which is used to find the kinetic energy and density of the electrons.

$$E[n] = -\frac{\hbar^2}{2m}\sum_i \int \psi_i{}^* \nabla^2 \psi_i d^3\boldsymbol{r} + \int v(\boldsymbol{r}) n(\boldsymbol{r}) d^3\boldsymbol{r} + \frac{e^2}{2}\int\int \frac{n(\boldsymbol{r})n(\boldsymbol{r})}{|\boldsymbol{r}-\boldsymbol{r}'|} d^3\boldsymbol{r} d^3\boldsymbol{r}' + E_{xc}[n]$$

$$+ E_{ion-ion}$$

In this expression the terms from the left are kinetic energy, potential due to coulomb interaction between electrons and nucleus, potential due to coulomb interaction between electrons, exchange-correlation energy and the last term is due to coulomb interaction between the nuclei. The term $E_{xc}[n]$ covers all the effects that are not included in the first three terms.

Minimizing the aforementioned expression of energy functional of density leads to form the set of equation known as Kohn-Sham equations, which are indicated by

$\left[-\frac{\hbar^2}{2m}\nabla^2 + V(\boldsymbol{r}) + V_H(\boldsymbol{r}) + V_{XC}(\boldsymbol{r})\right]\psi_i(\boldsymbol{r}) = \varepsilon_i\psi_i(\boldsymbol{r})$, in which the potential term V($\mathbf{r}$) is due to the interaction between electron and nuclei. The Hartee potential is symbolized by

$V_H(\boldsymbol{r}) = e^2 \int \frac{n(\boldsymbol{r}')}{|\boldsymbol{r}-\boldsymbol{r}'|} d^3\boldsymbol{r}'$.

This is the interaction of an electron with total electron density due to which the interaction of an electron with itself is also included which does not have any physical meaning, so it is necessary to include the correction term together with correlation between electrons in V_{XC} which can be defined as $V_{XC}(\boldsymbol{r}) = \frac{\delta E_{XC}(\boldsymbol{r}).}{\delta n(\boldsymbol{r})}$.

From this point it is possible to define the trial electron density, which will help to formulate the Hartree potential. By knowing the Hartree potential it is possible to solve the Kohn-Sham equations ended with the single electron wave function. Electron density can be calculated by using $n(\boldsymbol{r}) = 2\sum_i \psi_i^*(\boldsymbol{r})\psi_i(\boldsymbol{r})$, which can be compared with the trial electron density. If they match then the problem is solved. If not, then it is necessary to redefine the

density again unless they coincide within the limit of expected accuracy. After the results coincide then that density will be ground state electron density of the system.

2.3 Exchange and Correlation Functional

Though the DFT in principle is exact, it requires the use of approximations, which can be due to Born-Oppenheimer approximation and some are because the exact form of the functional are not known. One of them is due to the lack of exact form of exchange-correlation energy. So there exist different approximations: local density approximation, generalized gradient approximations, hybrid approximations, which helps to approximate the functional within the Kohn-Sham approach. Though we have used the Generalized Gradient Approximation in DFT calculations in NRLMOL code, it is worthwhile to start with LDA then move on to the GGA functional.

Local density approximation (LDA)

LDA are the approximations to the exchange-correlation energy functional in density functional theory and depend on the electron density at each point in space. From this approximation the exchange-correlation energy per electron at point **r** is equal to the exchange-correlation energy of the homogeneous electron gas that has the same density as the electron gas at that point

$$\varepsilon_{Xc}(r) = \varepsilon_{XC}^{homo}[\rho(\boldsymbol{r})]$$

$$E_{XC}[\rho(\boldsymbol{r})] = \int \varepsilon_{XC}(\boldsymbol{r})\rho(\boldsymbol{r})d\boldsymbol{r}$$

where ρ and ε_{XC} is the electronic density and exchange-correlation energy per particle of a homogeneous electron gas of charge density ρ. Here all the nonlocal dependencies of the energy functional are neglected and thus best represent for the systems, which are close to the homogeneous gas in terms of electron density variation i.e. metallic, ionic, strongly bonded

covalent etc. Due to inaccurate binding LDA underestimates the bond length and band gaps in solid. [64]

Generalized Gradient Approximation

LDA assumes that the electronic density is same through out the space but in real system, which is not true thus to account for the non-homogeneity of the true electron density the improvement over LDA was proposed in which exchange-correlation energy is no more only the functional of local density but also the functional of gradient and higher derivatives of electron density and these expansions are referred to as the generalized gradient approximations (GGA), which is proposed by Perdew, Burke and Ernzerhof (PBE). [64] [66]

$$E_{XC}[\boldsymbol{\rho}] = \int \rho(\boldsymbol{r})\varepsilon_{XC}[\rho(\boldsymbol{r})]F_{XC}[\rho(\boldsymbol{r}), \Delta\rho(\boldsymbol{r}), \Delta^2\rho(\boldsymbol{r}), \ldots\ldots\ldots]d\boldsymbol{r}$$

where F_{XC} is the dimension less enhanced term included the modification over LDA in order to include the variation of density around **r.** The GGA can better report the binding energies, atomic energy, bond lengths and bond angles over LDA.

2.3 Executable Used in this Study

2.1.1 NRLMOL

NRLMOL, the Naval Research Laboratory Molecular Orbital Library is a massively parallel code employed to report the electronic structure calculations on atoms, molecules and clusters etc. The code is based on Kohn-Sham formulation of density functional theory in which the electronic orbitals and eigenstates were determined using a linear combination of Gaussian atomic type molecular orbital (LCGTO) approach. This code is useful to report harmonic vibrational frequencies, infra-red spectra, Raman spectra, polarizability, density of staes, joint density of states, vibrational polarizability and also convenient for full or partial structure

optimization etc.[66] [67] [68] [69] [70] NRLMOL is principally developed by Mark Pederson and collaborators.

2.3.2 Vienna Ab Initio Simulation Program (VASP)

VASP is employed to perform the ab-initio quantum mechanical simulations [71] [72] and uses the pseudo potentials or project-augmented wave (PAW) method [73] [74] and a plane wave basis set [75]. The VASP code uses periodic boundary conditions and therefore is suitable for studying extended periodic systems. The VASP code is based on the density functional theory. The code requires some of the input files such as INCAR, POSCAR, POTCAR and KPOINTS, in which mainly direction of the calculations, position of the atoms, pseudo-potential for the atomic species used in the calculations, k points coordinates, mesh size to create the k-point grid etc. are provided. The successful completion of calculation results to form some output files such as: OUTCAR, CHGCAR, CONTCAR, EIGENVAL, DOSCAR files etc.

2.3.3 Molecular Orbital Package (MOPAC2009)

MOPAC is a software package with powerful semi-empirical quantum chemistry program based on NDDO [76] approximation first introduced by John Pople, in which NDDO stands for neglect of diatomic differential overlap. In this formalism, the overlap matrix is replaced by unit matrix and one and two centered integrals are either evaluated approximately or parameterized based on available experimental data. Mostly greater than two centered integrals are neglected due to which semi-empirical methods are fast and can be applicable for the large systems without compromising on the accuracy if applied to those molecules that are similar to the molecules used in parametrization. Even within the NDDO formalism different models were proposed based on the type of approximations and parametrization employed such as: Modified

Neglect of Diatomic Overlap (MNDO) [77], Austin Model 1(AM1) [78], Parametric method 3 (PM3) [79], Parametization method 6 (PM6) [80] etc.

2.3 Computational Approach

The search for the most stable isomer of an endohedral fullerene is challenging due to large number of possible isomers. The host C_{68} fullerene cage alone has 6332 isomers and the number of isomers increases significantly as moving to the larger fullerene cages. The orientation of encapsulated cluster inside the fullerene cage further enriches the configuration space for the search of the most stable isomers. Since the V atoms are found to be in the +3 state in the $VSc_2N@C_{80}$ fullerene [50], the number of electrons transferred from the encapsulated cluster to the outer cage is same as that for the Sc_3N cluster. To identify the lowest energy isomer of $V_xSc_{3-x}N@C_{2n}$(x=1-3, 2n=68,70,76,78,80,82), we used a systematic approach. First, all fullerene cage isomers for a given size were generated using fullgen algorithm [81] [82] and optimized using fullprod code developed in our lab in combination with MOPAC2009 [83]. It has been known from previous studies that the stability of the metal nitride endohedral fullerene is primarily due to the charge transfer from the encapsulated unit to the fullerene moiety. We thus optimized all isomers of C_{68} fullerenes in −2, -4 and−6 charge states and rest of others larger fullerenes in the -6 charge state. The lowest 300 isomers from each charge states in C_{68} and -6 charge state for other fullerenes were chosen for further calculations. Using these isomers we constructed the starting geometries of $VSc_2N@C_{68}$ endohedral fullerenes using the Cindy auxillary code developed in our laboratory. The VSc_2N unit is planar and was rotated about x-, y- and z- axis to generate 3 conformers for each of the parent cages. All isomers of endohedral fullerenes thus generated were again optimized at the PM6 level [83] in which it was found that the order of lowest seven isomers in different charge states of C_{68} is same hence the lowest 10 energetically distinct isomers of $VSc_2N@C_{68}$ followed from hex-anionic series were chosen further optimization at the DFT level. We did same calculation for other large fullerenes C_{70}, C_{76}, C_{78} and C_{80} for which we optimized all the possible isomers at PM6 level in hex-anionic state then

lowest 300 isomers were chosen to generate three conformers from each isomers by rotating separately optimized VSc_2N unit along x-, y- and z orientations, which resulted the 900 different structures. Those structures again optimized at PM6 level in neutral state. Again the lowest 10 structures at PM6 level are chosen for DFT calculation. All the DFT calculations reported here are carried out at the all-electron level using the Perdew-Burke-Ernzerhof exchange-correlation functional [84]. We have used the NRLMOL code for the optimization and the calculation of the electronic structure. [68] [69] [67] [70] [66] We have used the default NRLMOL basis set that uses 12, 13, 20 and 19 bare Gaussians for each C, N, V and Sc atoms respectively.

Chapter 3: Electronic Structure Calculation of Vanadium, Scandium Based Endohedral Fullerenes $VSc_2N@C_{2n}$(2n=70,76,78,80)

Introduction

The carbon cages in the endohedral fullerenes serve as a robust container to accommodate some units like atoms, molecules and clusters. Just after the discovery of Buckminsterfullerene C_{60} in 1985 by Smalley et al., the endohedral fullerene $La@C_{60}$ was synthesized for the first time in the same year. [85] The attention on endohedral fullerenes grew after its macroscopic production by Huffman and his group in 1990. [86] Still, the production of endohedral fullerenes was low and was about only 1% of the total production of empty cages of fullerenes. Harry Dorn et al. in 1999 successfully synthesized tri-scandium nitride cluster fullerene $Sc_3N@C_{80}$ using N_2 gas environment in the Kratschmer Huffman arc generator, which greatly enhances the yield of endohedral fullerenes. [87] The higher kinetic stability obtained from the opening of gap between the highest occupied molecular orbital (HOMO) and lowest unoccupied molecular orbital (LUMO) makes this nitride cluster fullerene (NCF) as the most abundant fullerene after C_{60} and C_{70}. Subsequently, other synthesis methods for the endohedral fullerenes were reported, which produced the endohedral fullerenes in macroscopic amounts. [88] [89] [90] [91] [92] Attractive properties like large surface area, high electron accepting capacity and empty space to accommodate the atoms, molecules and cluster for potential use in different applications such as medicine, electronics etc. make the fullerenes and endohedral fullerenes one of the active areas of research. [93] [94] [95] [96] [97] [98] [99] [100]

The stability of fullerenes is driven by the isolated pentagon rule (IPR). This rule is strictly followed by the empty cage fullerenes, and it grants the stability to only those fullerenes in which all the pentagonal sides are shared by hexagons. It has been pointed out that it is not possible for the C_{20}-C_{58}, C_{62}-C_{68} cages to satisfy the isolated pentagon rule. These carbon cages

have high strain, and as a result, are unstable and difficult to isolate. In the endohedral form, however, the complexation releases large strain energy, which leads to formation of stable structures. Before 2000, it was believed that only IPR fullerenes can be realized, but after the isolation of non-IPR $Sc_2@C_{66}$(4348) and $Sc_3N@C_{68}$(6140) structures, a number of non IPR endohedral fullerenes were reported. [101] [102] An elucidation on stabilization of the endohedral fullerenes is reported by Park et al. in which they proposed that there is change in aromaticity of the pentalene (two fused pentagons) system moving from neutral to charged state using negative nucleus independent chemical shift (NICS) near the ring center. [103] Thus gain in aromaticity, due to charge transfer from endohedral moiety to the cage, enhances the stability of the whole complex.

Recently, Wei et al. were successful in substituting scandium atom in $Sc_3N@C_{80}$ with vanadium. [104] This work is the first report of encapsulation of group-VB transition metal in fullerene. To synthesize vanadium-containing endohedral fullerene, they used DC- arc discharge technique with a mixture of Sc_2O_3, VC (or V_2O_5), graphite and 5% N_2. Using X-ray crystallography, resultant molecular structures of $V_xSc_{3-x}N@(I_h)C_{80}$ (x=1,2) were determined to be I_h-C_{80} cage containing planar VSc_2N and V_2ScN clusters. The resultant structures were further characterized by UV-vis-NIR and ESR spectroscopies. Using these characterizations and electrochemical studies, they found that the electronic and magnetic properties of $V_xSc_{3-x}N@(I_h)C_{80}$ (x=1,2) fullerenes can be tuned by changing the number of V atoms. The vanadium ion can exist in different charge states from +2 to +5 and its ionic radius ranges from 0.46 °A for +5 to 0.79 °A for +2 charge states. The V atoms are found to be in the +3 charge state with two unpaired d electrons located on each V ion in $VSc_2N@C_{80}$ and $V_2ScN@C_{80}$. [104] In our recent study, we examined the possibility of encapsulation of the VSc_2N unit inside the C_{68}

fullerenes. Very elaborate search for the most stable structure showed that the isomer 6079 to be the most stable candidate having significant chemical stability among all the 6332 isomers of C_{68}. [105] The vanadium doped fullerenes have spin magnetic moment but the spin-orbit coupling is found to be weak. [105] Most important finding of this study was the different isomer as the most stable structure of $VSc_2N@C_{68}$ than the one for the $Sc_3N@C_{68}$ fullerene. This observation motivated us to computationally explore the possibility of forming similar endohedral fullerenes with other host fullerene cages such as C_{70}, C_{76}, C_{78}, and also C_{80}. We computationally studied the properties of those fullerenes with VSc_2N endohedral unit at the density functional level. Using the procedure outlined recently, [105] we performed a large scale search that involves thousands of optimizations to identify the most favorable isomers of $VSc_2N@C_{70}$, $VSc_2N@C_{76}$, $VSc_2N@C_{78}$, and $VSc_2N@C_{80}$. Subsequently, detailed density functional calculations using large basis sets are performed to obtain the information about the electronic and structural properties of the most stable isomers.

Computational Method

The search for the most stable candidate becomes increasingly tedious as the number of isomers increases rapidly with the increase in cage size. The screening of 8149, 19151, 24109, and 31924 isomers of C_{70}, C_{76}, C_{78}, and C_{80} fullerenes has been done in order to select the energetically most favourable structure of endohedral fullerene. First, all the possible candidates of fullerenes were generated using the fullgen algorithm. [106] One of the important aspect of trimetallic nitride fullerenes is the charge transfer from endohedral unit to the cage which leads to stable endohedral fullerene structures. The formal charges transferred from the endohedral

unit to the fullerene cage in $VSc_2@C_{80}$ and $VSc_2@C_{68}$ is six electrons. Therefore, all the candidates of fullerenes were optimized in the hexanionic state at PM6 level using the MOPAC2009.[107] From the optimized database of hexanionic fullerenes, the lowest 300 isomers were selected as initial parent cages for the encapsulation of VSc_2N unit. The different orientation of the endohedral unit in each cage further increases the configurational space. These 900 initial geometries were obtained by rotating the planar VSc_2N unit perpendicular to the three principal axes of inertia which we label as x-, y-, and z- axes unit in each of the 300 isomers. The resultant endohedral fullerene geometries were again optimized using the MOPAC2009 at PM6 level. From those optimized structures, we chose some of the lowest isomers for further optimization at DFT level. The procedure is repeated for all the C_{70}, C_{76}, C_{78}, and C_{80} host fullerenes.

All the calculation at density functional level reported here were done at all electron level using PBE functional with generalized gradient approximation as implemented in UTEP-NRLMOL code.[108] [109] [110] NRLMOL uses the gaussian functions as the basis set which has 35 basis functions for the carbon atoms.[111] The partial charges were obtained using the density derived electrostatic and chemical net atomic charges as implemented in the ChargeMol code.[112] [113]

Results and Discussion

$VSc_2N@C_{80}$

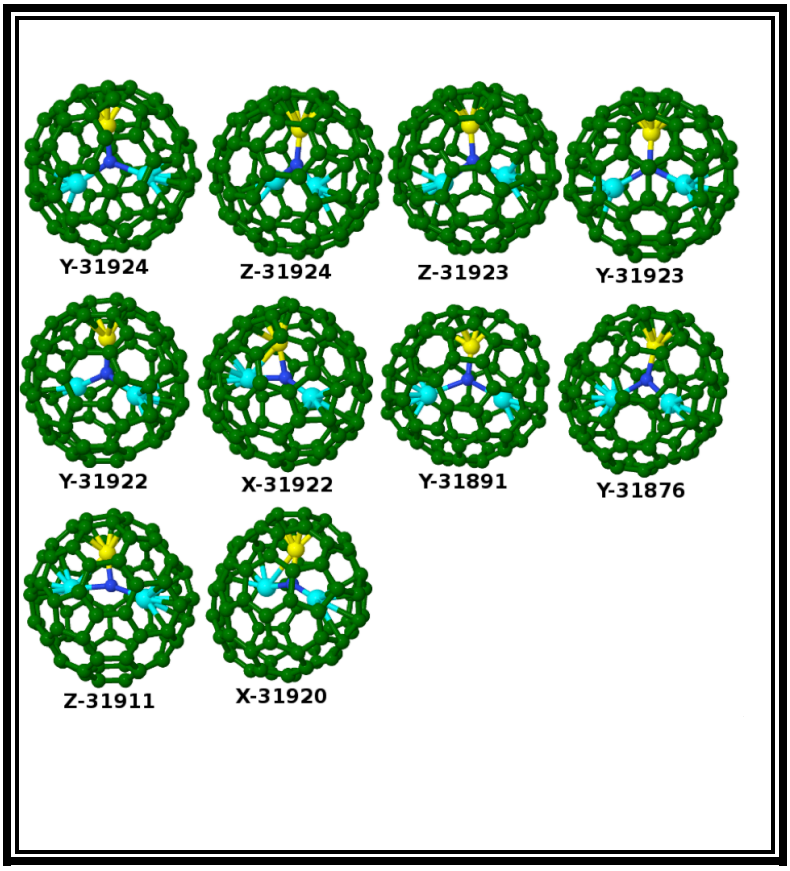

Figure 3.1: Optimized structures of $VSc_2N@C_{80}$ endohedral fullerenes. Carbon, Scandium, Vanadium and Nitrogen atoms are represented by green, aqua, yellow and blue respectively.

We first present the results of our calculations on the $VSc_2N@C_{80}$ fullerene and compare them with the available experimental results in order to validate the search method adopted in this work. The C_{80} based endohedral fullerenes are among the most studied ones. Particularly, $Sc_3N@C_{80}$ is the most abundant endohedral fullerene, and among all fullerenes it is the third most abundant fullerene after C_{60} and C_{70}. The successful entrapment and their studies on various

aspects of some of the clusters like: Sc_3N, [87] Gd_3N, [114] Dy_3N, [115] Tb_3N, [116] $ErSc_2N$, [117] and $CeSc_2N$ [118] etc. in the C_{80} cage have been documented in various reports. [119] The stabilization of endohedral C_{80} fullerene with those clusters is mainly due to the charge transfer from the endohedral unit to the fullerene cage. Recently, Wei et al. have synthesized V-substituted $V_xSc_{3-x}N@C_{80}$ fullerenes and have performed X-ray crystallography for structural characterization. [104] The structural characterization shows that the $VSc_2N@C_{80}$ has the fullerene shell of the isomer 31924, a fullerene with icosahedral symmetry. This system allows us to test our computational procedure adopted here for search of the endohedral fullerenes. For the C_{80} fullerene, the variations in the position of pentagons and hexagons results in 31924 different isomers. Out of these only seven isomers have isolated pentagons i.e. do not have two or more adjacent pentagons. These IPR structures are D_2, D_{5d}(31918), C_{2V}(31920), D_3, C_{2V}(31922), D_{5h}(31923), and I_h(31924). The IPR isomers with D_2 and D_{5d} symmetries are isolated and characterized as empty cages whereas the isomers 31924(I_h) and 31923(D_{5h}) are unstable in their pristine form due to their open shell electronic structure but the stability of these cages increases significantly with the transfer of electrons from endohedral moiety to the cage during the formation of endohedral fullerenes. The search procedure adopted here looks for the energetically bes*t*, that is, the most stable isomer of $VSc_2N@C_{80}$ endohedral fullerene. This is done by optimization of all the 31924 different isomers in its hexanionic at PM6 level using an inhouse code that interfaces with MOPAC2009. [107] These optimized structures provide a database of candidate structures for the search of endohedral fullerene. From this set of optimized isomers, three hundred lowest energy optimized structures were chosen for further calculation in which the cages were impregnated with a planar VSc_2N endohedral unit for which three different orientations along each mutually perpendicular orientations named as x, y, z were chosen. This step resulted in 900

$VSc_2N@C_{80}$ endohedral fullerenes, which were again optimized at the same level of theory. From these 900 optimized structures, the 10 lowest were further optimized at the DFT level as shown in Figure-3.1. We use the labeling notation with the letters X, Y and Z followed by the isomer number in order to distinguish the isomers according to the orientation of endohedral unit along x-, y- and z- axes (principal axes) in the initial geometries. Both DFT and PM6 calculations find isomer 31924 is the lowest energy structure irrespective of the orientation of the endohedral unit. The endohedral unit maintains the planar structure intact in isomer 31924 which is the lowest structure identified from DFT calculations. The sum of angles around the central nitrogen is 359.9 degree, which is in close agreement with 358.8 degree reported by Wei et al. [104] Similar planar structure of endohedral cluster Sc_3N was reported in $Sc_3N@C_{80}$ (31924) by Stevenson et al. [120] The V-N distance is 1.86 Å, which is in perfect agreement with the experimental result. [104] The observed Sc-N distances are 2.10 Å and are longer than the V-N distance by 0.24 Å, which may be due to the smaller ionic radius of V^{3+} (0.64 Å) as compared with Sc^{3+} (0.75 Å). [121] The vanadium atom is oriented toward the center of a hexagon and located at a distance of 2.24 Å from the closest carbon. Both the scandium atoms are oriented towards the vertices shared by two hexagons and a pentagon. Similar orientation of each scandium was observed in the experiment as well.[20] [104] Both scandium atoms are located at a distance of 2.26 Å from the closest carbons on the cage. Thus, the VSc_2N unit is almost symmetrically placed at the center of the cage. The 3d atoms are in the +3 charge state with a total magnetic moment of 2 μ_B for the complex.

In the spin compensated case, vanadium atom is oriented towards the center of a hexagon, and all the six carbons on that hexagon are at a distance of 2.22 Å from vanadium, and

the closest carbon atoms from both scandium are at a same distance of 2.25 Å. The V-N distance decreases slightly (0.02 Å) while the Sc-N distance increases by 0.04 Å when compared with Y isomer. The small energy difference between different conformers in which the orientation of the endohedral unit varies, is indicative of a free rotation of VSc_2N within the cage. On the other hand, restricted free rotation was noted in case $TiSc_2N@C_{80}$ (I_h) and Born-Oppenheimer molecular dynamics simulations showed that the dynamics of $TiSc_2N$ cluster can be described as restricted free rotation around Ti-N axis. [122] The HOMO-LUMO gap in isomer 31924 (with different orientations) is about 0.41 eV. This is much smaller than the HOMO-LUMO gap of 1.44 eV for the homogeneous NCFs $Sc_3N@C_{80}$ at the PBE level of calculation. [123] The presence of the vanadium atom introduces d-states near the Fermi level and thereby reduces the gap when compared with $Sc_3N@C_{80}$. A plot of the the HOMO and LUMO isodensity surface shows that these orbitals are mostly located on the vanadium atom.

Among the DFT optimized structures of $VSc_2N@C_{80}$, only two isomers 31920 and 31924 have magnetic moment of 2 μ_B, which is due to the transfer of 3 electrons to the cage and having formal +3 charge state with two unpaired electrons in the vanadium d orbital. The paramagnetic behavior of $VSc_2N@C_{80}$ was also confirmed in the experiment by Wei et al. using ESR and NMR signals. [104]

Table 3.1. Ten lowest energy isomers of $VSc_2N@C_{80}$ fullerenes, energies relative to the most stable structure in respective levels of theory and HOMO LUMO (H_L) gaps are also presented. All the reported energies are in eV.

$VSc_2N@$	DFT Energy	PM6 Energy	H_L gap (DFT)
C_{80}(X-31920)	2.90	1.43	0.14
C_{80}(X-31922)	2.00	1.06	0.10
C_{80}(Y-31876)	2.46	1.35	0.61
C_{80}(Y-31891)	2.34	1.52	0.17
C_{80}(Y-31922)	1.59	0.62	0.47
C_{80}(Y-31923)	1.22	0.88	0.33
C_{80}(Y-31924)	0.00	0.02	0.41
C_{80}(Z-31911)	2.84	1.33	0.58
C_{80}(Z-31923)	0.76	0.63	0.22
C_{80}(Z-31924)	0.00	0	0.38
C_{80}(X-31924)	0.00	0.02	0.41

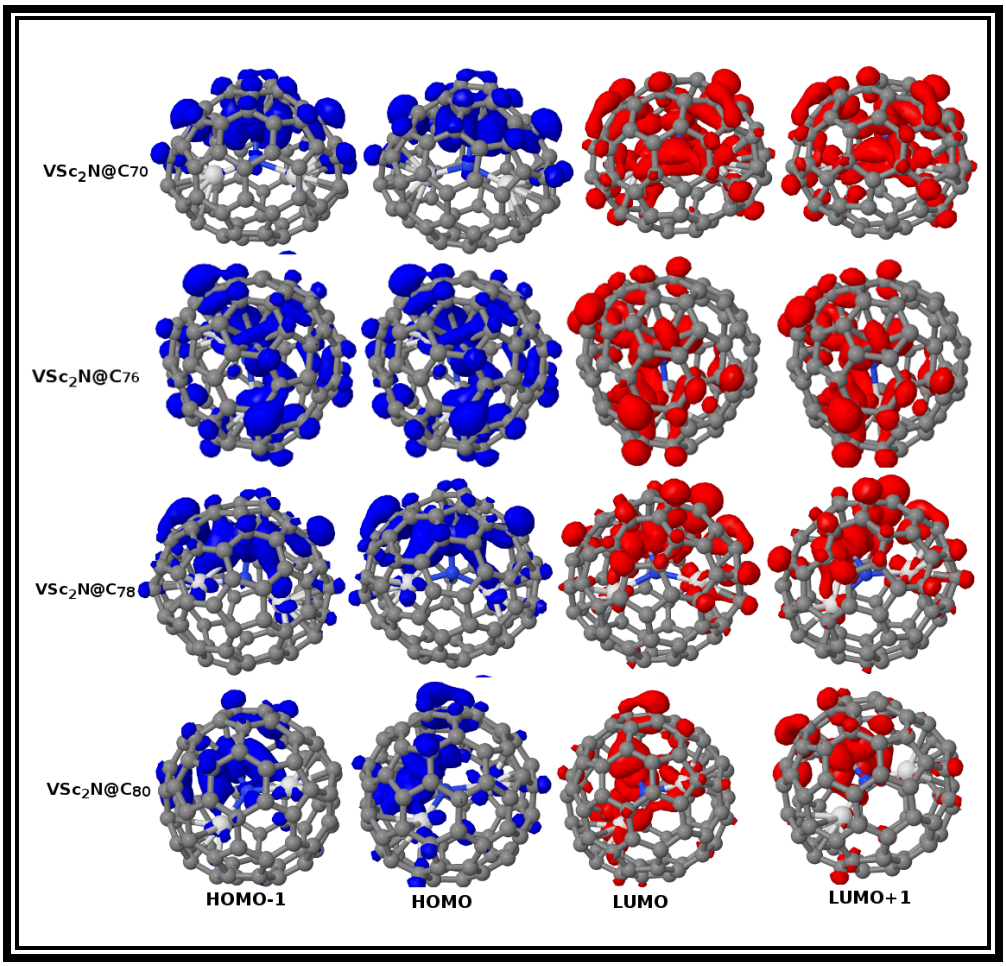

Figure 3.2: The molecular orbital plot for most probable cages for $VSc_2N@C_{70}$ (7854), $VSc_2N@C_{76}$ (19151), $VSc_2N@C_{78}$ (24109) and $VSc_2N@C_{80}$ (31924). HOMO-1, HOMO, LUMO and LUMO+1 from left to right.

We have also plotted a few molecular orbitals for the lowest energy structure of $VSc_2N@C_{80}$. These are shown in the bottom row in Figure-3.2. Among the four frontier orbitals, HOMO and HOMO-1 levels are mostly smeared on the vanadium and some of the carbon atoms. The four lobes around the vanadium indicates the most prominent contribution is due to the d orbital. The magnetic moment is mostly due to the higher number of majority unpaired electrons

in the vanadium d orbital and partly by carbon p orbitals as shown in Figure-3.3**.** The first two removals of electron (ionizations) would mostly occur from the vanadium d orbital. Likewise, the contribution due to vanadium d orbital is dominant for the LUMO and LUMO+1 levels. Thus addition of an extra electron would be primarily on the vanadium atom (d orbital). The scandium atoms have small contribution to the LUMO level which further diminishes in LUMO+1 level as shown in Figure-3.2. The density of states is plotted in Figure-S1. The above observation of the HOMO and LUMO plots is also seen in the DOS which shows the contributions from the vanadium d orbital and carbons p orbitals to these levels. Similar behavior was reported for the $TiSc_2N@C_{80}$ fullerene endohedral unit by Popov et al. where both the oxidation and reduction mainly occurs from the endohedral unit; it was reported to be the first endohedral fullerene to be electrochemically active in both reduction and oxidation. [122] Furthermore, Popov et al. reported that the localization of an unpaired electron occurs mainly on the Ti atom. [122] This is quite similar to our result in which we found the localization of unpaired electrons on the vanadium atom using density of states plot as shown in Figure-3.3. (Note: electronic configuration of vanadium only differ by one more electron in d orbital with that of titanium).

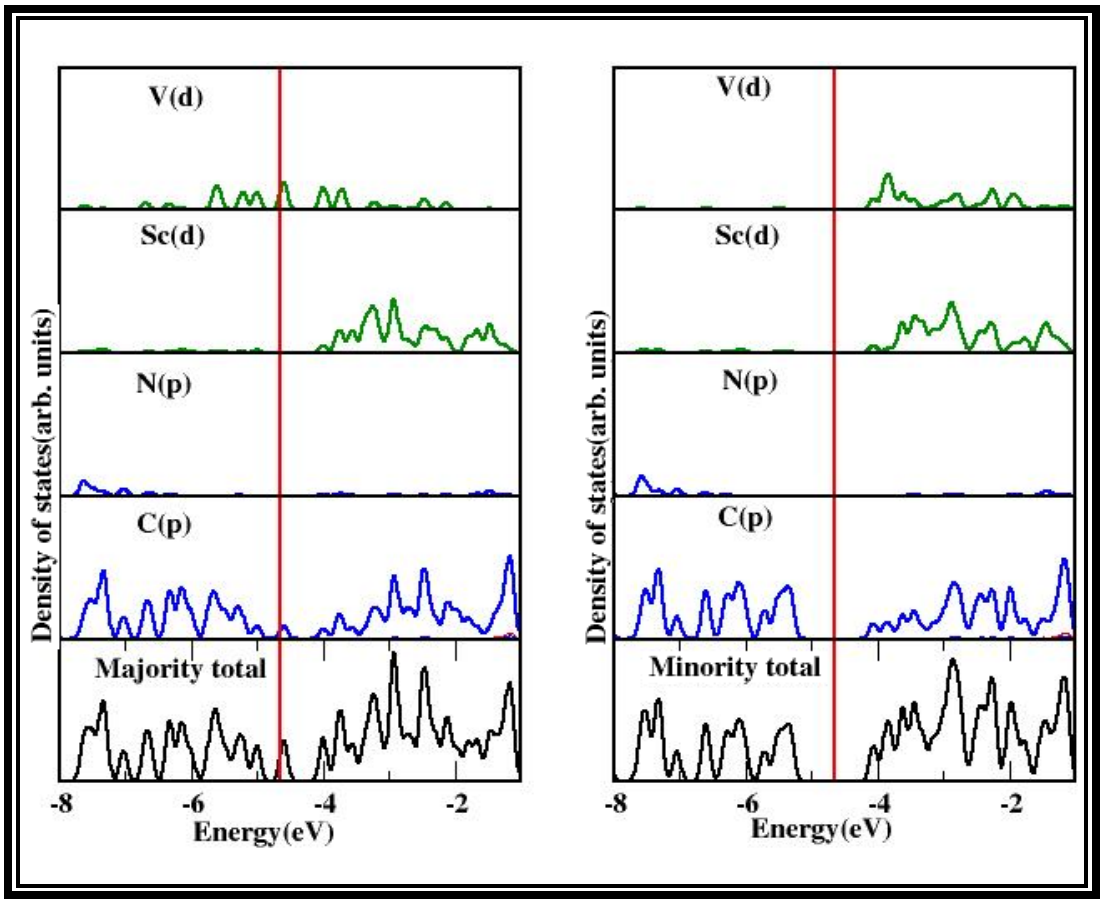

Figure 3.S1: Majority and minority spin density of states plot for the $VSc_2N@C_{80}$ (31924). The blue, green, and black curves indicate contribution due to s, p, d, and total states respectively. The red vertical line is the fermi level.

$VSc_2N@C_{70}$

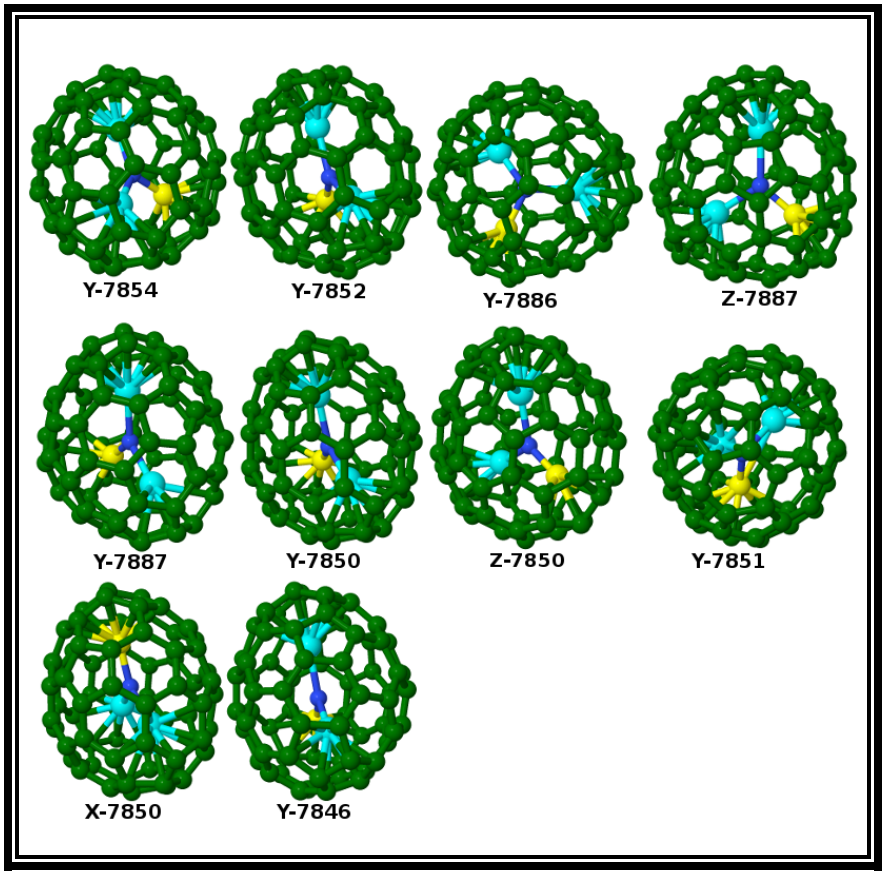

Figure 3.3: Optimized structures of $VSc_2N@C_{70}$ endohedral fullerenes. C, Sc, V and N atoms are represented by green, aqua, yellow and blue respectively.

There are 8149 different isomers of the C_{70} fullerene, among which only the isomer 8149 with D_{5h} symmetry follows the isolated pentagon rule. We optimized all 8149 structures which consists of 2-D_{5h}, 5-C_{3v}, 14-C_{2v}, 8-C_3, 300-C_2, 186-C_s, and 7634 isomers of C_1 symmetry [124] [125] in the hexanionic state at PM6 level using MOPAC 2009. Popov et al. carried out the similar calculations on hexanionic state of the C_{70} but using AM1 level of theory. [126] Out of the ten lowest isomers reported by them, eight of them agree with our lowest C_{70}^{-6} isomers. From the

optimized structures, 300 energetically most favorable cages within an energy window of 2.4 eV were chosen for further calculations. Three different orientations of the planar VSc_2N unit were chosen so that the unit lies perpendicular to the three principal axes of inertia which we label as x-, y-, and z-axes. The rotation of the endohedral unit led to 900 initial geometries of endohedral fullerenes $VSc_2N@C_{70}$. They were again optimized at the same level of theory. Subsequently, ten most promising isomers within an energy window of 0.33 eV were selected and optimized using the NRLMOL code at the DFT level. The optimized structures are shown in Figure-3.4. Among the competing structures, the isomers Y-7852 and Y-7854 are the most probable candidate at PM6 and DFT level of theory respectively. All the isomer numbers are as according to Fowler's table.[125] The same parent cage 7854 with C_{2v} symmetry is proclaimed to encapsulate the widely studied Sc_3N unit and its successful entrapment in C_{70} was reported by Shangfeng et al. in 2007. They synthesized the $Sc_3N@C_{70}$ using reactive gas atmosphere method and claimed the yield of the product of above 99% purity level using two-step HPLC.[127] There are three pairs of fused pentagons (pentalene) in isomer 7854 in which we observed that all three metal atoms orientated towards the pentalenes (fused pentagons). Similar proximity of metal atoms with fused pentagons in $Sc_3N@C_{70}$(7854) was also mentioned by Ceron et al.[128] The bond lengths of Sc-N and V-N are 2.17 Å and 1.84 Å respectively where significant stretching of Sc-N bond was observed as compared with respective bond distances in the separately optimized planar VSc_2N cluster, which may be due to Coulomb attraction between the positively charged ions and negatively charged cage. The reported Sc-N bond distances on $Sc_3N@C_{70}$(7854) by Yang et al.[129] were significantly lower as compared with our calculated Sc-N bond distances on $VSc_2N@C_{70}$(7854). The planar structure of VSc_2N endohedral unit remains intact inside the cage where the longer Sc-N bonds are somewhat along the axis of the oval C_{70} cage and the shorter V-

N bond is almost perpendicular to it. The closest carbon atoms are at 2.33 Å from both the scandiums, while the closest carbon is at 2.12 Å from the vanadium. The VSc_2N is located on one side of the cage and the proximity of the V to the carbon wall distorts the overall shape of the C_{70} cage. The isomer with VSc_2N perpendicular to the molecular axis shows distortion of the VSc_2N from a planar structure which causes the energy penalty of 0.70 eV due to the dominating steric strain over stabilization gain due to the charge transfer. We find that the $VSc_2N@C_{70}$ has two nearly degenerate spin states with spins S=0 and and S=1. The energy difference between the two states is only 0.02 eV at the PBE level. The charge states of the transition metal atoms remain same in both the isomers although the N-Sc bonds are slightly shorter by 0.08 Å and N-V bonds are longer by 0.08 Å. In the S=1 state, the vanadium has two unpaired d electrons, which results in the magnetic moment of $2\mu_B$. In the singlet state, the vanadium d electrons are paired resulting in a singlet state. The overall symmetry of the C_{70} fullerene is lost upon encapsulation and no significant structural change was noted between the two spin states. The densities of states of the two spin isomers are shown in Figure-S3. The lowest two panels show the total and the projected DOS on V ion for the S=0 isomer and the upper four panels show the spin majority and minority total DOS and the projected DOS on V. In the S=0 isomer, the HOMO-LUMO gap is wider (0.45 eV) compared with the S=1 state (0.29 eV) with the V occupied d states lying below the Fermi level in both the isomers. The carbon states near the Fermi level, which are noticeable in the total DOS, remain similar in both the isomers. Thus the HOMO in both the isomers has major contributions from the V d states, but in one isomer they are paired. The VSc_2N unit is not a stable molecule and tends to break apart in isolation. The confinement effect of the cage is required for it to form. In C_{70}, the cage volume is smaller compared to the C_{80} cage

resulting in larger interaction between the endohedral unit and the cage. Slight changes in the structure of the complex are sufficient to change the d states of the endohedral unit.

The calculated HOMO-LUMO gap in the lowest energy isomer Y-7854 is 0.46 eV. Yang et al. reported HOMO-LUMO gap of 1.29 eV in the $Sc_3N@C_{70}$ (7854) [127] and Zheng et al. reported the gap of 1.71 eV for the $Sc_2@C_{70}$ (7854) at PBE1PBE/6-31g* level of theory. [130] The HOMO-LUMO gap in the ten most stable structures ranges from 0.17 eV to 0.47 eV as shown in Table-3.2.

Table 3.2: Ten lowest energy isomers of $VSc_2N@C_{70}$ fullerenes, energy relative to the most stable structure in respective levels of theory, and the HOMO-LUMO gaps are presented. All the reported energies are in the eV.

$VSc_2N@$	DFT	PM6	H_L gap
C_{70}(X-7850)	1.09	0.33	0.32
C_{70}(Y-7846)	1.20	0.19	0.25
C_{70}(Y-7850)	0.93	0.23	0.38
C_{70}(Y-7851)	0.98	0.27	0.36
C_{70}(Y-7852)	0.40	0	0.30
C_{70}(Y-7854)	0	0.09	0.46
C_{70}(Y-7886)	0.82	0.17	0.40
C_{70}(Y-7887)	0.92	0.26	0.36
C_{70}(Z-7850)	1.08	0.33	0.38
C_{70}(Z-7887)	0.92	0.26	0.36

In S=0 $VSc_2N@C_{70}$, HOMO-1 is mostly localized on the vanadium with four lobes showing the d orbital shape, and it also spreads over some of the carbon atoms. The contribution due to Sc atoms is insignificant as shown in Figure 3.2. Again distribution of the HOMO level looks very similar to the HOMO-1 and is mostly contributed by vanadium and few carbon atoms. The distribution of the LUMO and LUMO+1 level looks different than that of the HOMO and HOMO-1, and it is smeared over all the atoms in the endohedral unit and also in the some of the carbon atoms in the cage. The density of states plot (Figure-3.S2) shows that the HOMO level is contributed mostly by vanadium d orbital and carbon p orbital, whereas the LUMO is due to vanadium and scandium d orbital and p orbital of nitrogen and carbon atoms as well.

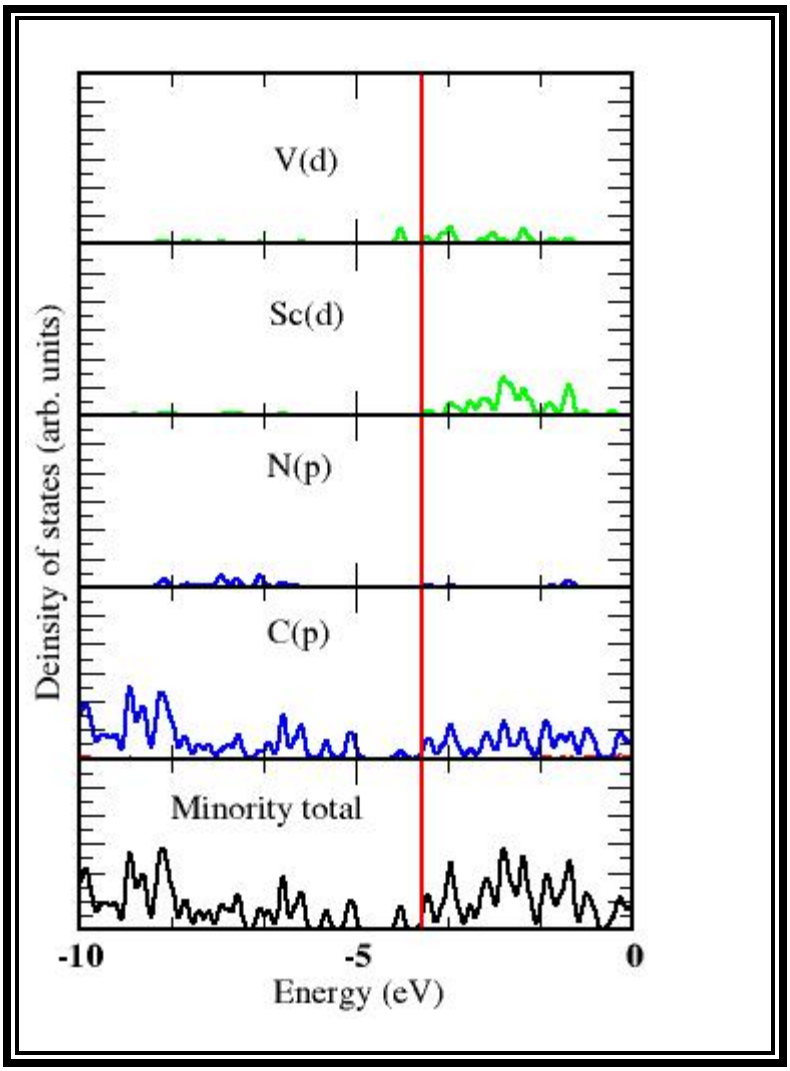

Figure 3.S2. DOS plot for $VSc_2N@C_{70}$

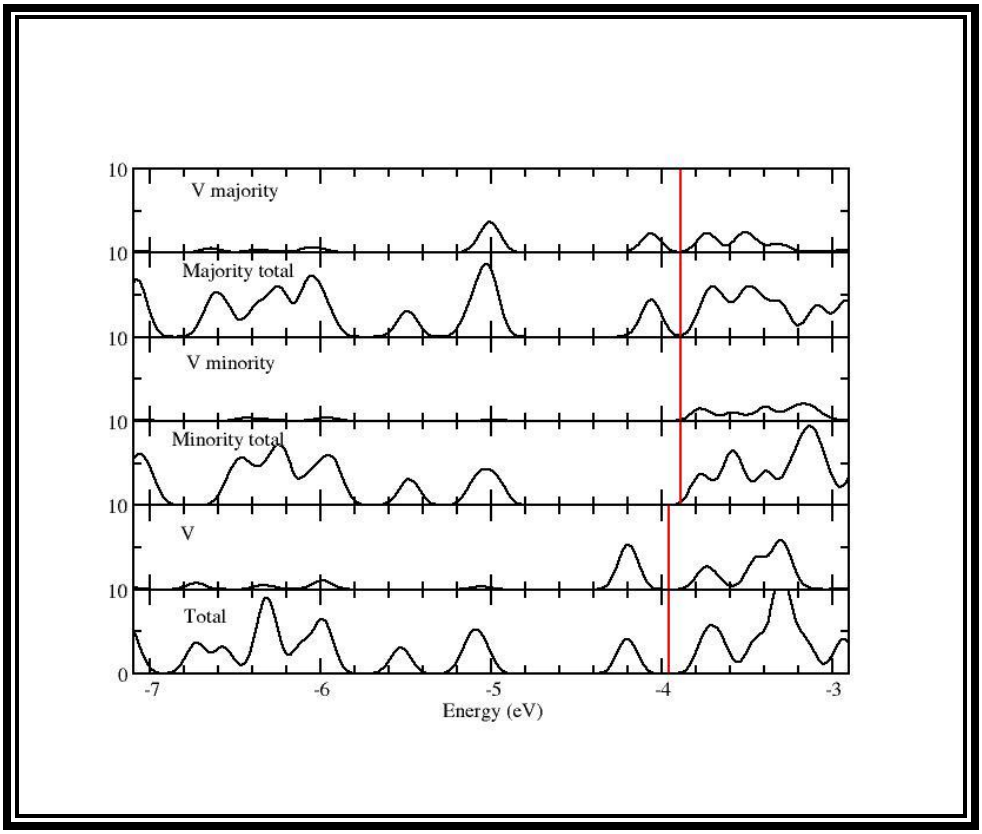

Figure 3.S3. The DOS of two spin isomers of $VSc_2N@C_{70}$. The lowest two panels show the total and the projected DOS on V ion for the S=0 isomer and the upper four panels show the spin majority and minority total DOS and the projected DOS on V.

$VSc_2N@C_{76}$

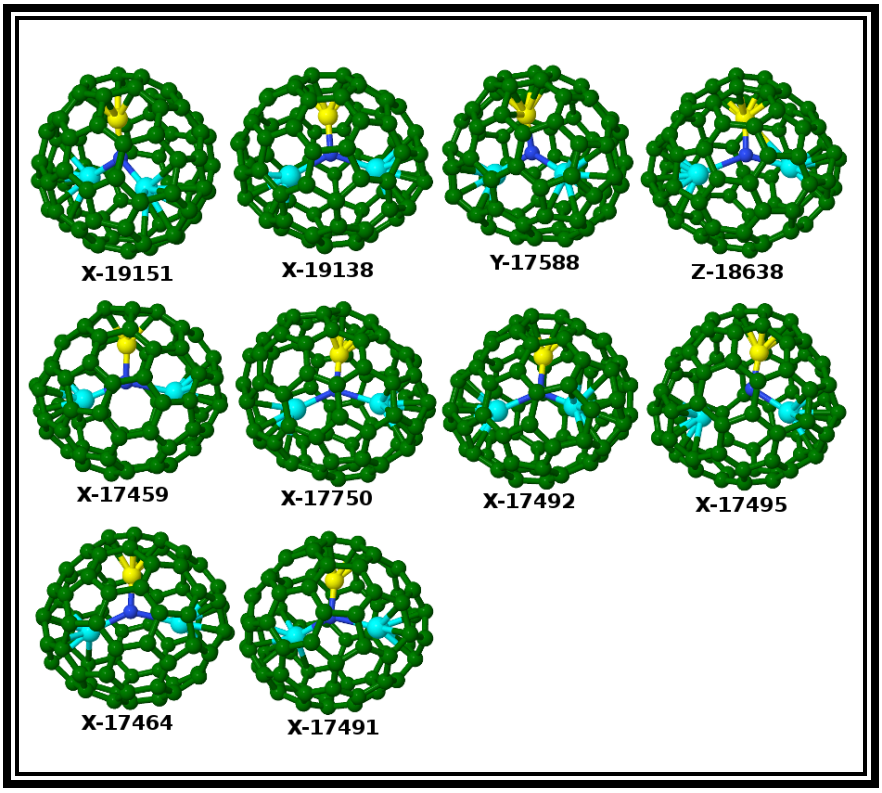

Figure 3.4: Optimized structures of $VSc_2N@C_{76}$ endohedral fullerenes. C, Sc, V and N atoms are represented by green, aqua, yellow and blue respectively.

There are no reports of homogeneous metal $M_3N@C_{2n}$ endohedral fullerenes between C_{70} and C_{78}. Encapsulation of the metal mixed nitride $DySc_2N$ in the C_{76} cage was reported by Yang et al. in 2007 and the cage structure reported in this case was the non-IPR isomer 17490 with C_s symmetry. [131] This was the first report of isolation of non-IPR C_{76} in the mixed metal nitride family. Here we also searched for the most stable mixed metal (i.e. vanadium, scandium) nitride

based C_{76} endohedral fullerenes through a series of calculations in which all the possible 19151 different structures were generated in a similar fashion as was done for other cages. The list of ten lowest energy isomers that we obtained from C_{76}^{-6} series are in perfect agreement with the AM1 optimized structures by Popov et al. [126] Among all the possible isomers of C_{76}, only two isomers 19151-T_d and 19150-D_2 have IPR-satisfying structure. Three hundred energetically most stable structures from previous step within the energy range of 2.36 eV were chosen as parent cages. The endohedral VSc_2N unit was introduced to generate 900 endohedral fullerenes using a procedure described earlier. The resulting endohedral fullerenes optimized in neutral state at PM6 level were found to lie within the energy range of 5.33 eV out of which the isomer X-19151 was obtained as the energetically most favorable isomer. Ten most probable isomers of endohedral fullerenes from PM6 level within the window of 0.64 eV were selected for further calculations and optimized at DFT level, which also showed the same isomer X-19151 as the most probable candidate. Here in X-19151 isomer, the endohedral unit shows slight deviation from a planar structure with sum of the angles of metallic atoms around central nitrogen being 356.6 degree. The V-N and Sc-N bond distances are 1.86 Å and 2.13 Å respectively, but those distances were 1.89 Å and 1.88 Å respectively in the separately optimized planar VSc_2N unit. In the isomer 19151 with T_d symmetry, there are four regions in which a hexagon is shared equally by three pentagons and three hexagons, and higher strain is observed in those regions due to higher concentration of the pentagons whereas other hexagons are shared by lower number of pentagons. From further structural analysis, it was observed that metal atoms are pointed towards those hexagons that are shared by three pentagons. The distance between the closest carbon from both Sc atoms are 2.28 Å, while vanadium is closer to the cage by 0.13 Å as compared to Sc-C distance. The successful entrapment of the Sc_2O unit in the same parent cage 19151 is reported

by Yang et al. and characterized by the techniques including UV/Vis/NIR absorption, mass and single-crystal X-ray diffraction.[132] An earlier DFT calculation by Zhao et al. on $Sc_2S@C_{76}$ also found the same isomer 19151 to be the lowest energy structure.[133] We have also included the isomer 17490, which is reported to encapsulate mixed metal nitride.[131] It is 0.45eV higher in energy than the lowest structure at our DFT level of calculation.

Table 3.3: Ten lowest energy isomers of $VSc_2N@C_{76}$ fullerenes, energy relative to the most stable structure in respective levels of theory, and the HOMO-LUMO gaps are presented. All the reported energies and HOMO-LUMO gaps are in the eV.

$VSc_2N@$	DFT energy (eV)	PM6 energy (eV)	H_L gap
C_{76}(X-17459)	1.17	0.58	0.26
C_{76}(X-17464)	1.59	0.45	0.61
C_{76}(X-17491)	1.59	0.31	0.61
C_{76}(X-17492)	1.52	0.4	0.43
C_{76}(X-17495)	1.58	0.59	0.74
C_{76}(X-17750)	1.50	0.64	0.45
C_{76}(X-19138)	0.26	0.48	0.29
C_{76}(X-19151)	0	0	0.27
C_{76}(Y-17588)	1.08	0.58	0.31
C_{76}(Z-18638)	1.12	0.55	0.60

The HOMO-LUMO gap ranges from 0.27 eV for the X-17459 to the 0.74 eV for the isomer X-17495 as given in Table 3. For the most stable isomer X-19151 the HOMO-LUMO gap is 0.29 eV. This value is larger than the HOMO-LUMO gaps for $Sc_3N@C_{76}$, $YSc_2N@C_{76}$, and $Y_3N@C_{76}$. Yang and et al. [132] have reported the HOMO-LUMO gaps of 0.14 eV, 0.18 eV,

and 0.10 eV in isomer 19151 for $Sc_3N@C_{76}$, $YSc_2N@C_{76}$, and $Y_3N@C_{76}$ respectively. Since the lowest energy isomer $VSc_2N@C_{76}$(19151) has magnetic moment 0, we have further optimized it by fixing the moment at different values of $1\mu_B$, $2\mu_B$, and $3\mu_B$. Similar to the $VSc_2N@C_{70}$ cluster, the isomer with moment $2\,\mu_B$ is only 0.02 eV higher in energy at the PBE level. However, this isomer has a much smaller HOMO-LUMO gap of 0.11 eV, which also shows that it will be more chemically unstable compared to the S=0 isomer.

In $VSc_2N@C_{76}$, HOMO-1 and HOMO are distributed over all metal atoms in the endohedral unit and carbon atoms throughout the whole cage, but again the most prominent contribution is by vanadium. These distribution patterns are different than that is observed in the $VSc_2N@C_{70}$ in which the contribution by scandium on HOMO and HOMO-1 is lower and only by the carbons from half part of the cage. The LUMO and LUMO+1 level in $VSc_2N@C_{76}$ are primarily localized on the metallic atoms and a few carbon atoms. These observations are also seen in the density of states plot (Figure S4) which shows significant contribution of vanadium d orbital and p orbital of carbon atoms to the HOMO level. The LUMO is again mostly contributed by vanadium d orbital and carbon p orbital along with scandium d orbital as well. The contribution of scandium on LUMO is higher than that on HOMO as shown in the orbital picture Figure 2.

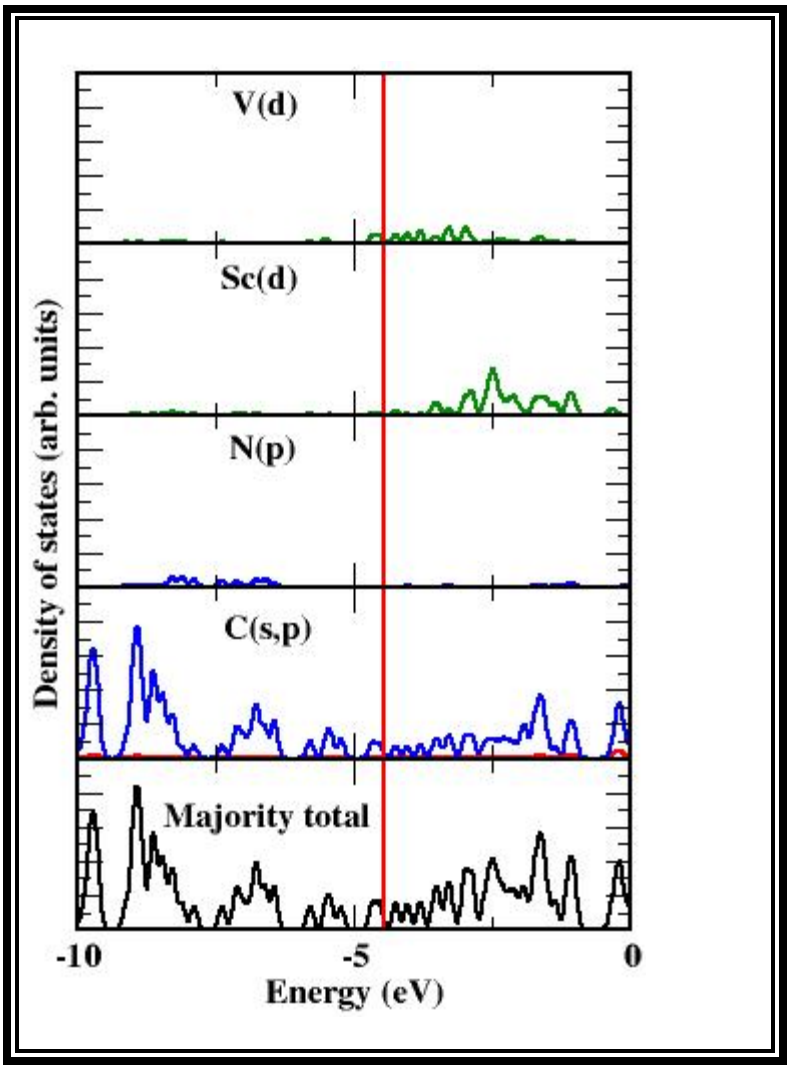

Figure 3.S4. DOS plot for $VSc_2N@C_{76}$

$VSc_2N@C_{78}$

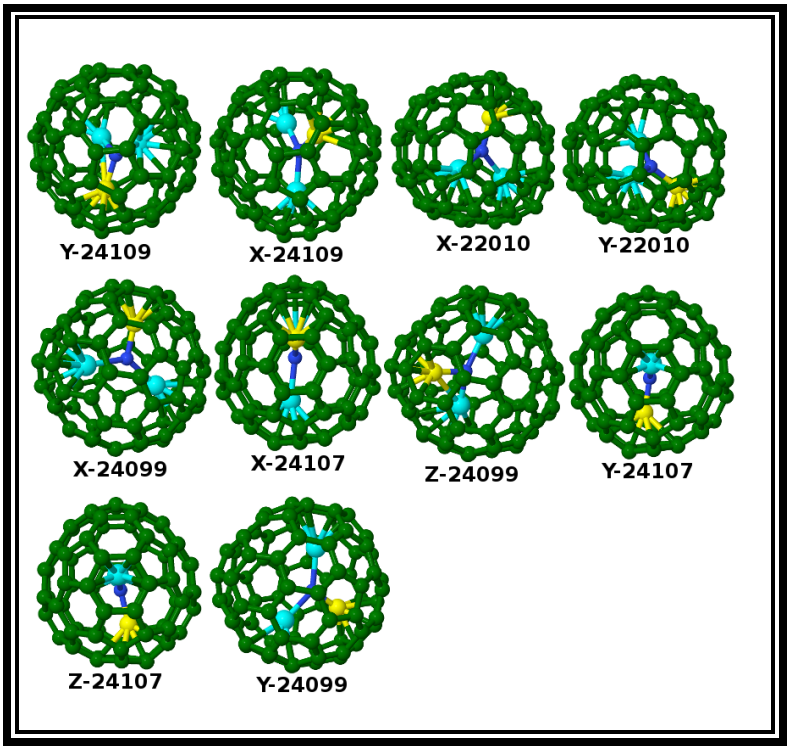

Figure 3.5: Optimized structures of $VSc_2N@C_{78}$ endohedral fullerenes. C, Sc, V and N atoms are represented by green, aqua, yellow and blue respectively.

Since the discovery of trimetallic nitride template endohedral fullerenes,[3] [87] many reports of encapsulation of transition metals in C_{78} cage have appeared: $Sc_3N@C_{78}$,[50] [134] $La_2@C_{78}$,[51] [135] $Ti_2C_2@C_{78}$, [136] and $Tm_3N@C_{78}$, and $Dy_3N@C_{78}$ were also isolated and characterized. [137] [115] There are 24109 different structures possible for C_{78}. Among them only five isomers obey IPR rule. These are $\mathbf{D}_3$ (24105), $\mathbf{C}_{2V}$ (24106), $\mathbf{C}_{2V}$ (24107), $\mathbf{D}_{3h}$ (24108), and $\mathbf{D}_{3h}$ (24109). [125] An extensive search for the most probable structure was performed. As mentioned earlier, we start with the optimization of all the possible structures in the hexanionic state (isomers 24109, 22010,

24107, 22646, and 24088 are the five most stable cages of C_{78}^{-6} series ordering from the lowes to the highest energy, the same order was reported by Le et al.) [138], from which three hundreds most probable isomers within the window of 3.16 eV were chosen as the parent cage to encapsulate VSc_2N endohedral unit. The VSc_2N unit was rotated along three different orientations resulting in 900 isomers of endohedral fullerenes and further optimized at PM6 level in which the energy window broadened to 7.55 eV, and the lowest ten most probable isomers were chosen for further calculation at DFT level. Ten of the DFT optimized structures are as shown in Figure 5. From both DFT and PM6 calculations, it was observed that the isomer Y-24109 is energetically the most favorable. The same cage was proposed to encapsulate endohedral unit Sc_3N in a study by Olmstead et al., [139] and similar planar structure of Sc_3N unit within the same isomer 24109 was verified through the X-ray analysis. [140] The parent cage 24109 has D_{3h} symmetry.

The endohedral VSc_2N unit maintains the planar structure in which V-N and Sc-N distances are 1.82 Å and 2.16 Å respectively. The closest carbon distances from Sc atoms and V atom are 2.26 and 2.16 Å respectively, and those carbon vertex are shared with three surface planes: two hexagonal and one pentagonal. The endohedral unit maintains the planar structure and is closer to the part of cage surface that has higher concentration of pentagons. The most stable cluster has a magnetic spin moment of $2\mu_B$ with other 24109 isomers of 0, 1, and $3\mu_B$ lying 0.48, 0.35, and 0.32 eV higher in energy respectively. For the lowest 10 isomers (Cf. Table 4) the HOMO-LUMO gap ranges from 0.16 eV to 0.51 eV. The calculated gap for the most stable complex (S=0) and (S=1) are 0.39 and 0.78eV respectively, which are higher than that of $VSc_2N@C_{76}$(X-19151). Echegoyen et al. using DFT calculations reported the HOMO-LUMO gap of 0.66 eV for the $Ti_2S@C_{78}$ on the same parent cage 24109. [138] Earlier DFT calculations by

Campanera et al. have shown that the isolated C_{78} cage has a HOMO-LUMO gap of 0.60 eV which increases to 1.24 eV when it encapsulates Sc_3N cluster. Thus based on the HOMO-LUMO gaps, the $VSc_2N@C_{78}$ fullerene such as $Ti_2S@C_{78}$ is chemically less stable than the $Sc_3N@C_{78}$. In $VSc_2N@C_{78}$, the HOMO, HOMO-1, LUMO, and LUMO+1 levels are mostly localized on vanadium and a few carbon atoms, and the contribution of scandium atoms increases significantly as moving from HOMO to LUMO level as shown in Figure 2. Similar picture is illustrated using density of states plot (Figure S5) in which significant contribution of vanadium d orbital and carbon p orbital on HOMO and LUMO levels is observed. Also the contribution of scandium d orbitals on LUMO level cannot be neglected.

Table 3.4: Ten lowest energy isomers of $VSc_2N@C_{78}$ fullerenes, energy relative to the most stable structure in respective levels of theory, and the HOMO-LUMO gaps are presented. All the reported energies are in the eV.

Systems	DFT deviation	PM6 deviation	H_L gap
C_{78}(X-22010)	0.52	0.60	0.51
C_{78}(X-24099)	1.06	0.09	0.47
C_{78}(X-24107)	1.08	0.56	0.38
C_{78}(X-24109)	0.29	0.45	0.38
C_{78}(Y-22010)	0.93	0.61	0.24
C_{78}(Y-24099)	1.33	0.47	0.26
C_{78}(Y-24107)	1.26	0.39	0.29
C_{78}(Y-24109)	0	0	0.39
C_{78}(Z-24099)	1.11	0.49	0.16
C_{78}(Z-24107)	1.26	0.39	0.29

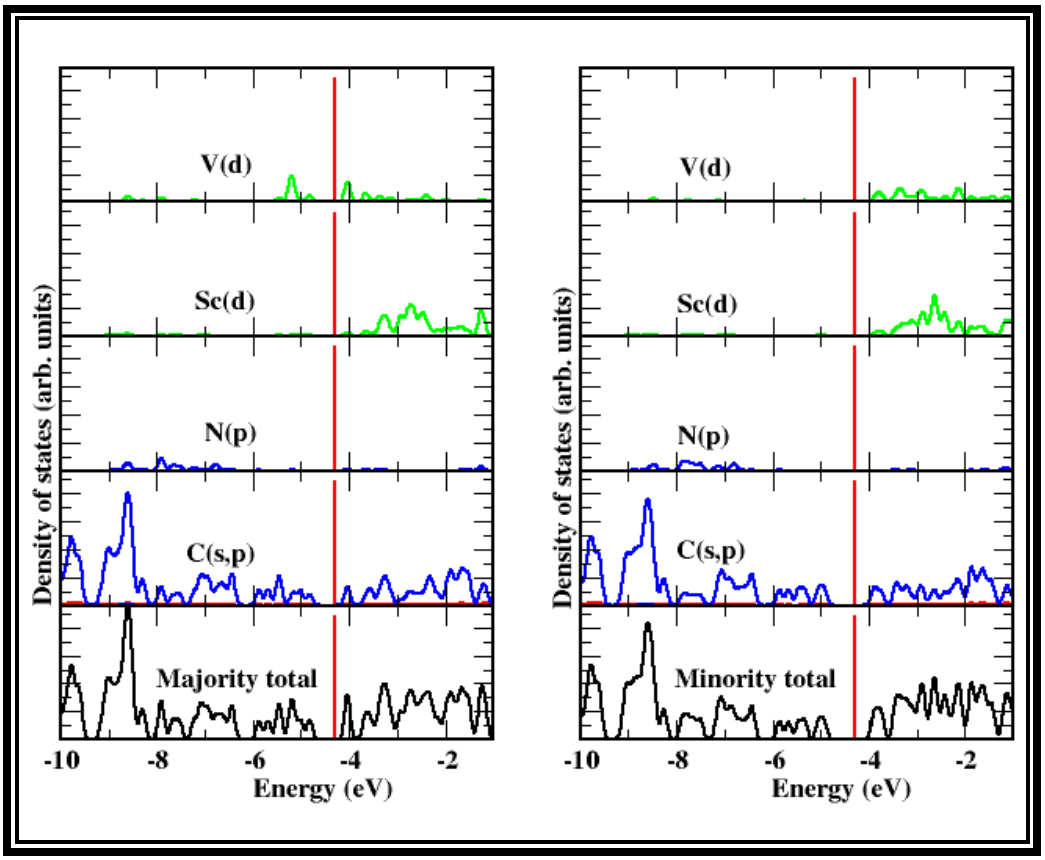

Figure 3.S5. DOS plot for $VSc_2N@C_{78}$

Chemical Stability

Table 3.5: Vertical ionization energy(vIP), vertical electron affinity(vEA), HOMO LUMO gap and the quasiparticle gap for the most stable isomers. All values are reported in eV.

VSc_2N@	vIP	vEA	H_L gap	QP gap
C_{70}(Y-7854)	5.59	2.28	0.46	3.31
C_{76}(Y-19151)	5.86	2.88	0.29	2.98
C_{78}(X-24109)	6.14	3.14	0.39	3.02
C_{80}(Y-31924)	6.43	3.09	0.41	3.34

The ionization potential and the electron affinity of molecules can provide information about the chemical stability of structure and can be useful in certain applications. For example, the C_{60} fullerene has high electron affinity and low reorganization energy and hence has applications as an electron acceptor in photovoltaics. The vertical ionization energy and vertical electron affinity for the most stable structures reported here are given in Table 5. The ionization potential increases for the larger cage size and ranges from 5.59 eV for $VSc_2N@C_{70}$(X-7854) to 6.43 eV for $VSc_2N@C_{80}$(Y-31924). The calculated vertical electron affinities range from 2.28 eV for $VSc_2N@C_{70}$ to 3.14 eV for $VSc_2N@C_{78}$(X-24109). The electron affinity and ionization potential are found to be nearly same for the nearly degenerate S=1 state of $VSc_2N@C_{76}$ cage with respective values of 2.90 and 5.84 eV. Jin et al. reported the similar trend of increase of ionization potential and electron affinity with the increase in cage size in which they included $Sc_3NC@C_{68}$, $Sc_3NC@C_{78}$ and $Sc_3NC@C_{80}$ endohedral fullerenes.[141] From the values of electron

affinity and ionization potential, it can be inferred that the reported clusters have not only high electron accepting capacity but rather they are stable against oxidation as well.

Energetic Stability

In order to check whether the encapsulation of endohedral units is thermodynamically favourable, the binding energies were calculated using

B.E(encapsulation energy) = E(endohedral@fullerene) - E(fullerene)- E(endohedral unit). The binding energies are 11.64 eV, 9.25 eV, 9.42 eV, and 11.91 eV for $VSc_2N@C_{70}$(Y-7854), $VSc_2N@C_{76}$(Y-19151), $VSc_2N@C_{78}$(X-24109), and $VSc_2N@C_{80}$(Y-31924) respectively. Again the binding energy per carbon atom in the parent cage is given by 7.59 eV, 7.64 eV, 7.65 eV, and 7.64 eV for C_{70}, C_{76}, C_{78}, and C_{80} respectively. The lower binding energy of C_{70} in isomer 7854 is more obvious due to three fused pentagons leading to the higher steric strain as compared with other IPR satisfying structures C_{76} (19151), C_{78} (24109), and C_{80} (31924) in which none of the pentagons touch each other. From reported encapsulation energies, it was observed that VSc_2N endohedral unit thermodynamically favors the C_{80} cage, and both the endohedral cluster VSc_2N and (C_{70}, C_{76}, C_{78}, and C_{80}) cages are better stabilized in the endohedral form.

Charge Transfer

To obtain the partial charges on atoms in the endohedral complexes, we used density derived electrostatic and chemical charges approach. An interface using fortran code was developed which outputs the density matrix and the converged Kohn-Sham orbital coefficients that can be used in the ChargeMole code.

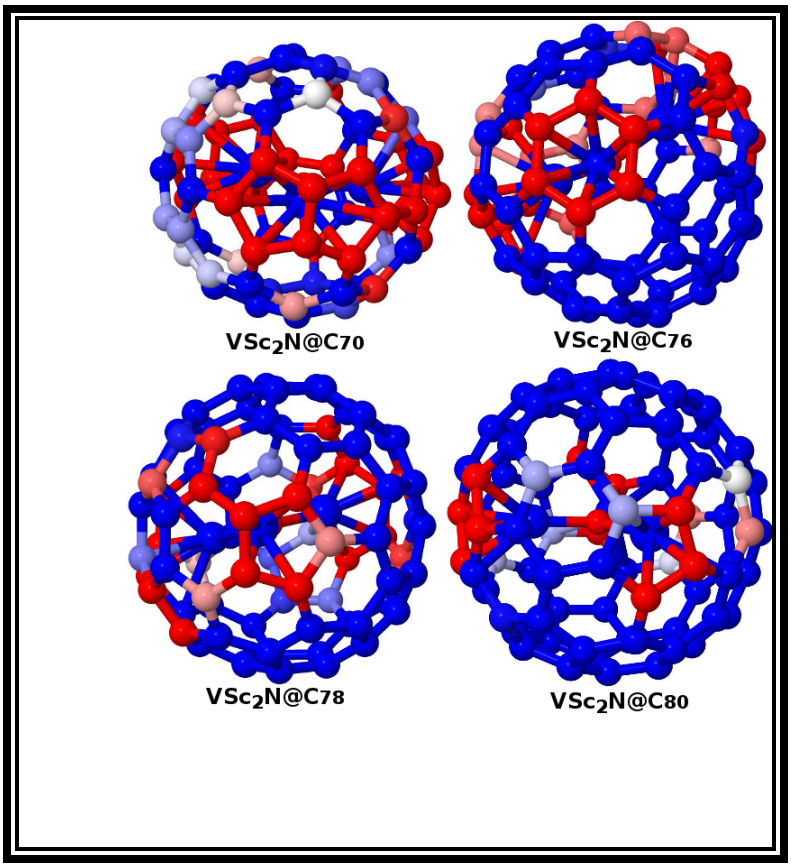

Figure 3.6: The lowest energy structures of $VSc_2N@C_{70}$, $VSc_2N@C_{76}$, $VSc_2N@C_{78}$ and $VSc_2N@C_{80}$ endohedral fullerenes. Dark red, pink, white, light blue and dark blue signify the different charge carried by the atoms given by negative, less negative, neutral, less positive and positive respectively.

By summing up all the atomic charges in endohedral unit, it can be inferred that there is significant amount of charge transfer from endohedral cluster to the outer cage. The charge transfer from the endohedral unit to the cages are 2.62e, 2.69e, 2.54e, and 2.63e in $VSc_2N@C_{70}$, $VSc_2N@C_{76}$, $VSc_2N@C_{78}$, and $VSc_2N@C_{80}$ respectively. The charge distribution is not uniform throughout the carbon on cage. In case of C_{70} (7854), maximum negative charge accumulation has observed on the 3 pairs of carbon atoms shared by two pentagons forming pentalenes and all

three metal atoms point toward the junction of fused pentagons. In the rest of the cages there are no fused pentagons but the maximum charges are carried by those carbon atoms which are located near to the positively charged metal ions. The charge transfer is further illustrated using colored picture as shown in Figure 6, in which red signify the electron accumulation while blue represents the electron deficient regions. Most of the red regions are observed on those carbon atoms which are closer to the endohedral metallic atoms.

In Summary, we have screened 8149, 19151, 24109, and 31924 different isomers of C_{70}, C_{76}, C_{78}, and C_{80} fullerenes cages respectively through a series of calculation using PM6 method followed by DFT optimizations to determine the structures of endohedral fullerenes with VSc_2N as endohedral unit. The host fullerene cages of the lowest energy structures of all the four types of endohedral fullerenes found in our elaborate searches have previously been reported to host different types of endohedral units. Only the $VSc_2N@C_{70}$ is found to have a non-IPR carbon cage. In all the fullerenes, the V atom is in +3 charge state, but the smaller cages showed an interesting pattern where two spin states with S=0 and S=1 are very close in energy with small structural difference. Such nearly degenerate spin states are not seen in the larger clusters of C_{78} and C_{80}. All the clusters have high ionization potential, and their electron affinities are higher than C_{60} except for the $VSc_2N@C_{70}$ cage with an electron affinity that is 0.4 eV lower than C_{60}. The charge transfer from the endohedral unit ranges from 2.5 to 2.7 electron in these clusters. These endohedral fullerenes are stable and can be useful as an electron acceptor.

Chapter 4: Density Functional Study on $V_2ScN@C_{2n}$(n=35, 38, 39 and 40) Endohedral Fullerenes

The interest on the endohedral metallofullerenes (EMF) grew intense after the synthesis of $La@C_{60}$ in the very first year of discovery of C_{60} in 1985. [142] Since then many reports of synthesis of EMF were documented as monometallofullerenes, dimetallofullerenes, trimetallo-fullerenes, metal nitride cluster-fullerenes (MNCF) etc., which make EMF class as the most abundant after bare cages fullerenes C_{60} and C_{70}. [143] [144] [145] [146] [147] [148] [149] [150] [151] [152] [153] Metal based endohedral clusters are known to transfer the electrons to the cage and endohedral fullerenes better represented by the salt like ionic structure as $(\text{metal-based clusters})^{+x}(\text{fullerenes})^{-x}$. [154]

Among metal-based endohedral fullerenes, trimetallo-fullerenes are less likely to form, in which Coulombic repulsion between the positive metal ions inside the cage plays important role to destabilize the system. However, there are some studies that report the formation of trimetallic endohedral fullerenes Er_3C_{74}, [148] Tb_3C_{80}, [146] Y_3C_{80} [147] and Dy_3C_{98} [149] but still there is a debate regarding the formation of trimetallo-fullerenes or carbide cluster fullerenes due to lack of experimental evidence. The inclusion of trimetallic clusters along with nitrogen greatly enhances the yield of endohedral fullerenes in which negatively charged nitrogen helps to reduce the Coulomb repulsion between metal ions leading to form the highly stable nitride cluster fullerenes (NCF) which has become the most widely studied group among the EMF family. Many reports were documented as the formation of homogeneous metal nitride cluster fullerenes (Sc, Gd, Tb, Dy, Tm, Lu etc.) [150] [155] [156] [157]. The NCFs family further populated along with the formation of mixed metal nitride clusters such as: $TiSc_2N$, [158] YSc_2N [159], $CeSc_2N$ [160], $NdSc_2N$, [161] $DySc_2N$ [161] etc. The scandium plays important role in the formation of NCFs either in the form of tri-scandium or scandium mixed-metal nitride fullerenes. The encapsulation of the homogeneous

metal nitride cluster in NCFs with the cages smaller than C_{80} are very rare and most of the studies were done on mixed scandium metal nitride fullerenes such as $Lu_2ScN@C_{68}$, $DySc_2N@C_{68}$, $DySc_2N@C_{76}$ etc. [162] [163] Wei et al. reported similar inhomogeneous NCFs using scandium and vanadium for the first time. [50] They synthesized NCFs using modified Kratschmer-Huffman Dc-arc discharge method with 5% N_2, VC (or V_2O_5), Sc_2O_3 and graphite. With three-step HPLC technique, they claimed the isolation of two NCFs as $VSc_2N@C_{80}$ and $V_2ScN@C_{80}$ in which they assign the cage structure to the isomer $I_h(7)/31924$ with icosahedral symmetry from the X-ray crystallography.

The study of vanadium based nitride cluster fullerenes are important not only because it is a new member in the NCFs family but also because it is a member along with titanium of the non lanthanide paramagnetic NCFs family that has been isolated to the date. [50] [164] In this chapter we present our studies on the V_2ScN cluster as the endohedral unit inside the same series of fullerenes, namely, C_{70}, C_{76}, C_{78} and C_{80} . The screening of all the possible 8149, 19151, 24109 and 31924 cages of C_{70}, C_{76}, C_{78} and C_{80}, respectively, were done through a series of calculations similar to those described in the previous chapter. These calculations led to the identification of the best isomers of V_2ScN encapsulating C_{70}, C_{76}, C_{78}, and C_{80} fullerenes. Further the detailed structural and electronic structure analysis of best cages for each size were done at DFT level.

Computational Method

The computational search for the most stable structure of fullerenes becomes more and more tedious as moving from lower to the higher cages due to abruptly increase in the number of isomers. The C_{70} fullerene itself has 8149 different structures possible, which further increases to 19151, 24109 and 31924 as moving to the higher fullerene cages C_{76}, C_{78} and C_{80} respectively.

The charge transfer from the endohedral unit to the outer cage plays very important role to stabilize the whole complex of endohedral fullerenes, [165] here in this study all the possible structures were optimized with six extra electrons using semi empirical quantum chemistry method MOPAC2009 [166] at PM6 level of theory. The configurational space further enriched by the possibility of rotation of endohedral cluster inside the cage but at some point we need to limit our calculation to minimize the computational cost thus we were limited to only few orientations of endohedral cluster for each fullerenes. The starting geometries of endohedral fullerenes were formed using cindy auxillary code developed in our lab in which three different rotations of separately optimized V_2ScN cluster were done in 300 lowest energy isomers from hex-anionic series leading to from 900 initial geometries of endohedral fullerenes, which were again optimized at PM6 level at neutral charge state. The series of calculation were followed by the DFT calculation using Vienna Ab initio Simulation Package (VASP) code on less than fifty lowest energy structures resulted from PM6 level of theory. Finally, ten lowest energy structures resulted from previous step were carried out using NAVAL Research Laboratory Molecular Orbital Library (NRLMOL) code [67] [70] [68] at all electron level in which the PBE exchange-correlation functional [167] within the generalized gradient approximation with large Gaussian basis set specially optimized for the PBE exchange-correlation functional were employed. [69] The number of primitive Gaussians and number of functions used for s- p- and d- type for each atom are listed as in the Table 1. Also a supplementary function is provided in each d-type for every atom. The partial charges were obtained using the density derived electrostatic and chemical net atomic charges as implemented in the ChargeMol code. [168] [169]

Table 4.1: The number of s- p- and d- type functions, number of bare (primitive) Gaussians, and exponent range used in each type of atoms.

Atom	s-type	p-type	d-type	Bare Gaussians	Exponent range
C	5	4	3	12	2.22×10^4 -0.077
N	5	4	3	13	$5.18 \times 10^4 - 0.25$
Sc	7	5	4	19	$1.57 \times 10^6 - 0.035$
V	7	5	4	20	$3.11 \times 10^6 - 0.038$

Results and Discussions

$V_3N@C_{80}$

Successful entrapment of Sc_3N within C_{80} was reported by Harry Dorn and collaborators for the first time in 1999 [157], which is the first report for the whole NCFs family. Interestingly, this novel material $Sc_3N@C_{80}$ endohedral fullerene showed the higher kinetic stability due to larger HOMO-LUMO gap and established itself as the most abundant after C_{60} and C_{70} even within the fullerene community. The C_{80} fullerene cage is known to encapsulate not only homogeneous metal nitride clusters such as Gd_3N, [155] Dy_3N, [156] Tm_3N [150] etc. but also mixed metal nitride clusters (MMNC) such as $Gd_xSc_{3-x}N(_{x=0-2})$, [151], [170] , $Lu_xSc_{3-x}(_{x=0-2})$, [171] $Ho_xSc_{3-x}(_{x=0-2})$ [172] etc. The encapsulation of similar MMNCs with vanadium and scandium was reported by Wei et al and the cage structure is assigned to the $I_h(7)C_{80}$ with icosahedral symmetry. [50] Here, in order to validate our search method we did the calculations on all the possible isomers of C_{80} (i.e

31924 isomers) with V_2ScN clusters through a series of calculation as mentioned above. All the optimized isomers in hexanionic series at PM6 level of theory fitted themselves within the window of 25.09 eV and isomer 31924 was found as the most stable structure of C_{80}^{-6} fullerene series. The encapsulation of endohedral units V_2ScN along three different orientations were done on 300 lowest energy isomers from hex-anionic series within an energy window of 4.51 eV. The resulting 900 isomers of $V_2ScN@C_{80}$ endohedral fullerenes were again optimized at same level of theory in neutral charge state and were found to lie within an energy window of 5.55 eV. Twenty lowest energy structures of $V_2ScN@C_{80}$ within the 0.97 eV from previous step were chosen for further calculation and optimized at DFT level. Ten isomers from the series are shown in the Figure-1. Among all competing structures of $V_2ScN@C_{80}$ endohedral fullerenes, isomer $V_2ScN@C_{80}$(X-31922) was selected as the most probable isomer at PM6 level, where as $V_2ScN@C_{80}$(Y-31924) became most favorable one at DFT level, which is 1.41eV lower in energy as compared with isomer X-31922. The same parent cage 31924(I_h) was reported and characterized as the $V_2ScN@C_{80}$ endohedral fullerene in the experimental work. [50] We have made some of the structural observation in $V_2ScN@C_{80}$ (31924) complex in which endohedral unit maintains almost planar structure with the sum of angles around center N atom (i.e. ∠MNM) is 359.7. Similar planar structure of V_2ScN unit was reported by Wei et al. [50] All the bond distances of metal ions from nitrogen are different, and are given by V(i)-N(1.88Å), V(ii)-N(1.95Å) and Sc-N(2.19Å). The closest C-M^{ion} distances are given by V(i)-C(2.26Å), V(ii)-C(2.19Å) and Sc-C(2.27Å), in which each closest carbons is shared by two hexagons and a pentagon. The orientation of each metal ion is different in which V(i/ii) is pointed towards the center of a hexagon/pentagon where as scandium is orientated towards a vertex (i.e. carbon),

which is shared by two hexagons and a pentagon. Wei et al. reported the orientation of each metal ion toward the junction of a pentagon and two hexagons.[50]

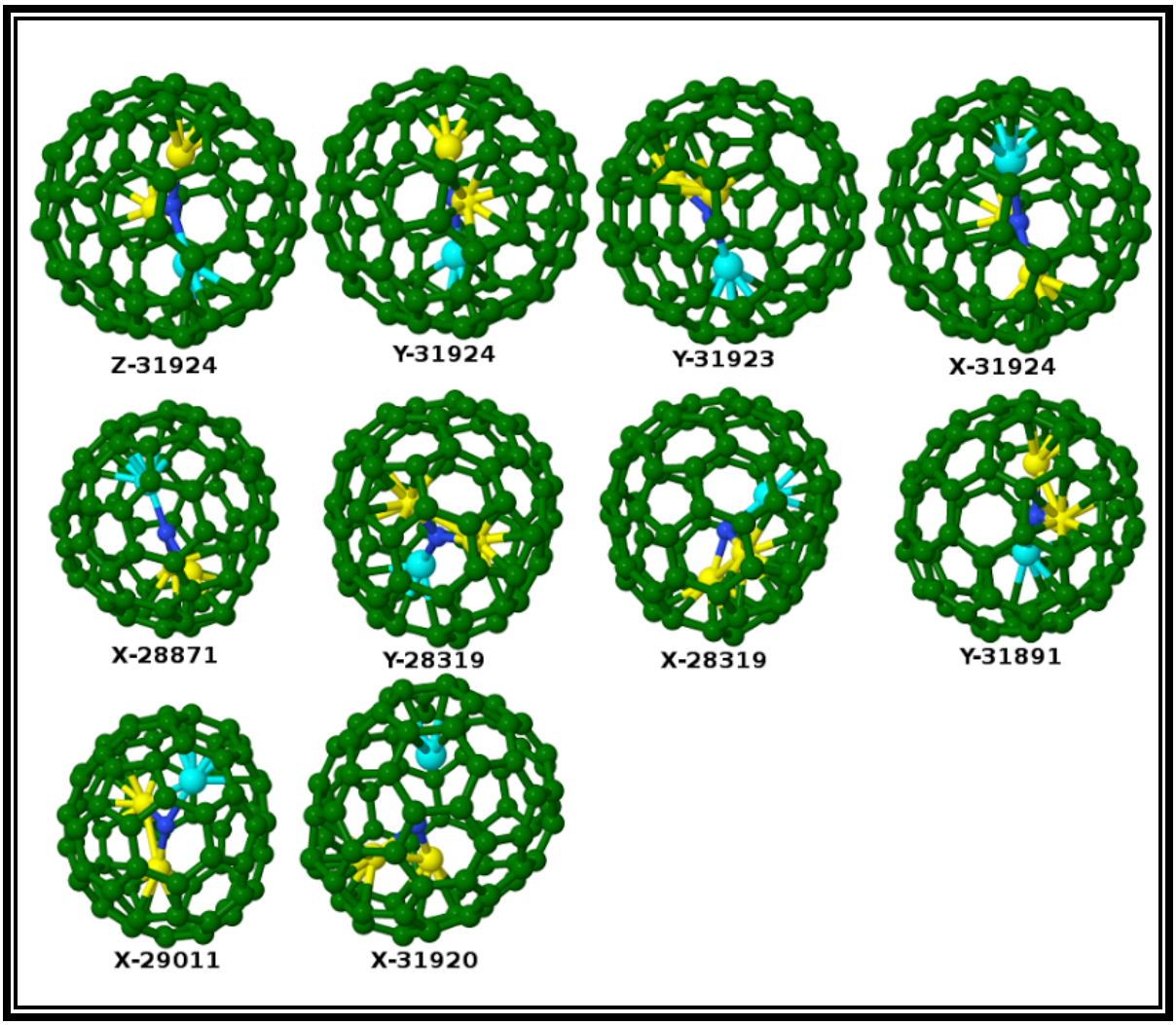

Figure 4.1: Optimized structures of $V_2ScN@C_{80}$ endohedral fullerenes. Carbon, Scandium, Vanadium and Nitrogen atoms are represented by green, aqua, yellow and blue respectively.

Table 4.2. Ten lowest energy isomers of $V_2ScN@C_{80}$ fullerenes, deviation energies were calculated with reference to the most stable structure in respective levels of theory and HOMO LUMO (H_L) gaps are also presented. All the reported energies are in eV.

$V_2ScN@C_{80}$	DFT	PM6	H_L gap	# of unpaired electrons
X31920	2.67	0.59	0.15	4
X29011	2.46	0.58	0.49	0
Y31891	2.20	0.65	0.29	0
X28319	2.18	0.49	0.35	0
Y28319	2.01	0.54	0.4	0
X28871	1.80	0.74	0.35	0
X31924	0.66	0.84	0.18	2
Y31923	0.47	0	0.35	0
Y31924	0.00	0.84	0.23	4
Z31924	0.00	0.84	0.23	4
X31922	1.41		0.20	2

.

The HOMO-LUMO gaps for ten most stable candidates were also reported in the Table 1, which ranges from 0.15 to 0.49 eV. The observed H_L gap in the $V_2ScN@C_{80}$ (Y/Z-31924) is 0.23 eV. Popov et al. reported the H_L gap of 1.46eV for the $Sc_3N@C_{80}$ (31924) at DFT level of theory. [173] Some of the DFT optimized $V_2ScN@C_{80}$ endohedral fullerenes have magnetic moment of 4 μ_B including the lowest energy structure $V_2ScN@C_{80}$ (Y/Z-31924). The magnetic moment arises due to the partially filled d-orbital of vanadium atoms. The localization of the spin densities on V^{3+} ions along with magnetic moment of 4 μ_B in $V_2ScN@C_{80}$ (I_h) was reported by Wei et al. at GGA-PBE level of theory. [50]

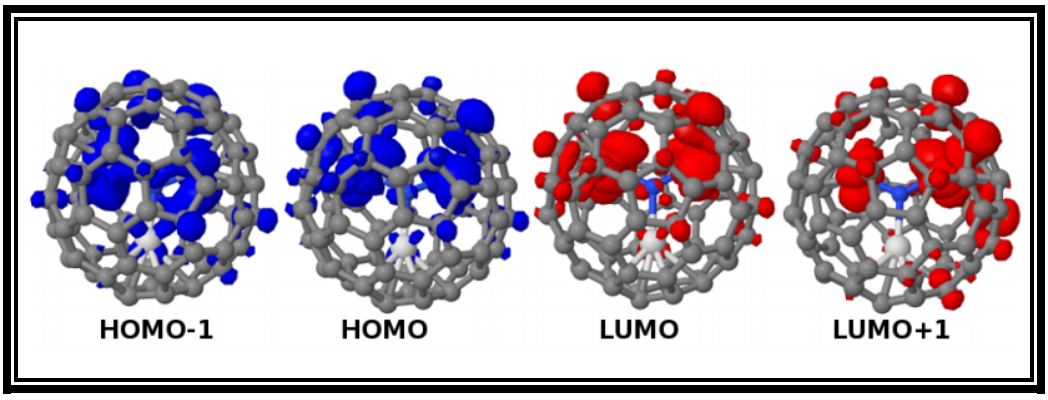

Figure 4.2: The molecular orbital plot for most probable cage of $V_2ScN@C_{80}$ (X-31924).

We have also plotted the molecular orbital density surfaces of $V_2ScN@C_{80}$ as shown in Figure-2, in which it was observed that HOMO-1 and HOMO are mostly contained on vanadium with the shape similar to *d* orbital having four lobes and the contribution of scandium decreases

significantly as moving from HOMO-1 to HOMO level. Again the dominating effect of vanadium atoms were observed on LUMO and LUMO+1.

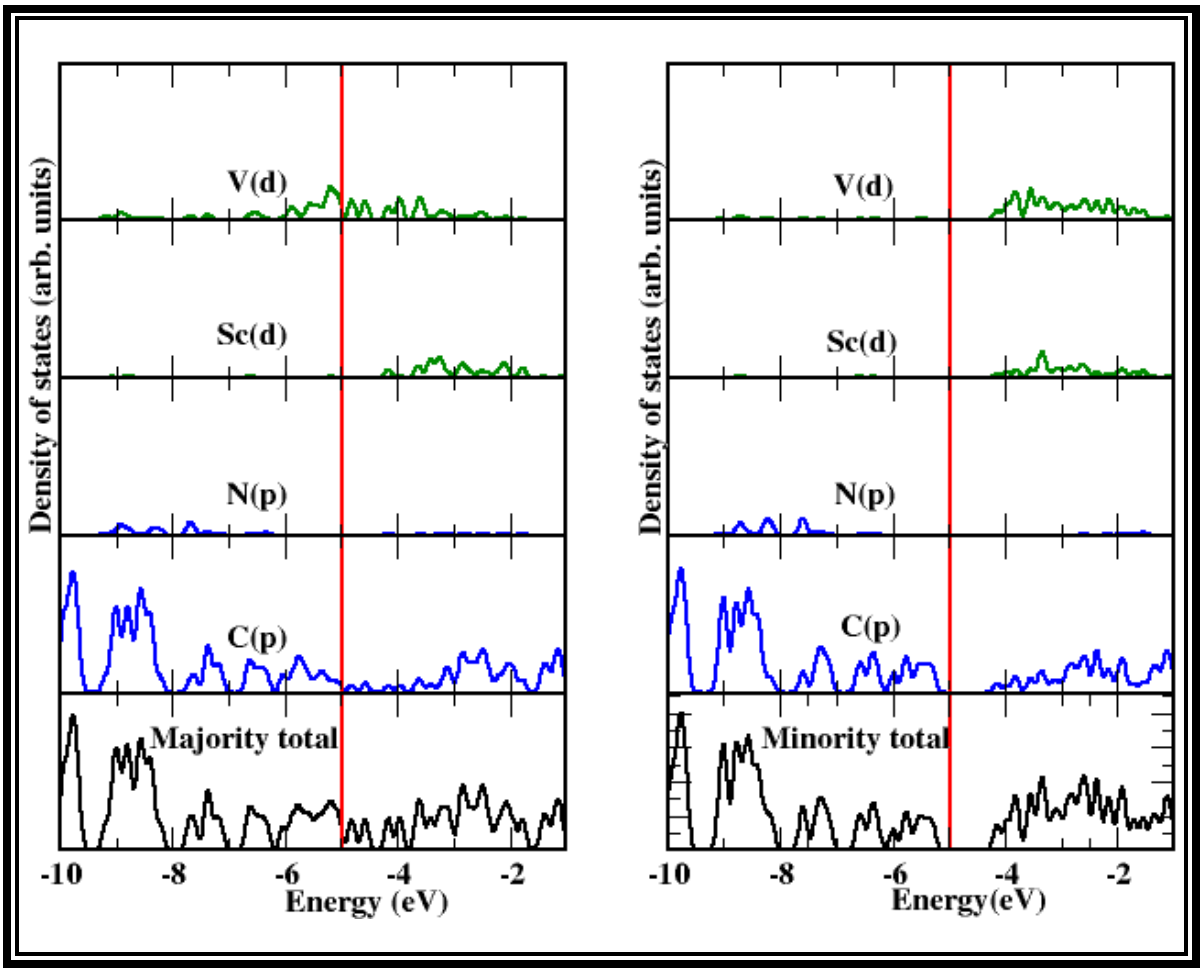

Figure 4.3: Density of states plot for the $V_2ScN@C_{80}$ (31924) blue, green and black curves indicates contribution due to p, d and majority(left)/minority(right) total respectively. The red vertical line is the Fermi level.

The molecular orbital picture is further illustrated using density of states plot, in which HOMO and LUMO level is mostly contributed by vanadium d and carbon p orbitals. The density of states difference between majority and minority spin carrier mainly observed for the vanadium

d orbitals, which further illustrate the observed magnetic moment in $V_2ScN@C_{80}$ (31924) endohedral fullerene.

$V_2ScN@C_{70}$

A similar search method as done for C_{80} is also adopted here in case of C_{70} cage, in which 300 lowest energy cages from hex-anionic series within the window of 2.43 eV were selected as the parent cage for endohedral fullerenes $V_2ScN@C_{70}$. After impregnating the endohedral units V_2ScN along three different directions, the resulting 900 isomers of endohedral fullerenes are optimized at PM6 level manage themselves within the energy range of 5.14 eV. The 39 lowest energy structures of $V_2ScN@C_{70}$ from previous step within the energy window of 0.41 eV were selected for further calculation and optimized at DFT level using VASP and NRLMOL codes. Among 900 competing structures of $V_2ScN@C_{70}$ endohedral fullerenes, isomer X-7887 was found to be the most probable isomer at both semi empirical and DFT level of calculation, which is iso-energetic with X-7854 at DFT level. The same parent cage 7854 is known to encapsulate Sc_3N unit. There are three fused pentagons in the isomer 7854 and endohedral unit V_2ScN maintains the planar structure in which two vanadium atoms are closer to each other as compared to scandium. Among three metal ions, two of them are pointed towards the fused pentagons and third one towards a hexagon, which is again connected to the fused pentagons. The closest carbon atom from scandium is at a distance of 2.32 Å in which the carbon is shared by two pentagons and a hexagon. The closest M-C distances reduced as moving to the vanadium atoms and are given by 2.09 Å and 2.15 Å in which these carbon atoms are shared by a hexagon and two pentagons, and all hexagons respectively. The Sc-N, V-N(i) and V-N(ii) bond distances are given by 2.31 Å, 1.78 Å and 2.09 Å. The similar orientation of endohedral unit was observed in

iso-energetic isomer X-7887, in which Sc-N, V-N(i) and V-N(ii) bond distances are given by 2.31 Å, 1.79 Å and 2.09 Å respectively and the closest carbon atoms from each metal ions are given by Sc-C (2.31 Å), V(i)-C(2.14 Å) and V(ii)-C(2.11 Å). Among ten lowest energy isomers only one Y-7892 is reported with the moment of 2 μ_B, whereas rest of the endohedral complexes ended with zero moment in their DFT optimized structures. For the lowest energy structure, we run the calculation with fixed moment of 1, 3/2 and 2 μ_B in which, spin states S=0 and S=1 of $V_2ScN@C_{70}$ (7854) are isoenergetic, whereas S=3/2 and S=2 states are higher in energy by 0.22 eV and 0.31eV respectively with that of S=1 state.

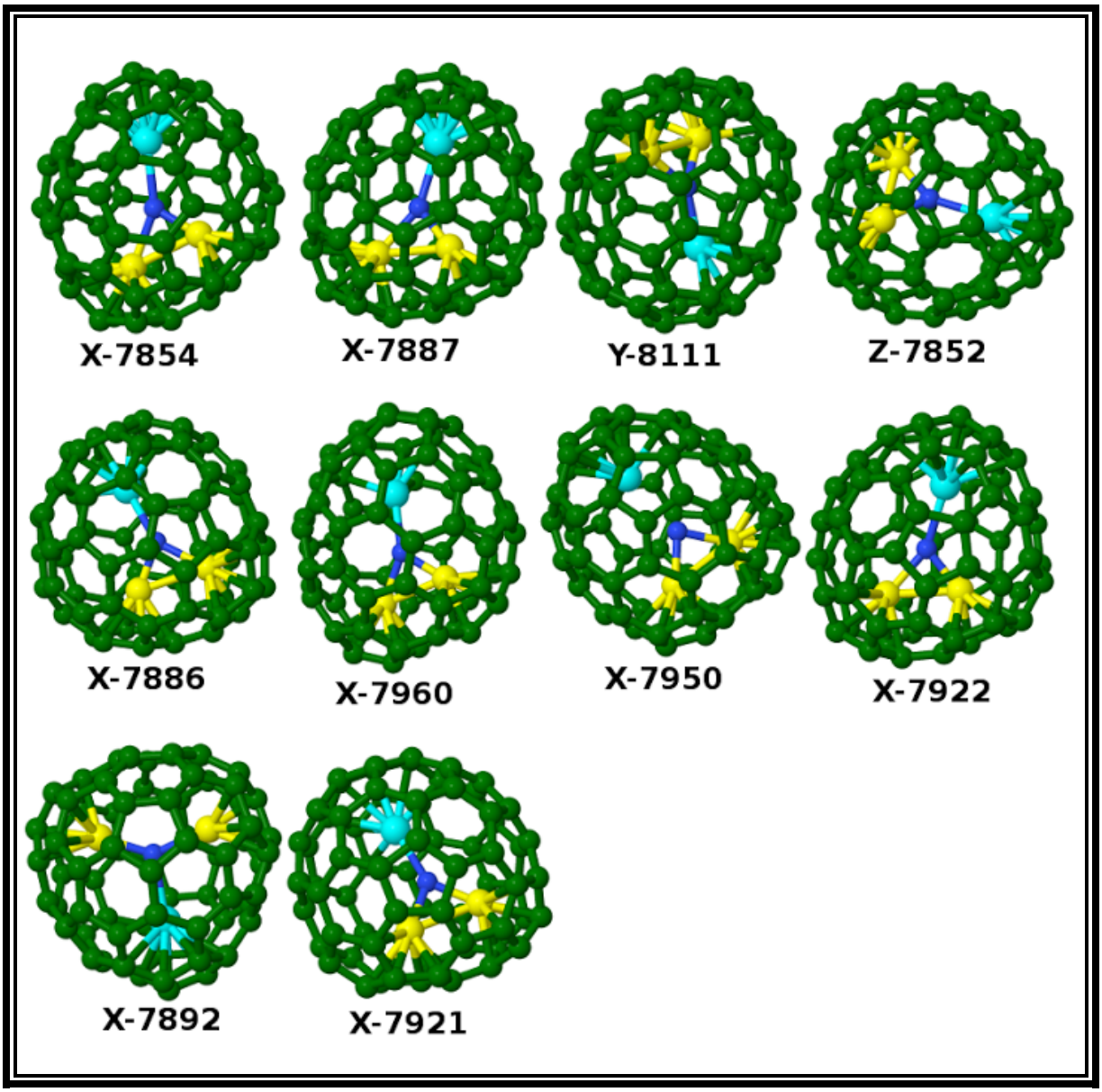

Figure 4.4: Optimized structures of $V_2ScN@C_{70}$ endohedral fullerenes. Carbon, Scandium, Vanadium and Nitrogen atoms are represented by green, aqua, yellow and blue respectively.

The HOMO LUMO gap of ten lowest energy isomers of $V_2ScN@C_{70}$ endohedral fullerenes are listed in the Table 3, and are ranges from 0.29 to 0.75eV, where as this gap is only 0.38eV in the most stable structure X-7854.

Table 4.3: Ten lowest energy isomers of $V_2ScN@C_{70}$ fullerenes, deviation energies were calculated with reference to the most stable structure in respective levels of theory and HOMO LUMO (H_L) gaps are also presented. All the reported energies are in eV.

$V_2ScN@C_{70}$	DFT	PM6	H_L gap	# of unpaired electrons
X7921	0.70	0.47	0.4	0
Y7892	0.32	0.12	0.45	2
X7922	0.63	0.66	0.34	0
X7950	0.51	0.42	0.75	0
X7960	0.39	0.42	0.29	0
X7886	0.37	0.61	0.38	0
Z7852	0.28	0.25	0.43	0
Y8111	0.23	0.54	0.56	0
X7887	0.00	0.00	0.44	0
X7854	0.00	0.61	0.44	0
Y7854	0.97	1.39	0.38	0

In $V_2ScN@C_{70}$, The dominant contribution of both vanadium atoms on frontier molecular orbitals: HOMO-1, HOMO, LUMO and LUMO+1 was observed as shown in Figure 4.5, in

which the orbitals having four lobes show the strong d orbital contribution, where as the contribution of scandium was feeble. Thus addition or removal of an electron mostly involves in the vanadium d orbital.

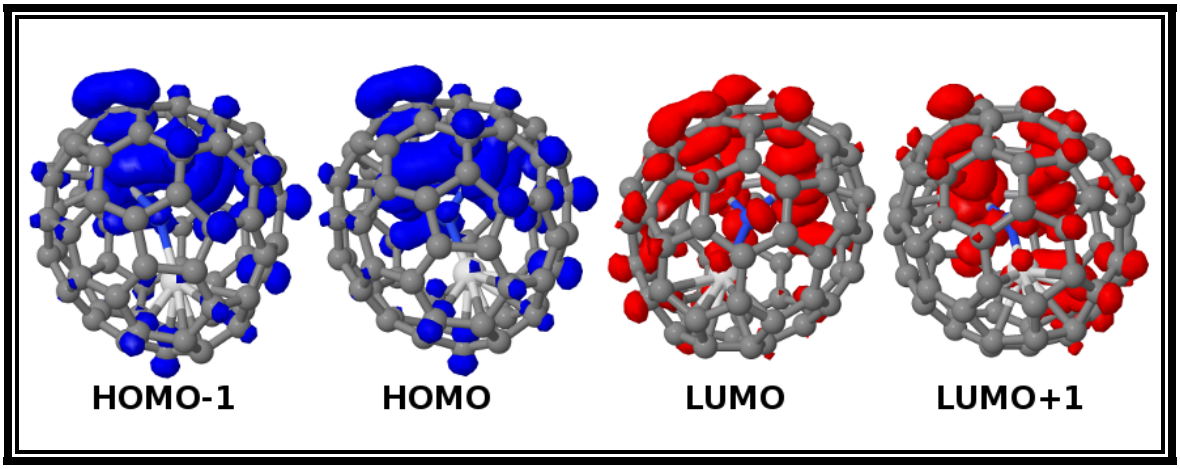

Figure 4.5: The molecular orbital plot for most probable cage of $V_2ScN@C_{70}$ (X-7854). HOMO-1, HOMO, LUMO and LUMO+1 from left to right.

$V_2ScN@C_{76}$

Yang et al. reported the successful encapsulation and characterization of mixed metal nitride cluster $DySc_2N$ in the C_{76} cage for the first time, in which they assign the cage structure to the isomer 17490 with Cs symmetry. [174] Here in this study we tried to explore the energetic stability and electronic structure of the similar mixed metal nitride endohedral fullerenes $V_2ScN@C_{76}$ but with vanadium. Similar search method as done for previous cages was adopted with semi-empirical method followed by DFT calculations. The encapsulation of V_2ScN endohedral unit along three different orientations were done on the 300 lowest energy structures of C76 within the window of 2.36eV resulting from hex-anionic series. The resulting 900

isomers of $V_2ScN@C_{76}$ optimized at PM6 level are able to manage themselves within the window of 5.52 eV. The DFT calculations were done on the 50 lowest energy structures of $V_2ScN@C_{76}$ metal nitride fullerenes within the window of 1.16 eV using VASP and NRLMOL codes. Ten of the lowest energy structures are as shown in Figure 6. Among 19151 competing structures of $V_2ScN@C_{76}$ endohedral fullerenes, isomer X-19151 was obtained as the lowest energy structure at both PM6 and DFT level of theory. The same parent cage 19151 was found energetically most favorable one even with VSc_2N endohedral unit in our previous study. The isomer 19151 has higher Td symmetry. In $V_2ScN@C_{76}$ (X-19151), the endohedral unit maintains the planar structure and the stretching of all three metal-N bonds were observed as moving from separately optimized V_2ScN cluster. The closest carbons from each metal ions are given by Sc-C (2.25 Å), V(i)-C (2.13 Å) and V(ii)-C (2.11 Å) and which are shared by two hexagons and a pentagon. The vanadium atoms are separated by 3.53 Å, where as this distance was 2.51 Å in the $V_2ScN@C_{70}$ (X-7854).

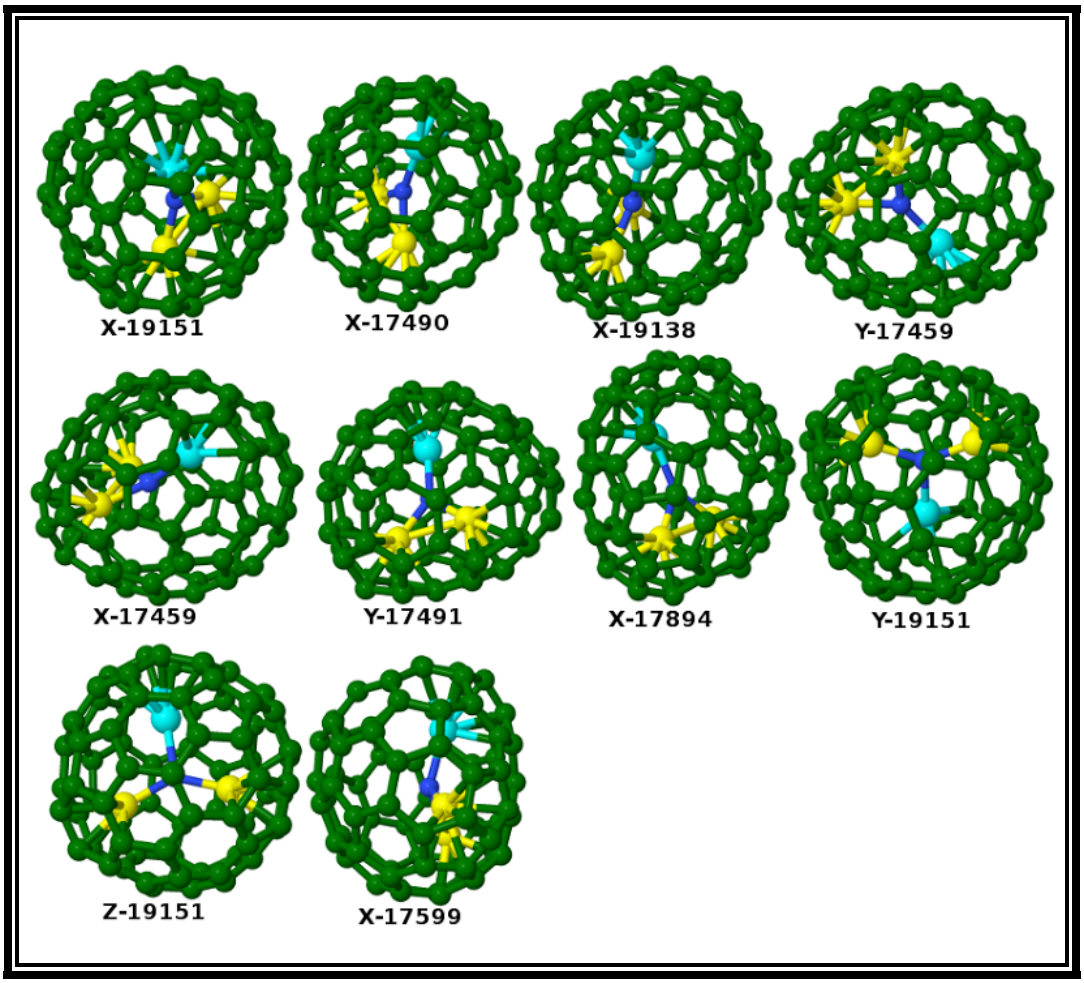

Figure 4.6: Optimized structures of $V_2ScN@C_{76}$ endohedral fullerenes. Carbon, Scandium, Vanadium and Nitrogen atoms are represented by green, aqua, yellow and blue respectively.

The HOMO-LUMO gap in the ten lowest energy isomers ranges from 0.03 to 0.56 eV at DFT level of calculation, among which the most stable structure X-19151 is observed with small gap of 0.10 eV. This gap is further reduced in other isomers Y-/Z-19151. The same parent cage 19151 along with Y_3N, Sc_3N and YSc_2N as endohedral unit was reported with similar lower gap 0.10, 0.16 and 0.18 eV respectively at DFT level of theory. [174] As we know that the HOMO

LUMO gaps are the indicator of the chemical stability, thus due to having lower gap in most stable structure we have also included the 2nd lowest structure i.e. X-19138 in our detail electronic and geometrical analysis, which is only 0.10 eV higher in energy than the isomer 19151 but has higher gap of 0.31 eV at DFT level of calculation. The same parent cage 19138 is reported to encapsulate metal ion Sm^{+2}. [175] There is only one pair of fused pentagons in isomer 19138, in which one of the vanadium is oriented towards it. The endohedral unit V_2ScN maintains almost planar structure and the sum of M-N-M is given by 358.8 degree. The M-N bond distances are given by V(i)-N(1.87 Å), V(ii)-N(1.95 Å) and Sc-N(2.07 Å). The distance of closest carbon atoms from each M ions are given by V(i)-C(2.1 Å), V(ii)-C(2.07 Å) and Sc-C(2.25 Å). From the orbital picture, it can be observed that the HOMO-1 and HOMO is mostly contained on carbon atoms and some of the contribution by metal atoms as well. The picture is different as moving to the LUMO in which the contribution of vanadium atoms increases whereas it decreases from carbon atoms as compared with HOMO and HOMO-1 levels. Almost similar picture of LUMO+1 with that of LUMO level was observed as shown in Figure-7. The orbital picture is further illustrated by the density of states plot as shown in Figure-8, in which the HOMO level is mostly contributed by carbons p orbital and partly by vanadium d orbital, where as the contribution of the vanadium d orbital increases significantly as moving to the LUMO level. Also the major difference in the majority and minority spin carriers are observed in the vanadium d orbital, which shows the strong vanadium d orbital contribution on the magnetic moment of $V_2ScN@C_{76}$ (X-19138) (i.e. 2 μ_B).

Table 4.4: Ten lowest energy isomers of $V_2ScN@C_{76}$ fullerenes, deviation energies were calculated with reference to the most stable structure in respective levels of theory and HOMO LUMO (H_L) gaps are also presented. All the reported energies are in eV.

$V_2ScN@C_{76}$	**DFT**	**PM6**	**H_L gap**	**# of unpaired electrons**
X17599	1.08	1.02	0.56	0
Z19151	0.57	0.83	0.03	2
Y19151	0.57	0.84	0.05	2
X17894	0.90	0.77	0.42	0
Y17491	0.82	1.04	0.47	0
X17459	0.80	0.88	0.27	0
Y17459	0.45	0.88	0.47	0
X19138	0.10	0.68	0.31	2
X17490	0.28	1.00	0.44	0
X19151	0	0	0.12	2

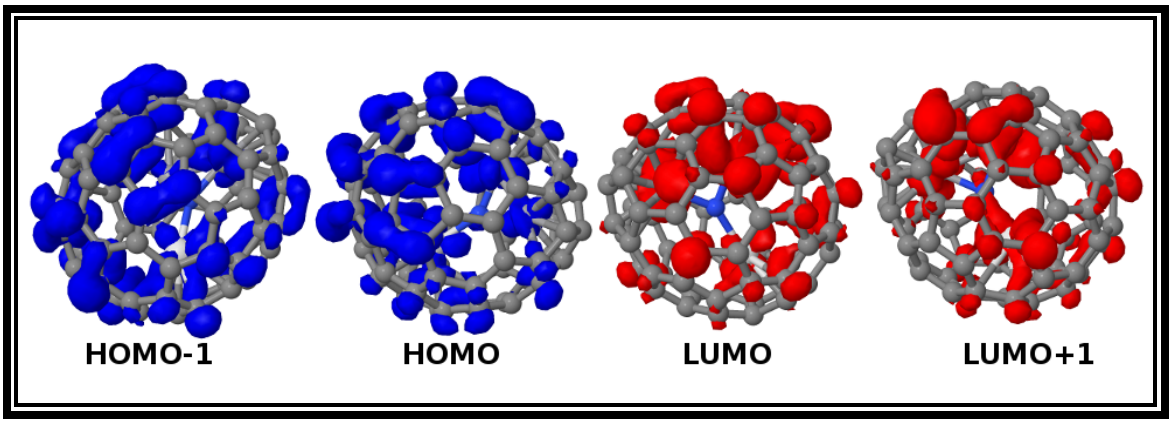

Figure 4.7: The molecular orbital plot for most probable cage of $V_2ScN@C_{76}$(X-19138). HOMO-1, HOMO, LUMO and LUMO+1 from left to right.

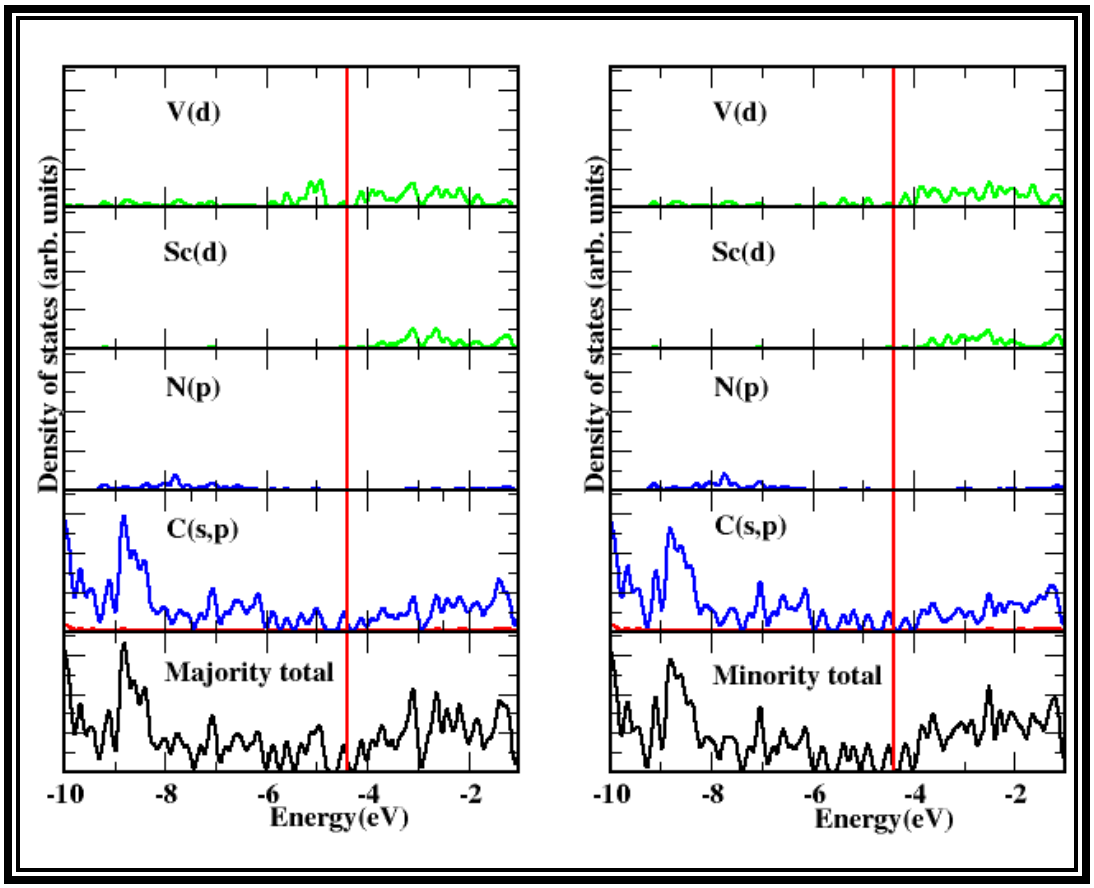

Figure 4.8: Density of states plot for the $V_2ScN@C_{76}$ (19138) blue, green and black curves indicates contribution due to p, d and majority(left)/minority(right) total respectively. The red vertical line is the Fermi level.

$V_2ScN@C_{78}$

C_{78} fullerenes are important in the tri-metallic nitride endohedral fullerenes family not only due to successful encapsulation of Sc_3N [176] unit but also it can act as the threshold for some of the larger clusters like Tm_3N, [177] Dy_3N [178] with significant yield. The number of isomers increases abruptly for larger cage fullerenes. There is increase of 4958 isomers even stepping up

from C_{76} to C_{78} fullerene. Thus the search for the most stable candidate becomes more and more tedious as moving to the higher fullerenes. Again the extensive study on all the isomers of C_{78} with V_2ScN as endohedral unit has been done in a similar fashion as adopted in the previous cages. The encapsulation of endohedral clusters along three different orientations were done on 300 cages resulting from hex-anionic series within the energy window of 3.16 eV leading to form 900 complexes which were again optimized at PM6 level of theory. The resulting isomers of $V_2ScN@C_{78}$ endohedral fullerenes accommodate themselves within the energy range of 4.88 eV. Ten isomers of $V_2ScN@C_{78}$ endohedral fullerenes within the window of 0.72 eV from previous step were selected for further calculation at DFT level. Among 24109 competing candidates, isomer X-24109 became the most probable structure of $V_2ScN@C_{78}$ endohedral fullerenes at both PM6 and DFT level of theory, in which the parent cage follow the IPR-satisfying structure. The same parent cage was reported as the lowest energy structure of $VSc_2N@C_{78}$ endohedral fullerenes in our previous study. In $V_2ScN@C_{78}$ (X-24109), endohedral unit V_2ScN maintains almost planar structure with the sum of M-N-M angles around center N atom is 357.7 degree. Campanera et al. reported perfect planar structure of Sc_3N in the same parent cage 24109 of C_{78}. [179] The Sc-N (2.09Å) bond is longer than other two V-N bonds by 0.21Å. As compared with our previous study on $VSc_2N@C_{78}$, stretching of V-N bond distance was observed as moving to the $V_2ScN@C_{78}$, where as Sc-N bond distance decreases by increasing the number of vanadium atoms in the $M_3N@C_{78}$ (i.e. M= V or Sc) endohedral fullerene. The M-M distance between two vanadium atoms is 2.58Å, where as this distance increases by more than 1 Å for M(Sc)-M(V(i/ii). The vanadium atoms are closer to the cage as compared with scandium and the closest metal-carbon distances are given by (V(i/ii)-C) 2.09 Å and (Sc-C) 2.23 Å, in which two vanadium are orientated toward the pentagon where as

scandium pointed toward the carbon vertex shared by two hexagons and a pentagon. All of the closest carbon atoms from three metal ions are shared by two hexagonal and a pentagonal surfaces.

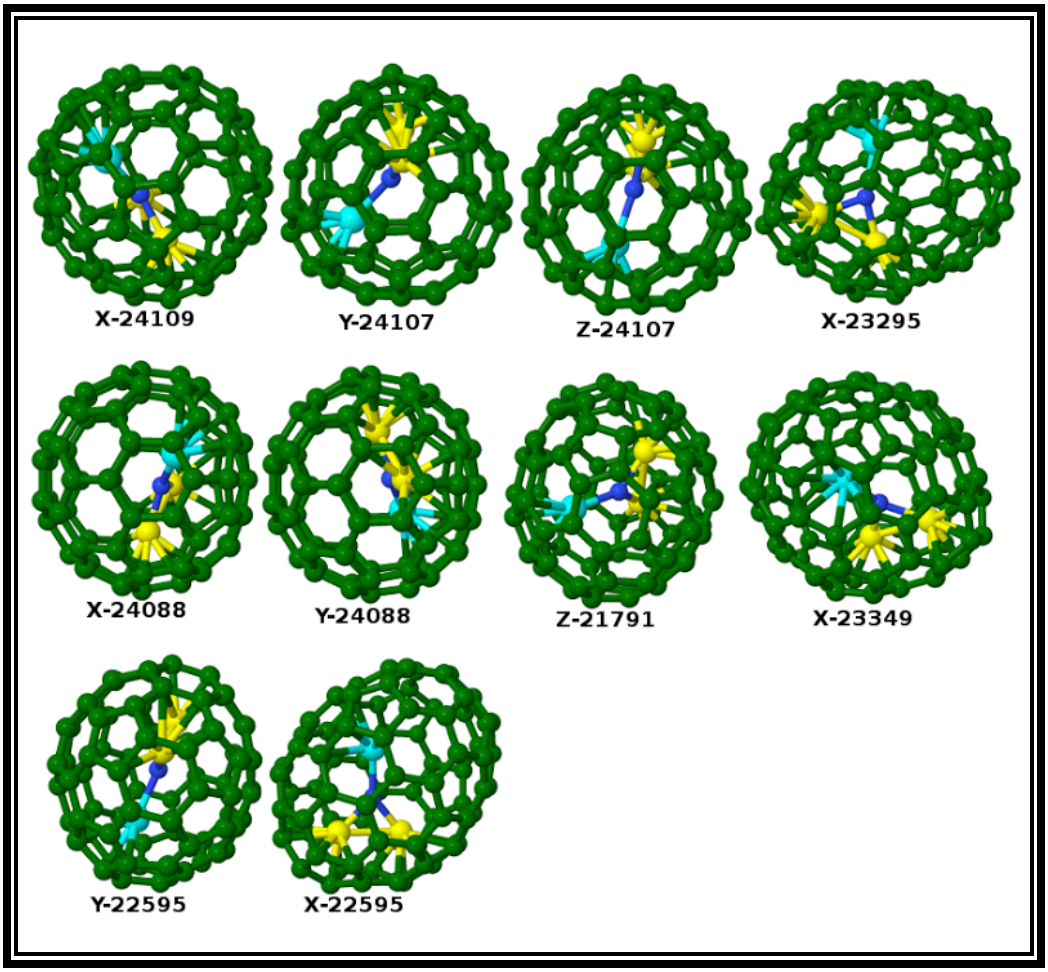

Figure 4.9: Optimized structures of $V_2ScN@C_{78}$ endohedral fullerenes. Carbon, Scandium, Vanadium and Nitrogen atoms are represented by green, aqua, yellow and blue respectively.

Table 4.5: Ten lowest energy isomers of $V_2ScN@C_{78}$ fullerenes, deviation energies were calculated with reference to the most stable structure in respective levels of theory and HOMO LUMO (H_L) gaps are also presented. All the reported energies are in eV.

$V_2ScN@C_{78}$	DFT	PM6	H_L gap	# of unpaired electrons
X22595	2.27	0.56	0.23	0
Y22595	2.01	0.71	40	0
X23349	1.90	0.63	0.33	0
Z21791	1.85	0.65	0.50	0
Y24088	1.67	0.68	0.57	0
X24088	1.67	0.68	0.57	0
X23295	1.36	0.71	0.34	0
Z24107	1.34	0.36	0.38	0
Y24107	0.93	0.36	0.50	0
X24109	0	0	0.71	2

In $V_2ScN@C_{78}$, the vanadium and some of the carbon atoms mostly contribute to the HOMO-1 and HOMO levels, where as the contribution of nitrogen decreases significantly as moving from HOMO-1 to HOMO level. Again there is higher effect due to the vanadium on the both LUMO and LUMO+1 levels. The contribution of carbon atoms decreases, where as the effect of vanadium increases from HOMO to LUMO level. Similar picture is further illustrated using density of states plots as shown in Figure 4.11, in which the HOMO and LUMO levels are

mostly contained in the carbon p and vanadium d orbitals where as the contribution of carbon decreases on the LUMO level as compared with vanadium which is similar to the orbital picture as we observed in Figure 4.10. Further more difference in density of states was mainly observed between the majority and minority spin carriers of vanadium d orbital which further illustrates to the observed magnetic moment of $V_2ScN@C_{78}$ (X-24109) fullerenes as obtained in the calculation (i.e. 2 μ_B)

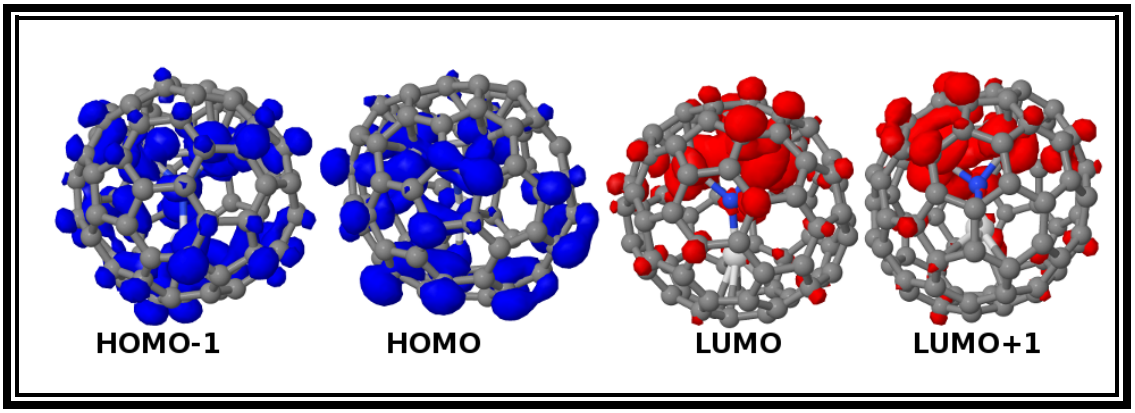

Figure 4.10: The molecular orbital plot for most probable cage $V_2ScN@C_{78}$(X-24109). HOMO-1, HOMO, LUMO and LUMO+1 from left to right.

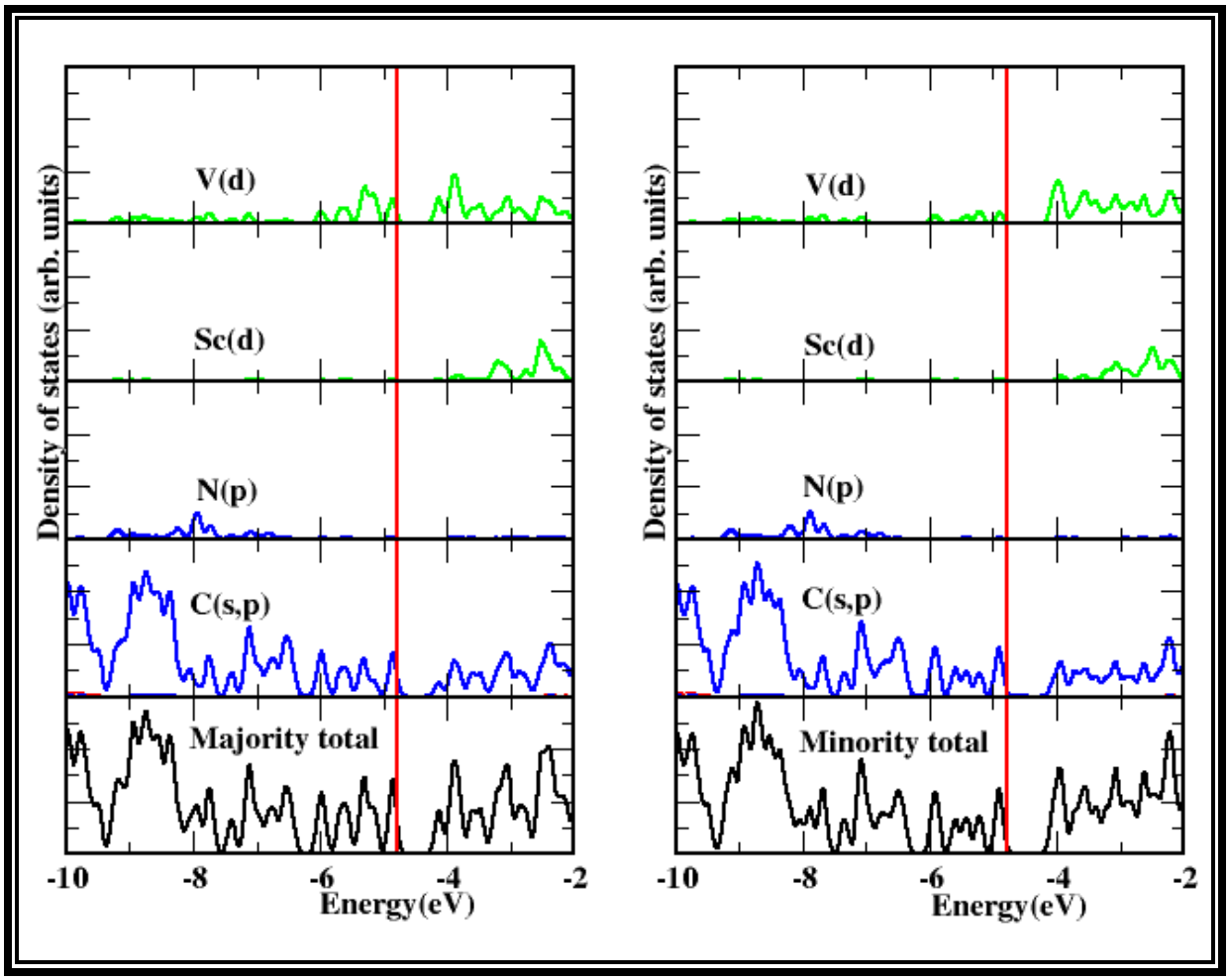

Figure 4.11: Density of states plot for the $V_2ScN@C_{78}$ (24109) blue, green and black curves indicates contribution due to p, d and majority(left)/minority(right) total respectively. The red vertical line is the Fermi level.

Chemical stability

The HOMO LUMO gap (H_L gap) is the indicative of the chemical stability. A system with larger value of H_L gap presents its higher degree of inertness on electron cloud and change in electron number. The HOMO LUMO gaps as calculated in DFT are underestimated due to the self-interaction errors present within the exchange correction functionals. However HOMO LUMO gap can also be calculated using ionization potential and electron affinity, which is known as quasi particle gap and is given by the equation

$E_g^{quasi} = vIP - vEA = E(N+1) + E(N-1) - 2E(N)$,

where E(N) is the total self consistent ground state energy of an N electron system. $vIP\ and\ vEA$ are the vertical ionization potential and vertical electron affinity, in which it is assumed that the change in electron cloud during removal and addition of electron is instantaneous so geometry does not relax to other position. The vIP , vEA, quasi particle gap and HOMO LUMO gaps for the most stable candidates of endohedral fullerenes under study are presented in the Table 4.6.

Table 4.6: Vertical electron affinity (vEA), vertical ionization potential (vIP), quasi particle gaps (Eg) and HOMO LUMO gaps for the most stable candidates of $V_2ScN@C_{2n}$ (where n=35, 38, 39, 40). All the reported energies are in eV unit.

$V_2ScN@$	vIP	vEA	Eg (quasi)	H_L gap	BE
C_{70} (X-7854)	6.04	2.81	3.23	0.44	9.67
C_{76} (X-19151)	5.87	2.87	3.00	0.12	7.74
C_{76} (X-19138)	5.87	2.78	3.09	0.31	7.97
C_{78} (X-24109)	6.23	2.68	3.55	0.71	8.02
C_{80} (Z-31924)	6.46	3.45	3.01	0.23	9.42

We have also investigated the energetic stability by computing binding energy of the lowest energy structures using given equation

$BE = -[E(V_xSc_{3-x}@C_{2n}) - E[V_xSc_{3-x}] - E[C_{2n}]$,

where 1st, 2nd and 3rd term on the right hand side of the equation are total energy of the complex, endohedral cluster and fullerene cage respectively. Higher the binding energy more is the energy released during the encapsulation of the endohedral cluster within the fullerene cages. From the tabulated values of binding energies it can be inferred that among four different size of cages V_2ScN endohedral unit better favored the C_{70} fullerene. All the reported NCFs have higher electron accepting capacity, which are even higher than that of C_{60}. From the observed values of vIP, it can be inferred that all the reported clusters are stable against oxidation as well.

Charge transfer

We have employed the program called Chargemol to perform atomic population analysis on most stable cages of each size C_{2n} (2n=70, 76, 78 and 80) along with V_2ScN endohedral unit,

which helps to determine density derived electrostatic and chemical (DDEC) net atomic charges on each atom.

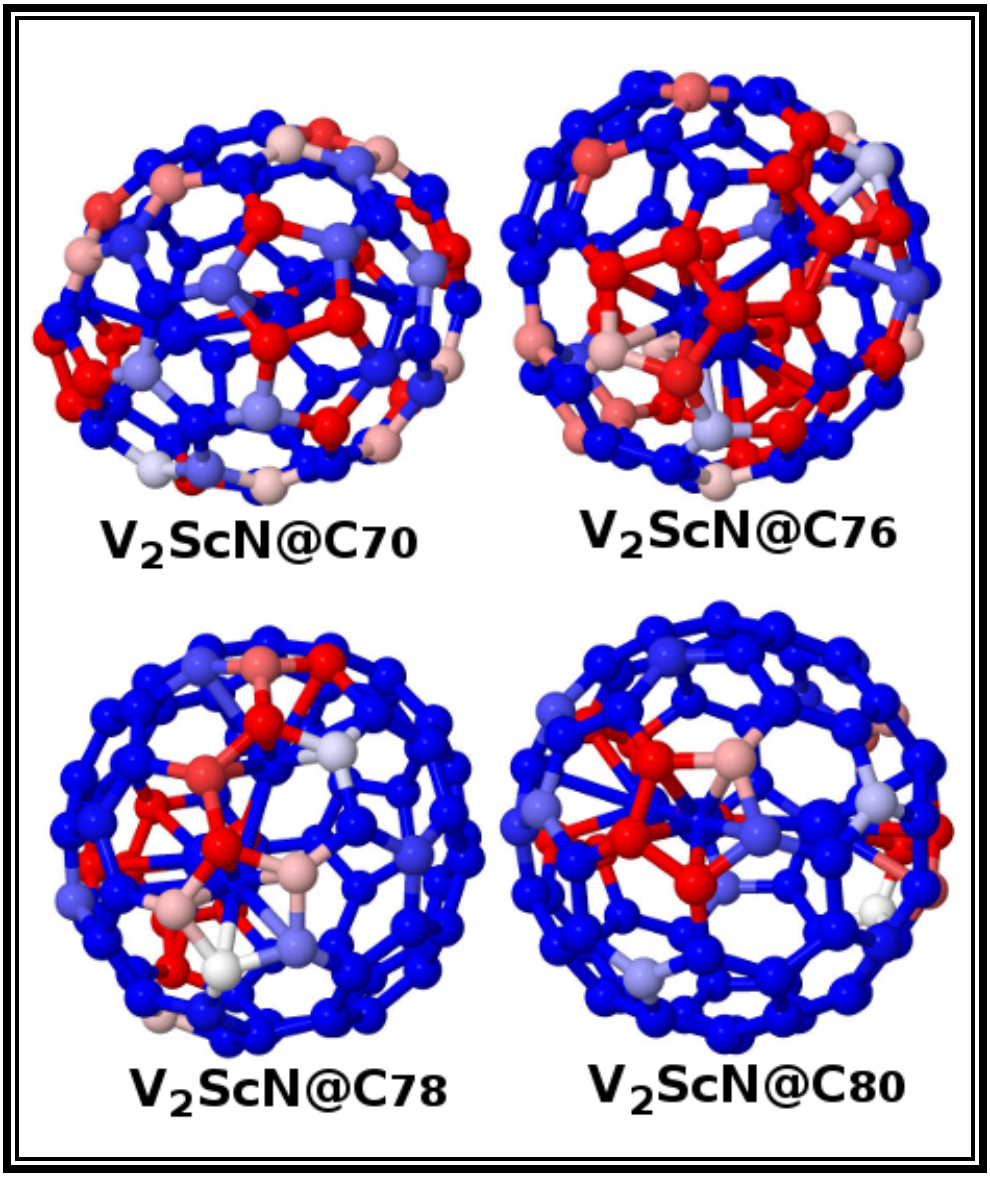

Figure 4.12: The lowest energy structures of $V_2ScN@C_{2n}$ (2n=70,76,78 and 80). Dark red, pink, white, light blue and dark blue signify the different charge carried by the atoms given by negative, less negative, neutral, less positive and positive respectively.

By summing up the charges on the endohedral unit, it was observed that the significant amount of charge transfer occurs from endohedral unit to the cage, which varies from system to system and are given by 2.33, 2.27, 2.22 and 2.39 e for the systems $V_2ScN@C_{70}$, $V_2ScN@C_{76}$, $V_2ScN@C_{78}$ and $V_2ScN@C_{80}$ respectively.

In Summary, we have screened 8149, 19151, 24109, and 31924 different isomers of C_{70}, C_{76}, C_{78}, and C_{80} fullerenes cages respectively through a series of calculation using PM6 method followed by DFT optimizations to determine the structures of endohedral fullerenes with V2ScN as endohedral unit. The host fullerene cages of the lowest energy structures of all the four types of endohedral fullerenes found in our elaborate searches have previously been reported to host different types of endohedral units. Only the $VSc_2N@C_{70}$ is found to have a non-IPR carbon cage. In all the fullerenes, the V atom is in +3 charge state. All the clusters have high ionization potential, and their electron affinities are higher than C_{60}. The charge transfer from the endohedral unit ranges from 2.22 to 2.39 electron in these clusters. These charge transfer amounts are lower as compared with singly doped vanadium. These endohedral fullerenes are stable and can be useful as an electron acceptor.

Chapter 5: The electronic structure calculation on $V_3N@C_{2n}$ (2n=70,76,78 & 80)

There are many reports of encapsulation of homogeneous metal nitride such as: Gd_3N,[155] Dy_3N,[156] Tm_3N [150] etc. along with very first member of tri-metallic nitrides family Sc_3N [157]. Wei et al. reported the encapsulation of vanadium based endohedral fullerenes for the first time, in which they were able to characterize the inhomogeneous metal nitride cluster.[50] Here, in this study we adopted the similar search method as described above for the V_2ScN based endohedral fullerenes in order to explore the possibility of encapsulation of homogeneous metal nitride V_3N with different cluster sizes such as C_{70}, C_{76}, C_{78} and C_{80}.

$V_3N@C_{80}$

There are 31924 isomers of C_{80} fullerenes and seven of them follow the IPR rule. The screening on all the possible isomers has been done in order to find the most stable cage. All the optimized isomers of C_{80} fullerenes in hex-anionic series at PM6 level of theory fitted themselves within the window of 25.09 eV and the isomer 31924 was selected as the most stable structure of $C80^{-6}$ fullerene series. The encapsulation of endohedral units V_3N along three different orientations were done on 300 lowest energy isomers within the window of 4.51 eV resulting from hex-anionic series. The resulting 900 isomers of $V_3N@C_{80}$ endohedral fullerenes were again optimized at same level of theory in neutral charge state, which resulted in an energy ordering of the isomers within 6.63 eV. The twenty lowest energy structures of $V_3N@C_{80}$ lying within an energy range of 0.69 eV from the previous step were chosen for further calculation and optimized at DFT level and ten of them are shown in the Fig 5.1. Since the twenty lowest energy structures $V_3N@C_{80}$ in the previous step does not include the most renowned icosahedral cage 31924, we have also included this cage in our study at DFT level.

Table 5.1 The ten lowest energy isomers of $V_3N@C_{80}$ fullerenes, deviation energies were calculated with reference to the most stable structure in respective levels of theory and HOMO LUMO (H_L) gaps are also presented. All the reported energies are in eV.

$V_3N@C_{80}$	DFT	PM6	H_L gap	# of unpaired electron
X31921	3.32	0	0.27	2
X31243	3.53	0.30	0.22	0
X31919	2.91	0.35	0.10	2
Z31919	3.41	0.15	0.32	0
Z28863	3.15	0.37	0.35	2
X28316	1.94	0.52	0.28	4
Y31367	2.85	0.68	0.13	2
X31367	2.85	0.68	0.15	2
Z31918	2.42	0.27	0.29	0
X31924	0.00	1.29	0.36	2

Even within the same parent cage icosahedral 31924, many structural changes such as: orientation of metal ion, bond lengths in endohedral cluster, distances of M^{ion}-C etc. were observed moving from inhomogeneous endohedral cluster V_2ScN to the homogeneous V_3N unit, which suggests the change in cluster-cage interaction with larger number of vanadium. From this series of calculations, isomer 31924 was selected as the most probable isomer of $V_3N@C_{80}$ endohedral fullerenes in which V_3N unit is distorted from the planar structure and the sum of the angles around center nitrogen is given by 347.5 degree. The V-N bond distances are given by V(i/ii)-N 1.90 Å and V(iii)-N 1.94 Å in which V(i) and V(ii) are pointed towards the hexagon

and V(iii) to the pentagon. The distance between the vanadium and the closest carbon atom is the lowest (2.12 Å) for the one, which is pointed towards the pentagon, while this distance increases to 2.17 Å for the other vanadiums.

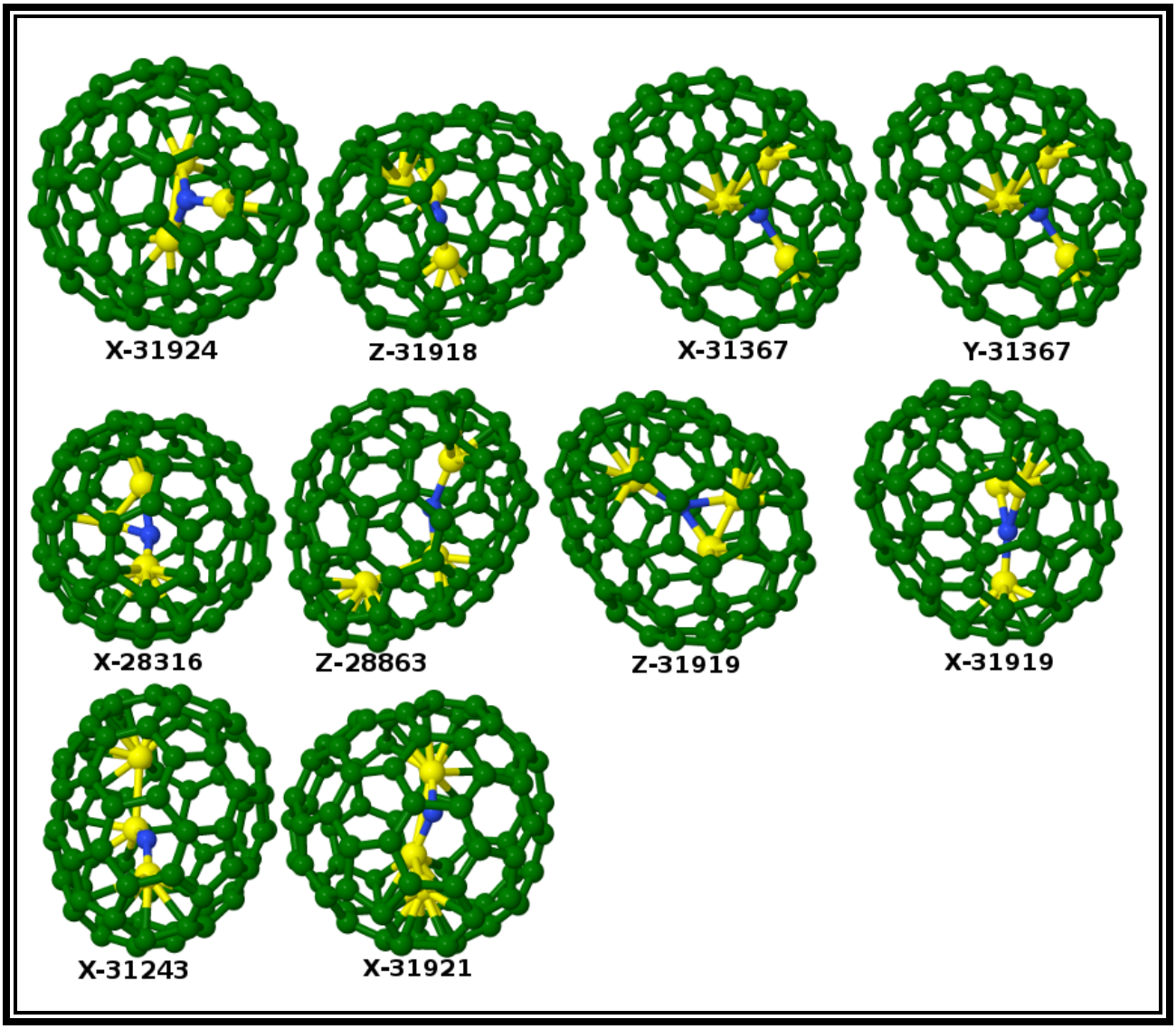

Figure 5.1: Optimized structures of $V_3N@C_{80}$ endohedral fullerenes. Carbon, Scandium, Vanadium and Nitrogen atoms are represented by green, aqua, yellow and blue respectively.

In $V_3N@C_{80}$, HOMO-1 level is mostly contained on V (i) and V (ii) vanadium, and two carbon atoms at a distance of 2.97 Å from each of those vanadium. The contribution of V(iii) increases significantly as moving from HOMO-1 to HOMO level. Again all three vanadium have prominent effect on LUMO level, where as the contribution of V(iii) increases as moving to the LUMO+1 level.

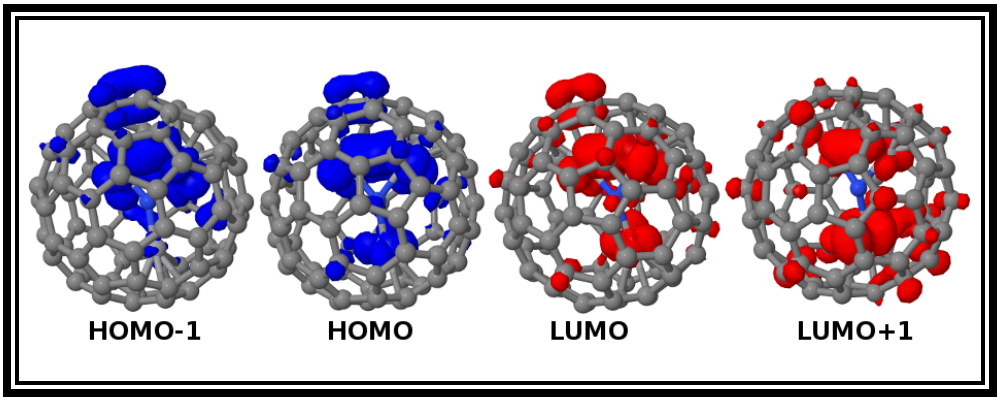

Figure 5.2: The molecular orbital plot for most probable cage of $V_3N@C_{80}$(X-31924). HOMO-1, HOMO, LUMO and LUMO+1 from left to right.

The molecular orbital picture is further assisted by the density of states plot Fig-5.2. The HOMO and LUMO levels mostly originate from the vanadium d-orbitals and some of the contribution comes from carbon p-orbitals as well. The difference in majority and minority spin carriers arise from the partially filled vanadium d-shell, which is mainly responsible for the magnetic moment of 2 μ_B obtained in the calculation.

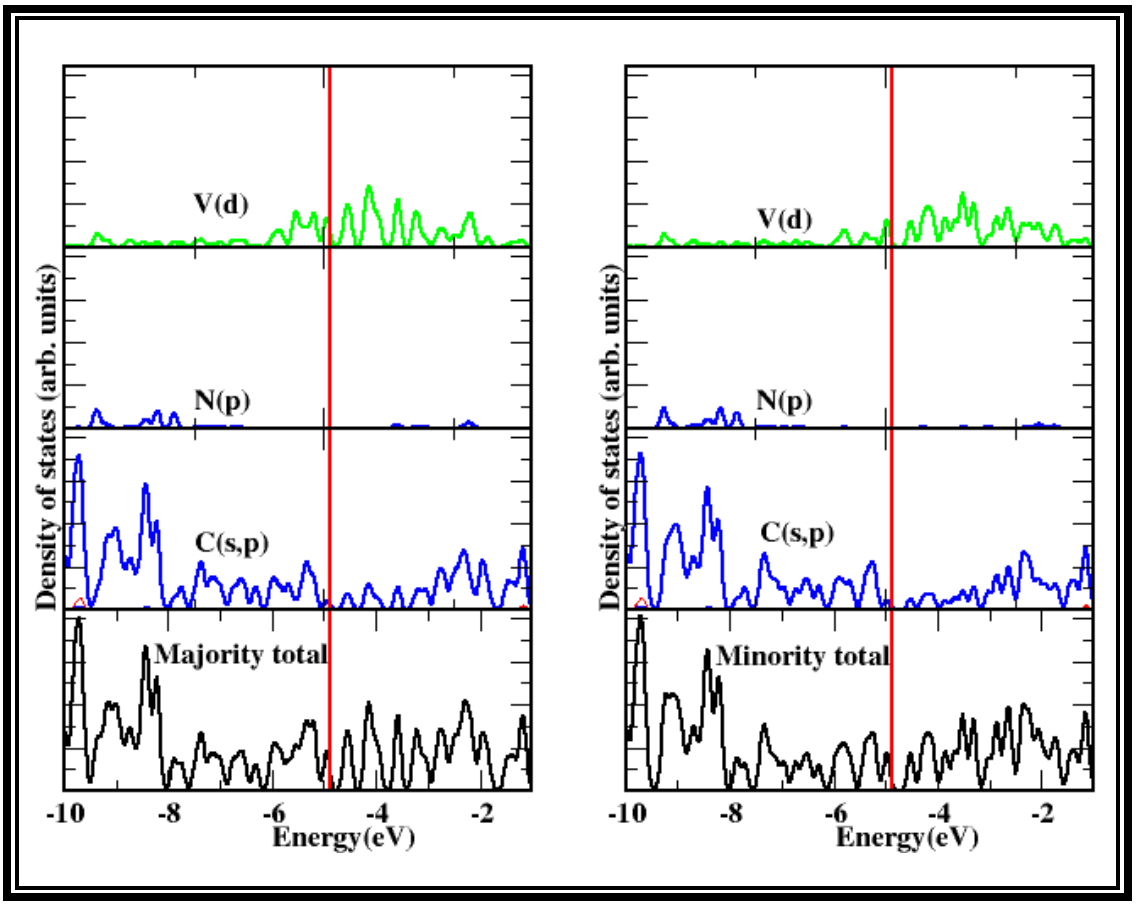

Figure 5.3: Density of states plot for the $V_3N@C_{80}$ (31924) blue, green and black curves indicates contribution due to p, d and majority(left)/minority(right) total respectively. The red vertical line is the Fermi level.

$V_3N@C_{70}$

A similar search method as done for C_{80} is also adopted here in case of C_{70} cage, in which 300 lowest energy cages from hex-anionic series within the window of 2.43eV were selected as the parent cage for endohedral fullerenes $V_3N@C_{70}$. After impregnating the endohedral unit along three different directions, the resulting 900 isomers of endohedral fullerenes optimized at PM6 level manage themselves within the energy range of 6.68 eV. The 50 lowest energy

structures of $V_3N@C_{70}$ from previous step within the energy window of 0.94 eV were selected for further calculation and optimized at DFT level using VASP and NRLMOL.

Among 900 competing structures of $V_3N@C_{70}$ endohedral fullerenes, isomer Z-8005 was found to be the most probable isomer at PM6 level of theory, but at the DFT level, the most stable candidate came out to be the isomer Z-8149, which is 0.91eV lower in energy as compared with Z-8005. Among the 8149 different possible structures of C_{70} cage, isomer 8149 is the only one, which obey the IPR rule in which none of the pentagons touch each other leading to the higher stability due to lower steric strain in the cage as compared with the cages with fused pentagons. The V_3N unit takes the perfect planar structure inside 8149 with the sum of angles M-N-M =360 degree and the V-N distances are given by V(i)-N(1.89 Å), V(ii)-N(1.91 Å) and V(iii)-N(2.01 Å). The closest carbon atoms from each metal ions are given by V(i)-C(2.10 Å), V(ii)-C(2.09 Å) and V(iii)-C(2.16 Å) in which each closest carbon vertex are shared by two hexagons and a pentagon. For simplicity, each vanadium is distinguished from each other with reference to the distance from nitrogen, where i, ii and iii are given in the order of increasing distance.

The HOMO LUMO gap ranges from 0.24 to 0.37 eV for the ten lowest isomers of $V_3N@C_{70}$ endohedral fullerenes. This gap is only 0.26 eV in the lowest energy isomer Z-8149. The observed H_L gap decreases by 0.15eV as moving from $V_2ScN@C_{70}$ (7854) to $V_3N@C_{70}$ (8149). Among ten lowest energy structures of $V_3N@C_{70}$ endohedral fullerenes, five of them carried the magnetic moment of 2 μ_B including the lowest energy isomer Z-8149.

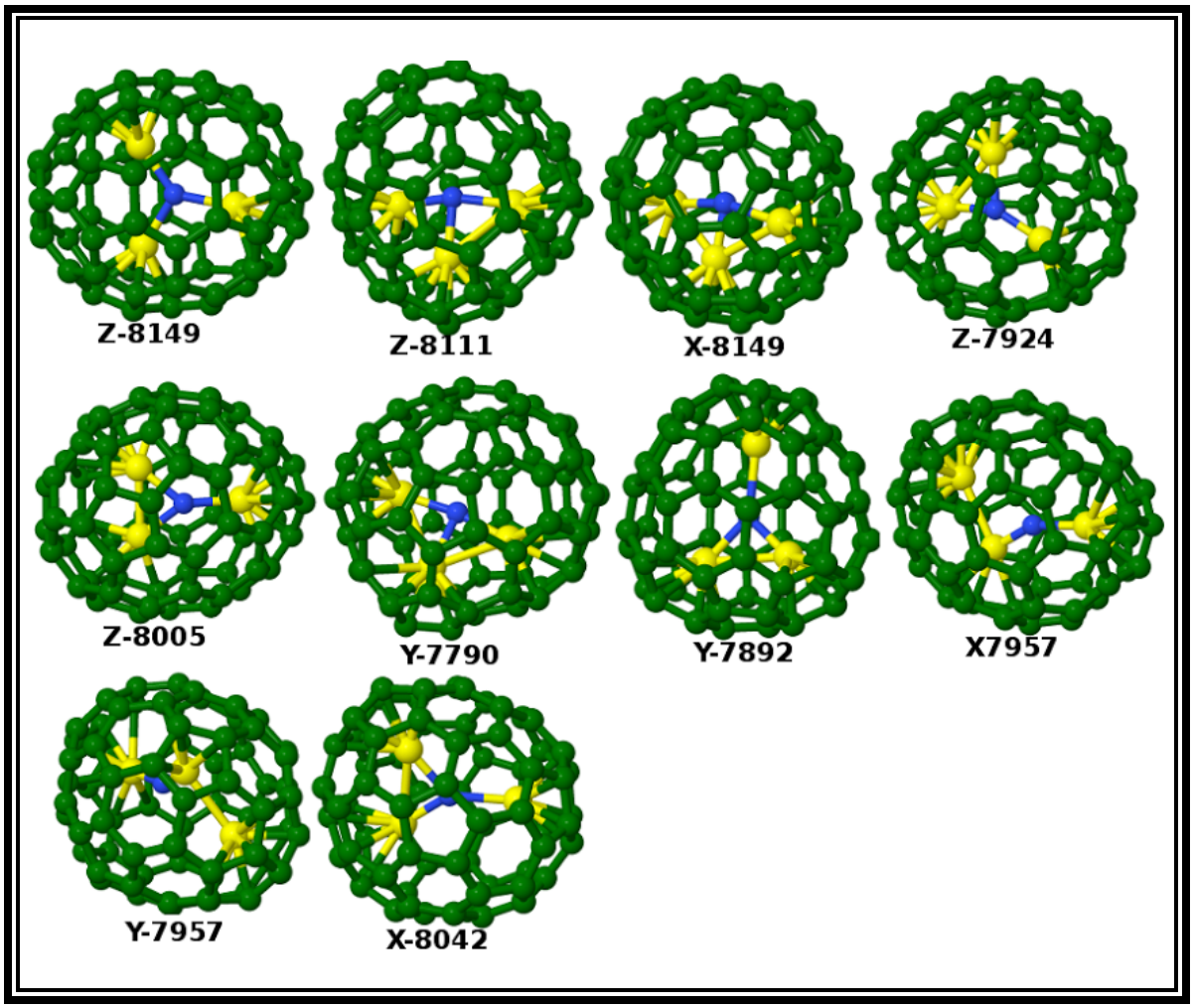

Figure 5.4: Optimized structures of $V_3N@C_{70}$ endohedral fullerenes. Carbon, Scandium, Vanadium and Nitrogen atoms are represented by green, aqua, yellow and blue respectively.

Table 5.2: Ten lowest energy isomers of $V_3N@C_{70}$ fullerenes, deviation energies were calculated with reference to the most stable structure in respective levels of theory and HOMO LUMO (H_L) gaps are also presented. All the reported energies are in eV.

$V_3N@C_{70}$	DFT	PM6	H-L gap	# of unpaired electrons
X8042	1.27	0.60	0.37	2
Y7957	1.36	0.57	0.32	0
X7957	1.36	0.58	0.30	0
Y7892	0.86	0.73	0.26	2
Y7790	0.82	0.69	0.29	2
Z8005	0.92	0	0.38	0
Z7924	0.39	0.35	0.26	2
X8149	0.45	0.73	0.24	0
X8111	0.44	0.38	0.26	0
Z8149	0	0.29	0.26	2

In $V_3N@C_{70}$, HOMO and HOMO-1 levels have contribution from all the vanadium atoms and also from some of the carbon atoms. But the contribution is significantly lower from V(iii) as compared to the V(i) and V(ii). Again moving on to the LUMO and LUMO+1 levels, there is prominent effect of all vanadium and few carbon atoms but here all the vanadium atoms have comparable contribution.

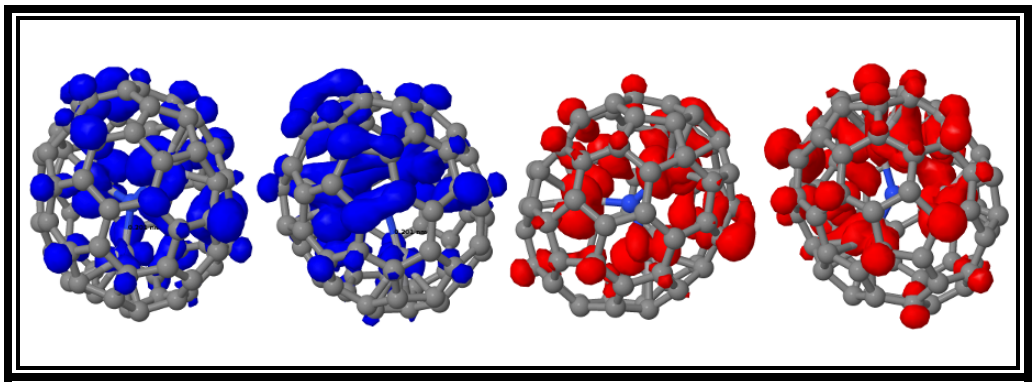

Figure 5.5: The molecular orbital plot for most probable cage of $V_3N@C_{70}$ (Z-8149). HOMO-1, HOMO, LUMO and LUMO+1 from left to right.

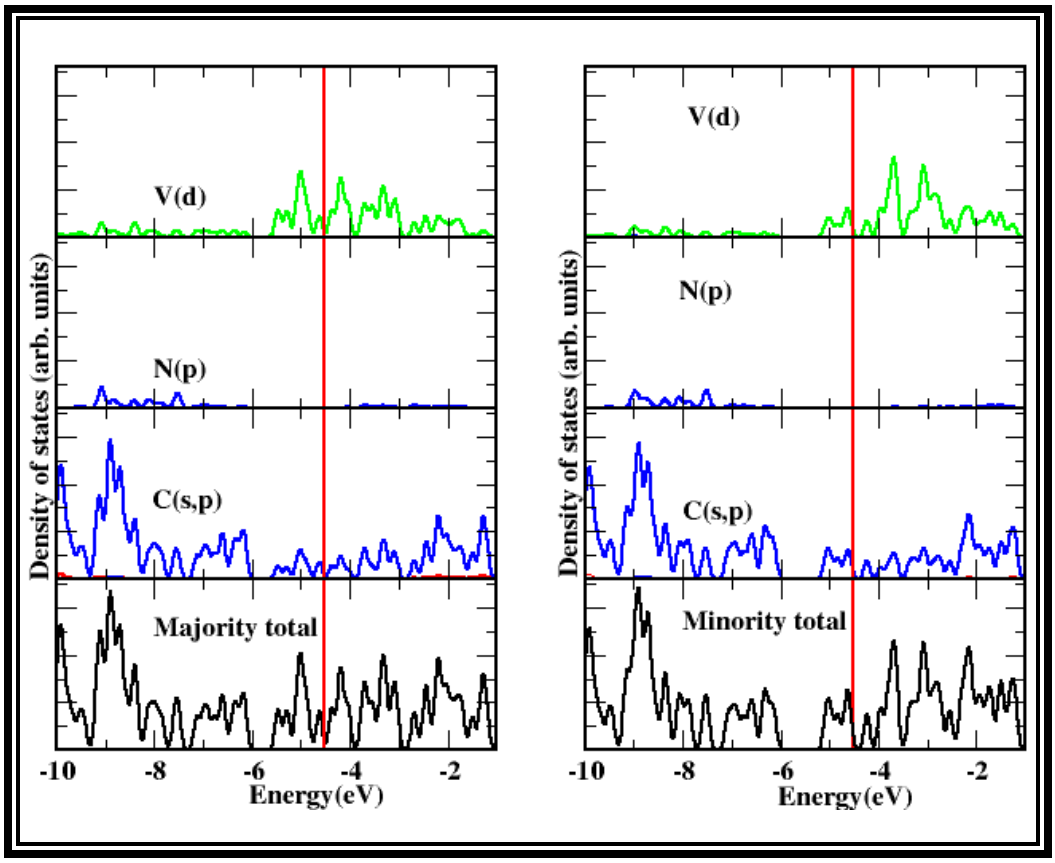

Figure 5.6: Density of states plot for the $V_3N@C_{70}$ (8149) blue, green and black curves indicates contribution due to p, d and majority(left)/minority(right) total respectively. The red vertical line is the Fermi level.

The density of states also plotted as shown in fig-5.6, which helps to illustrate the molecular orbital picture as described above, in which HOMO and LUMO levels are mostly contributed due to the vanadium d-orbitals and carbon p orbitals. The density of states difference between the majority and minority spin carriers are mostly localized in the vanadium d orbital, which is mainly responsible for the magnetic moment of 2 μ_B due to the two unpaired electrons as obtained in the calculation.

$V_3N@C_{76}$

Here in this study we tried to explore the energetic stability and electronic structure of the endohedral fullerenes $V_3N@C_{76}$, similar search method as done for previous cages was adopted with semi-empirical method followed by DFT calculations. The encapsulation of the V_3N endohedral unit along three different orientations were done on the 300 lowest energy structures of C_{76} within the window of 2.36 eV resulting from hex-anionic series. The resulting 900 isomers of $V_3N@C_{76}$ optimized at PM6 level were within energy window of 6.98 eV. The DFT calculations were done on the 50 lowest energy structures of each $V_3N@C_{76}$ metal nitride fullerenes within the window of 0.73 eV using VASP and NRLMOL codes.

Among competing structures of $V_3N@C_{76}$ endohedral fullerenes, isomer Y-19150 is the most stable isomer at PM6 level of theory but isomer X-17894 is the most stable candidate at DFT level, which is 0.34 eV lower in energy as compared with Y-19150. Gao et al. reported the lower interaction energy of YCN cluster within the same cage 17894 among the four competing isomers with a pair of pentagonal adjacency i.e. (C_1(17459)-C_{76}, C_{2v}(19138)-C_{76}, C_2(17646)-C_{76}, and C_1(17894)-C_{76}). [180] There are only two IPR-satisfying structures 19151 and 19150 among 19151 isomers of C_{76}. From our calculations, two of the inhomogeneous nitride clusters VSc_2N and V_2ScN better favored the IPR structure 19151, whereas V_3N cluster better stabilizes non-IPR 17894. The endohedral unit in X-17894 endohedral fullerene does not maintain a planar form and sum of the angles around N atom M-N-M is given by 350.6 degree. There is one pair of fused pentagons in isomer 17894 and the endohedral cluster shifted in such a way that it maintains itself closer to the region of cage where there is pentagonal adjacency. In addition, one of the vanadiums pointed towards the pentalene such that it helps to stabilize the whole complex through the Columbic attraction resulting from the positively charged vanadium ion with

negative pentalene region. The V-N bond distances are given by V(i)-N(1.81) Å, V(ii)-N(1.96) Å and V(iii)-N(1.98) Å and the closest carbon atoms from the metallic ions are at the distances of V(i)-C(2.16) Å, V(ii)-C(2.09) Å and V(iii)-C(2.11) Å, in which two of the each closest carbons is shared by two hexagons and a pentagon, while third one is on the part of pentagonal adjacency.

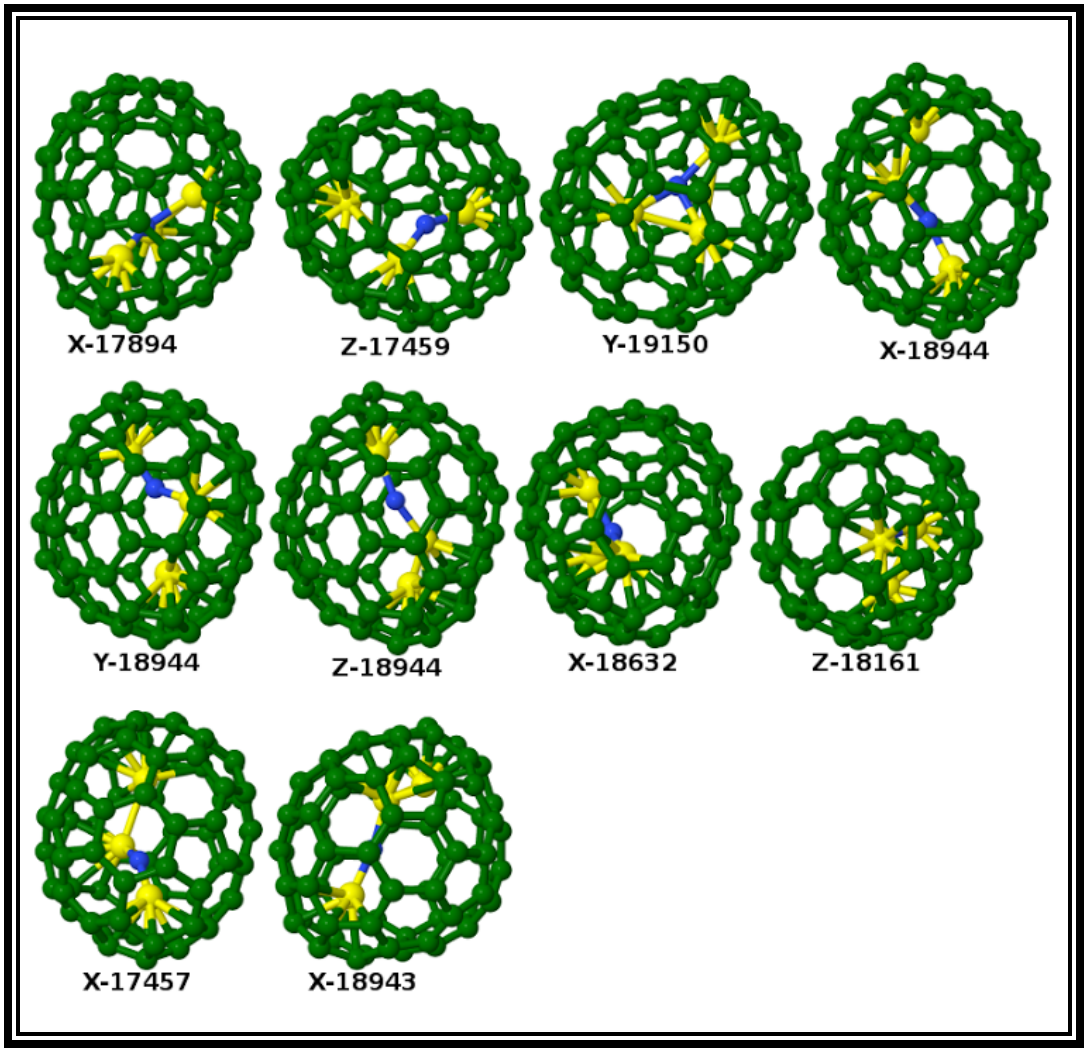

Figure 5.7: Optimized structures of $V_3N@C_{76}$ endohedral fullerenes. Carbon, Scandium, Vanadium and Nitrogen atoms are represented by green, aqua, yellow and blue respectively.

Table 5.3. Ten lowest energy isomers of $V_3N@C_{76}$ fullerenes, deviation energies were calculated with reference to the most stable structure in respective levels of theory and HOMO LUMO (H_L) gaps are also presented. All the reported energies are in eV.

$V_3N@C_{76}$	DFT	PM6	H_L gap	# of unpaired electrons
X18943	1.03	0.50	0.3	0
X17457	0.71	0.37	0.44	2
Z18161	0.68	0.61	0.43	2
X18632	0.60	0.17	0.23	2
Z18944	0.65	0.16	0.34	0
Y18944	0.65	0.35	0.24	0
X18944	0.65	0.35	0.24	0
Y19150	0.34	0	0.09	2
Z17459	0.47	0.01	0.40	2
X17894	0	0.10	0.37	4

The HOMO-LUMO gap in ten of the DFT optimized $V_3N@C_{76}$ endohedral fullerenes ranges from 0.09 to 0.44 eV, where the most stable structure X17894 has the gap of 0.37 eV. Most of the DFT optimized complexes have the magnetic moment other than zero i.e. 2 μ_B as shown in the Table 5.3, which shows the paramagnetic nature of those complexes. The most stable cage X17854 has even higher moment of 4 μ_B which may be due to the localization of higher number of electrons in the vanadium *d* orbitals.

In $V_3N@C_{76}$, the HOMO and HOMO-1 orbitals have significant d character that arises mainly from the vanadium ions. The V(i) and V(iii) vanadium atoms have higher contribution to HOMO-1 as compared with V(ii). Similarly, V(ii) and V(iii) have most prominent contribution to the HOMO as compared with V(i). The LUMO and LUMO+1 levels mostly smeared over all vanadium and few carbon atoms, where as the contribution of carbon atom increases as moving form LUMO to LUMO+1 level. Overall, the frontier orbitals have mainly d-character arising from the vanadium atoms.

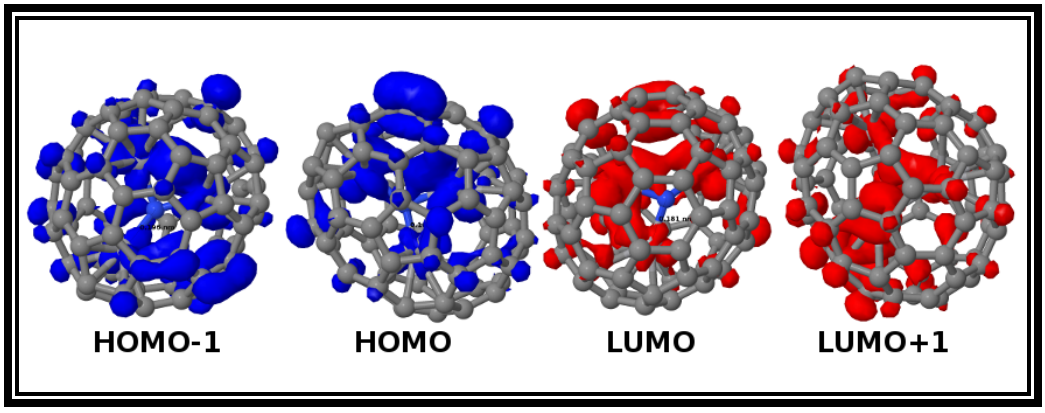

Figure 5.8: The molecular orbital plot for most probable cage of $V_3N@C_{76}$ (X-17894). HOMO-1, HOMO, LUMO and LUMO+1 from left to right.

The molecular orbital picture is further illustrated using density of state plot as shown in fig-5.8, in which clearly shows the contribution to HOMO and LUMO levels from vanadium d and carbon p orbitals. Also from the difference between density of states of majority and minority spin carriers, the unpaired electrons mostly localized in the vanadium d orbitals, which is mainly responsible for the magnetic moment of the complex (i.e. 4 μ_B).

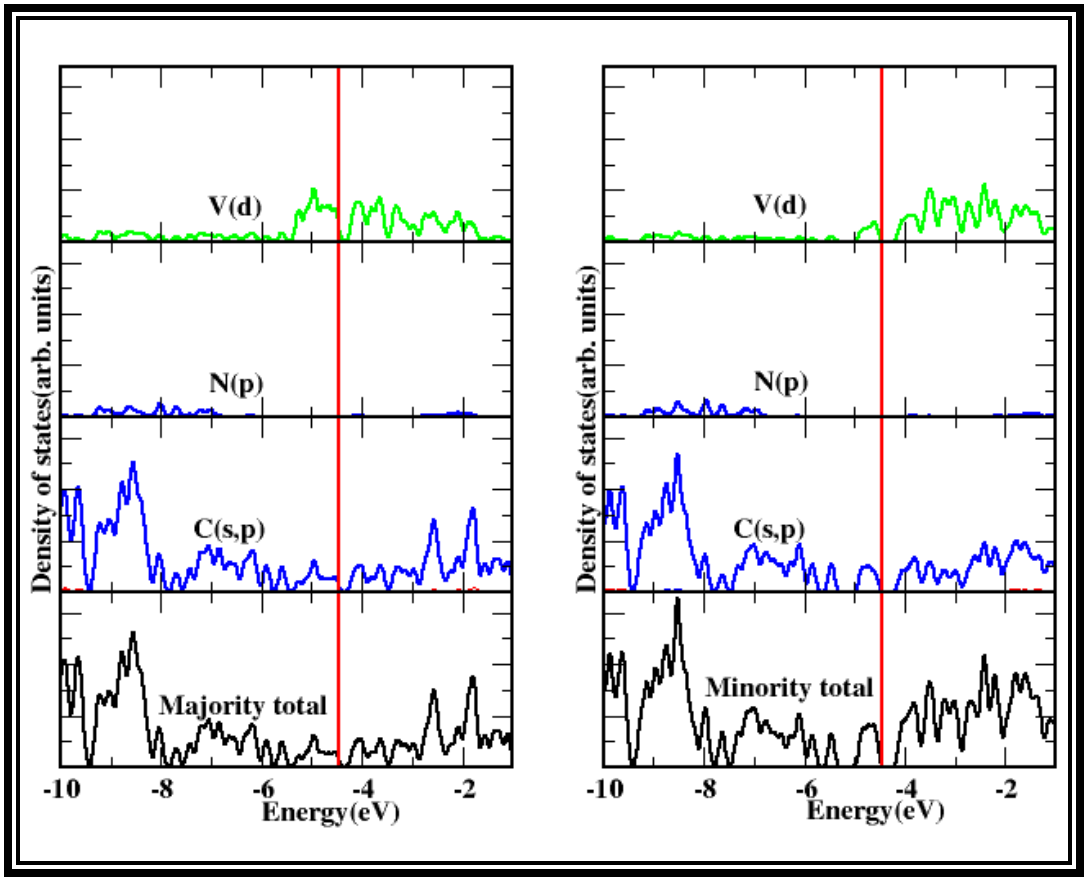

Figure 5.9: Density of states plot for the $V_3N@C_{76}$ (X-17894) blue, green and black curves indicate contribution due to p, d and majority(left)/minority(right) total respectively. The red vertical line is the Fermi level.

$V_3N@C_{78}$

C_{78} fullerenes are important in the tri-metallic nitride endohedral fullerenes family not only due to successful encapsulation of Sc_3N [176] unit but also can acts as the threshold for some of the larger clusters like Tm_3N, [177] Dy_3N [178] with significant yield. The number of isomers increases abruptly as moving to larger cage fullerenes. There is increase of 4958 isomers from C_{76} to C_{78} fullerene. Thus the search for the most stable candidate becomes more and more tedious as moving to the higher fullerenes. Again the extensive study on all the isomers of C_{78} with V_3N as endohedral unit has been done in a similar fashion as adopted in the previous cages. The encapsulation of endohedral clusters along three different orientations were done on 300 cages resulting from hex-anionic series within the energy window of 3.16eV leading to form 900 complexes which were again optimized at PM6 level of theory. The resulting isomers of $V_3N@C_{78}$ endohedral fullerenes are found within an energy range of 6.38eV. Twenty isomers of $V_3N@C_{78}$ endohedral fullerenes within the window of 0.68 eV from previous step were selected for further calculation at DFT level.

Among 900 competing structures of $V_3N@C_{78}$ endohedral fullerenes, isomer Z-24106 was selected as the most probable candidate at both PM6 and DFT levels of theory. The parent cage 24106 satisfies the IPR structure and has C_{2v} symmetry. Among five IPR-satisfying isomers of C_{78}, three of them: $C_{2v}(24106)$-C_{78}, $C_{2v}(24107)$-C_{78} and $D_3(24105)$-C_{78} were isolated in its pristine form as reported in different studies. [181] [182] [183]. In isomer Z24106, the endohedral cluster does not maintain a planar form, in which the sum of M-N-M angles around nitrogen is given by 321 degree, where as the planar structure of Sc_3N inside C78 fullerene was reported in a study. [179] The V-N bond distances are given by V(i)-N(1.88 Å), V(ii)-N(1.90 Å) and V(iii)-N(1.93 Å). The closest carbon atoms are at distance of V(i)-C(2.09 Å), V(ii)-C(2.08 Å) and

V(iii)-C(2.21 Å), in which C(2.08 Å) and C(2.09 Å) are shared by a pentagon and two hexagons, while third one is shared by all three hexagons. The HOMO-LUMO gap in the lowest ten isomers ranges from 0.16 to 0.41 eV, in which most stable structure $V_3N@C_{78}$ (Z-24106) has the gap of 0.38 eV. Campanera et al. reported the larger gap 1.24 eV in the similar homogeneous trimetallic nitride endohedral fullerene $Sc_3N@C_{78}$ at DFT level of theory.[179]

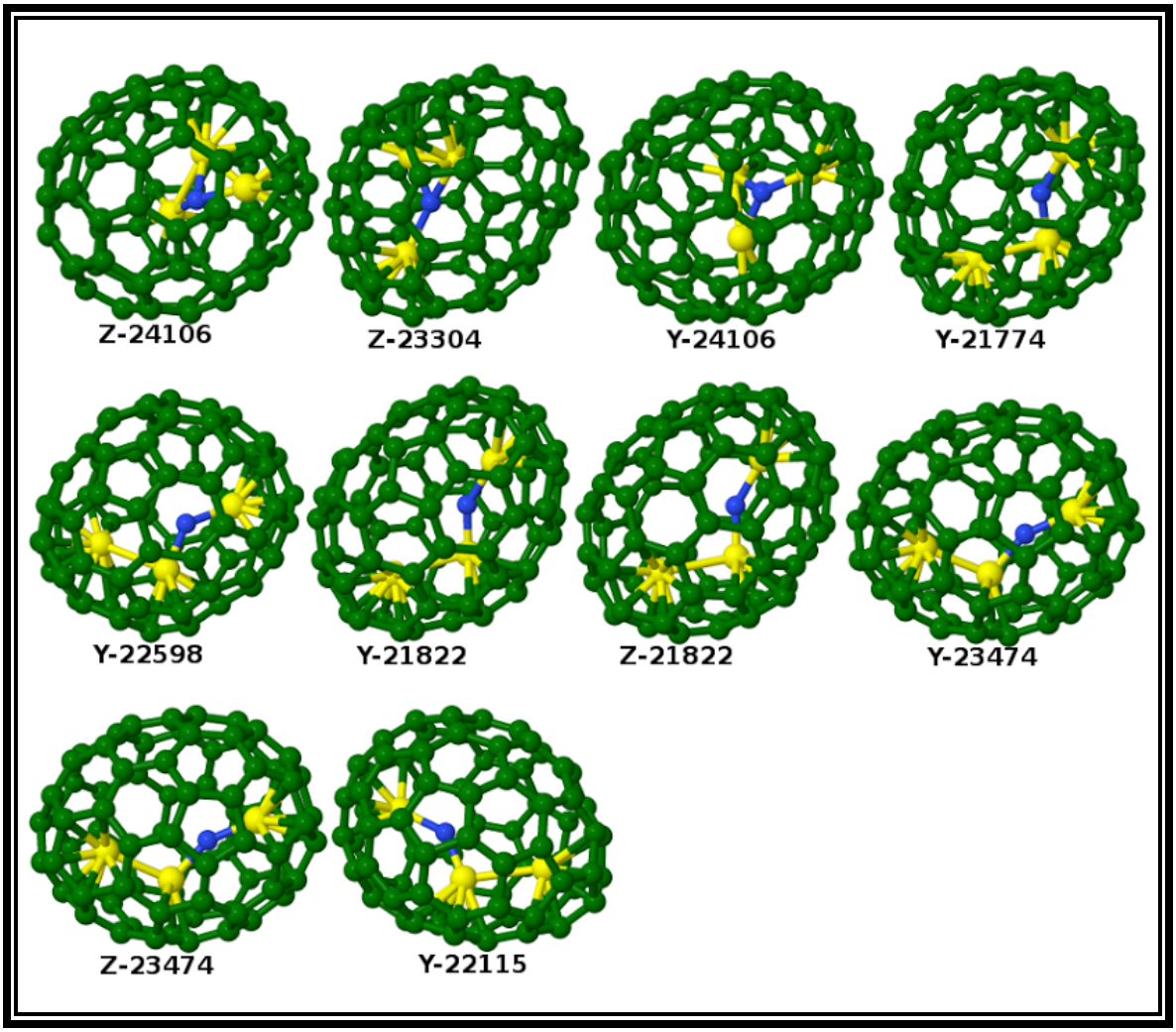

Figure 5.10: Optimized structures of $V_3N@C_{78}$ endohedral fullerenes. Carbon, Scandium, Vanadium and Nitrogen atoms are represented by green, aqua, yellow and blue respectively.

Table 5.4: Ten lowest energy isomers of $V_3N@C_{78}$ fullerenes, deviation energies were calculated with reference to the most stable structure in respective levels of theory and HOMO LUMO (H_L) gaps are also presented. All the reported energies are in eV.

$V_3N@C_{78}$	DFT	PM6	H_L gap	# of unpaired electrons
Y22115	1.71	0	0.35	2
Z23474	1.59	0.08	0.41	2
Y23474	1.59	0.08	0.41	2
Z21822	1.55	0.23	0.36	2
Y21822	1.56	0.21	0.35	2
Y22598	1.19	0.69	0.16	2
Y21774	1.07	0.61	0.34	2
Y24106	0.32	0.28	0.39	2
Z23304	1.03	0.58	0.40	0
Z24106	0	0.28	0.38	2

In $V_3N@C_{78}$, the HOMO and HOMO-1 levels are smeared over all vanadium and some of the carbon atoms but the contribution due to vanadium i.e. V(ii) is more prominent as compared with other atoms. The contribution from carbon atoms decreases as moving form HOMO-1 to HOMO level but which increases with vanadium atoms. Again the comparable contribution with that of HOMO levels has been observed in the LUMO and LUMO+1 as well, in which there is most prominent effect due to vanadium and few carbon atoms.

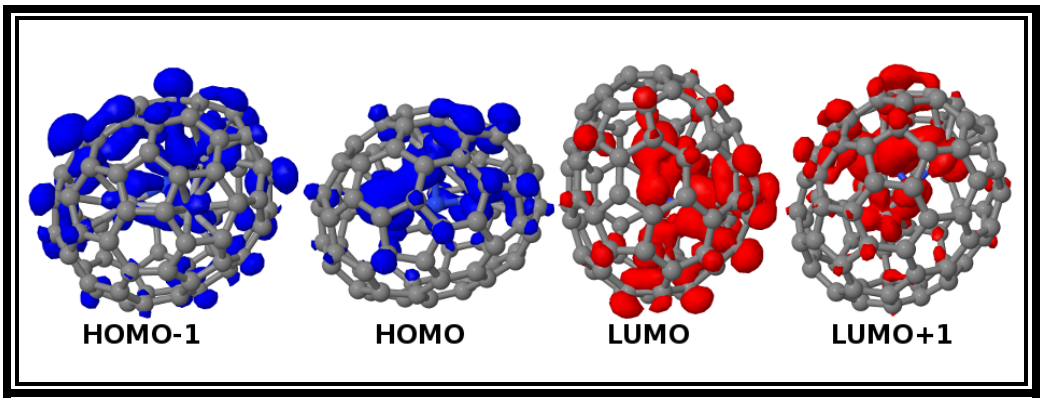

Figure 5.11: The molecular orbital plot for most probable cage $V_3N@C_{78}$ (X-24106). HOMO-1, HOMO, LUMO and LUMO+1 from left to right.

The molecular orbital picture is further illustrated using density of states plot as shown in fig 5.11, in which there is significant contribution due to the vanadium d and carbon p orbitals.

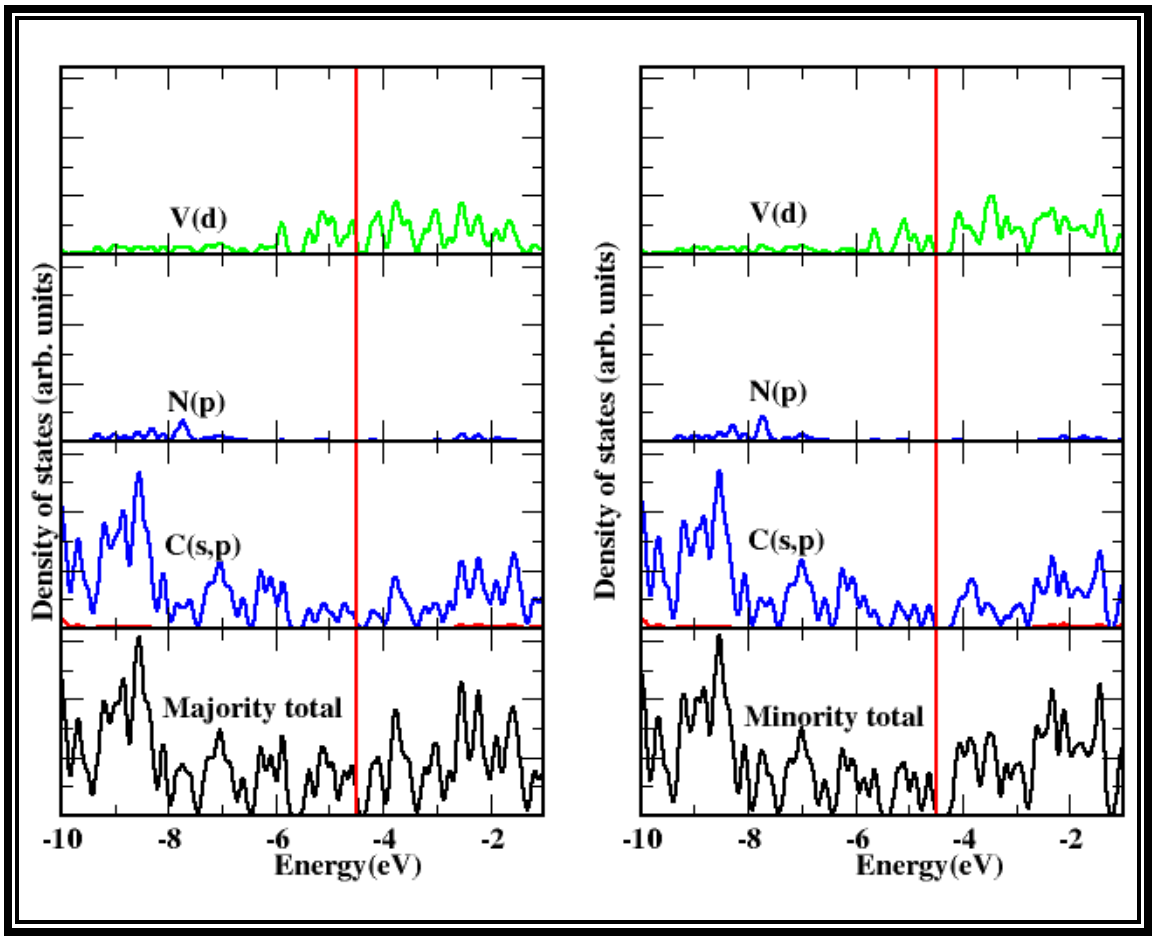

Figure 5.12: Density of states plot for the $V_3N@C_{78}$ (24106) blue, green and black curves indicates contribution due to p, d and majority(left)/minority(right) total respectively. The red vertical line is the Fermi level.

Chemical Stability

The HOMO LUMO gap (H_L gap) is the indicative of the chemical stability. A system with larger value of H_L gap presents its higher degree of inertness on electron cloud and change in electron number. The HOMO-LUMO gaps as calculated in DFT are underestimated due to the self-interaction errors present within the exchange correction functionals. However HOMO-

LUMO gap can also be calculated using ionization potential and electron affinity, which is known as quasi particle gap and as given by the equation

$E_g^{quasi} = vIP - vEA = E(N+1) + E(N-1) - 2E(N)$,

where E(N) is the total self consistent ground state energy of an N electron system. vIP and vEA are the vertical ionization potential and vertical electron affinity, in which it is assumed that the change in electron cloud during removal and addition of electron is instantaneous so geometry does not relax to other position. The vIP , vEA, quasi particle gap and HOMO LUMO gaps for the most stable candidates of endohedral fullerenes under study are presented in the Table 5.5.

Table 5.5: Vertical electron affinity (vEA), vertical ionization potential (vIP), quasi particle gaps (Eg) and HOMO-LUMO gaps for the most stable candidates of $V_3N@C_{2n}$ (where n=35, 38, 39, 40).

Systems	vIP	vEA	Eg (quasi)	H_L gap	BE
$V_3N@C_{70}$ (Z-8149)	6.05	2.88	3.17	0.26	5.03
$V_3N@C_{76}$ (X-17894)	5.95	2.69	3.26	0.37	6.13
$V_3N@C_{78}$ (Z-24106)	6.01	2.79	3.22	0.38	5.69
$V_3N@C_{80}$ (X-31924)	6.23	3.17	3.06	0.36	8.80

We have also investigated the energetic stability by computing binding energy of the lowest energy structures using given equation

$$BE = -[E(V_xSc_{3-x}@C2n) - E[V_xSc_{3-x}] - E[C2n],$$

where 1st, 2nd and 3rd term on the right hand side of the equation are total energies of the complex, endohedral cluster and fullerene cage respectively. Higher the binding energy more is the energy released during the encapsulation of the endohedral cluster within the fullerene cage. From the values of binding energies as given in the Table 5.5, it can be inferred that V_3N cluster better favored in C_{80} cage as compared with other three cages. Among four lowest energy structures of V_3N@fullerenes, only C_{76} has non-IPR cage thus it has more steric strain as compared with other IPR satisfying cages, thus having lower binding energy per atom in its (17854) parent cage. Further more all the reported cages better stabilize in its complex form rather than the separate isolated systems. All the reported NCFs have higher electron accepting capacity, which are even higher than that of C_{60}. From the observed vIP, it can be inferred that all the reported clusters are stable against oxidation as well.

Charge Transfer

We have employed the program called Chargemol to perform atomic population analysis on most stable cages of each size C_{2n} (2n=70, 76, 78 and 80) along with V_3N endohedral unit, which helps to determine density derived electrostatic and chemical (DDEC) net atomic charges on each atom.

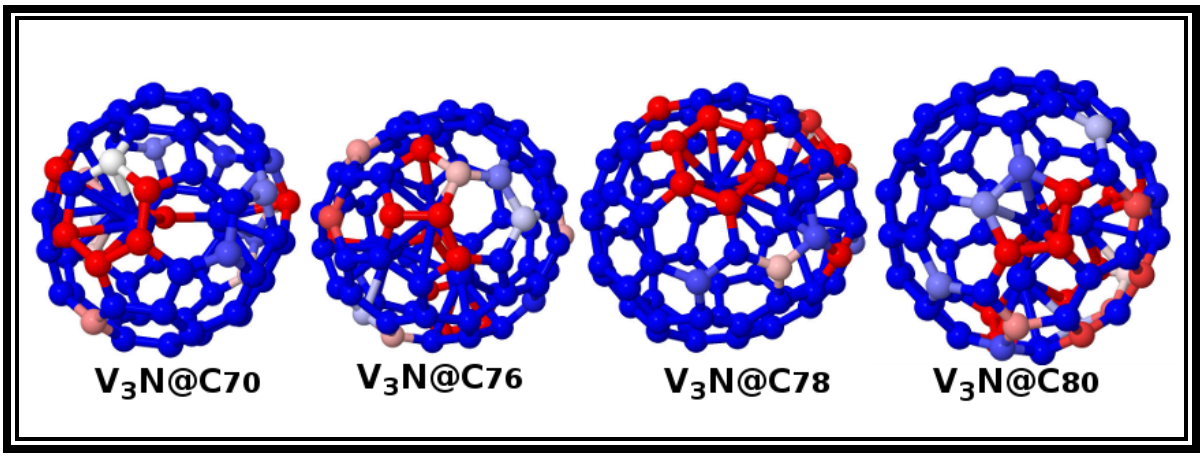

Figure 5.13: The lowest energy structures of $V_3N@C_{2n}$ (2n=70,76,78 and 80) with color represents the net atomic charges in which red, blue and white represents –ve, +ve and neutral charge respectively.

By summing up the charges on the endohedral unit, it was observed that the significant amount of charge transfer occurs from endohedral unit to the cage, which varies from system to system and are given by 2.16, 1.84, 1.76, and 1.95e for the systems $V_3N@C_{70}$ (8149), $V_3N@C_{76}$ (17854), $V_3N@C_{78}$ (24106), and $V_3N@C_{80}$ (31924) respectively. We also observed that most of the red regions contains in the regions which are close to the vanadium ions.

In Summary, we have screened 8149, 19151, 24109, and 31924 different isomers of C_{70}, C_{76}, C_{78}, and C_{80} fullerenes cages respectively through a series of calculation using PM6 method followed by DFT optimizations to determine the structures of endohedral fullerenes with V3N as endohedral unit. The host fullerene cages of the lowest energy structures of all the four types of endohedral fullerenes found in our elaborate searches have previously been reported to host different types of endohedral units. Only the $V_3N@C_{76}$ is found to have a non-IPR carbon cage. All the clusters have high ionization potential, and their electron affinities are higher than C_{60}. The charge transfer from the endohedral unit ranges from 1.76 to 2.16 electron in these clusters.

From our studies on other higher doped vanadium clusters, it can be inferred that the charge transfer decreases as increasing the number of vanadium in the endohedral cluster. These endohedral fullerenes are stable and can be useful as an electron acceptor.

Chapter 6: Electronic Structure Calculation on $C_{60}@C_{240}$ Onion

Carbon onions or carbon nano onions (CNOs) are the concentric multi shell fullerene like carbon cages. The name onion is derived from the structural resemblance of layered structure with onions. The observation of carbon onion like structure was noted even before the discovery of carbon fullerenes in 1986 [51] but they have remained in shadow of other carbon materials like graphene, fullerenes, and carbon nano tubes etc. [52] [53] [54] Iijima in 1980 provided the electron micrographs of graphitized carbon cages with diameters ranging from 30 to 70 Å [51]. The carbon nanoonions (CNO) were observed as a byproduct during the carbon black synthesis. After the discovery of C_{60} by Smalley and his group in 1985, [142] Iijima realized that the innermost shell that he observed in 1980 [51] had the diameter of 8 Å approximately similar to C_{60} and he proposed the innermost shell of CNOs could be C_{60}. Later on Ugarte put forth the formation mechanisms and observed the CNOs from the intense irradiation of carbon soot by electron beam [184]. This method is limited in terms of yield of the carbon onions but provided a route to synthesize them. There after many potential methods are reported in two decades, Du et al. reported the synthesis of CNOs with higher yield and purity using coal by radio frequency plasma [185]. In addition to Ugarte, Banhart et al. also reported the formation of CNOs by electron beam irradiation of carbon materials in 1997 in which irradiation helps to create the high temperature regime and structural fluidity which finally lead to the formation of graphitic shells [186]. The synthesis of CNOs by the chemical vapor deposition method was reported by Maquin in 1999 [187]. Other method of synthesis by high energy ball-milling was documented by Huang et al. in which it was believed that there is bending of flat sp2 hybridized bonds under mechanical deformation, which leads to the curved shell structure [188]. Gubarevich and his group documented

the CNOs synthesis by electromagnetically accelerated plasma spraying in which nano diamond particles are treated at high temperature leading to the thermal graphitization. [189] Lange et al. reported the synthesis of CNOs by arc discharge in water between pure and catalyst-doped graphite electrodes. [190] The last two synthesis methods claimed to be more attractive due to its higher yield, high purity and controllability. In 2000, Mordkovich et al. reported synthesis of double and triple layer CNOs (i.e. $C_{60}@C_{240}$, $C_{240}@C_{560}$ and $C_{80}@C_{240}@C_{560}$ etc.) from high temperature laser pyrolysis of carbon black for the first time [191].

Theoretical studies at the *ab initi*o level are scarce. In 2008, Zope reported electronic structure of $C_{60}@C_{240}$ and its first-order response to the appiled static electric field at density functional level. The nearly identical values of the polarizability of C_{240} fullerene and $C_{60}@C_{240}$ fullerene found in his study indicated that the outer shell sheilds the inner C_{60} from the applied electric field, making $C_{60}@C_{240}$ as molecular example of Faraday cage [192]. Subsequent calculations by Bhusal and co workers confirmed this behavior by expliciting computing the contributions to the polarizabilty by two shells. [193] Recently, Casello et al. studied the structure and spectroscopic properties of $C_{60}@C_{240}$ and $C_{60}@C_{180}$ using the BLYP functional with Grimme's empirical dispersion correction. [194] They noted that the encapsulation of C_{60} leads to strong mutual perturbation of the fullerenes in the $C_{60}@C_{180}$ onion. Very recently Voityuk and Sola studied the nature of the excited states calculated using the semiempirical INDO/S approach. They analyzed the nature of excited states in terms of exciton localization and charge transfer from inner to the outer cage in $C_{60}@C_{240}$. [195] The solvent effects were modeled using a COSMO-like polarization continuum model. They noted that the energy of charge separated states do not depend on the environment polarity. Here in this study we have investigated the optical and electronic structure of $C_{60}@C_{240}$ at DFT level in detail using large polarized Gaussian

basis sets with focus on the changes in the electronic properties upon complex formation and the charge transfer electronic transition from one shell to the other. Additionally we study the vibrational properties and predict the Raman spectra for the first time. Below we describe the computational methodology in brief.

Computational Methodology

All calculations are performed using density functional theory at the all-electron level using the Perdew–Burke–Ernzerhof (PBE) exchange correlation functional as implemented in the UTEP-NRLMOL code. The structures of the individual fullerene shells were first performed using the LBFGS algorithm and the onion structure was built using the optimized geometries of individual shells. The DFT-D3 parameterization was used to include the van der Waals interaction. We point out that the basis set used in NRLMOL is specially optimized for use with the PBE functional. Moreover, it correctly satisfies the $Z^{10/3}$ rule for Gaussian basis sets, where Z is the atomic number, so that the basis set superposition errors are minimized [68]. This is important as binding in these complexes occurs due to van der Waals interactions.

As discussed later in more details, a number of molecular orbitals primarily reside on one of the two-fullerene shells. As a consequence number of electronic excitations have charge transfer nature where the electron transfers from inner C_{60} unit to the outer C_{240} fullerene shell or vice-versa. The calculations of excited states with a strong charge transfer character within the density functional theory can be problematic if the time dependent density functional theory (TDDFT) with standard GGA functionals such as PBE are used. A number of alternative approaches such as constrained DFT or use of specially tuned system dependent range-corrected functionals have been suggested as a remedy to overcome charge-transfer excitation problems in

DFT. In this work, we use constrained DFT approach developed by Baruah and Pederson, which we call the perturbative delta-SCF method to compute the charge transfer excited states. In this method, the orthogonality between the ground state total wavefunction and the excited state total wavefunction, both of which are constructed as single Slater determinants from the Kohn–Sham orbitals, is strictly enforced. The occupied orbitals are relaxed in the space of unoccupied orbitals using the first order perturbation method where the perturbation Hamiltonian is the change in the ground state Hamiltonian due to rigid shift of an electron from the hole to the particle orbital. Likewise, the hole orbital is relaxed in the space of occupied orbitals. This constraint enforces the strict orthogonality between the ground and excited state wavefunctions. This method has been used earlier to efficiently describe the charge transfer excited states of several molecular donor–acceptor dyads and triads.[**196**][**191**][**68**] Our benchmark calculations on a set of small donor–acceptor molecules have shown that this method in conjunction with the pure GGA functional such as PBE can yield results of the same quality as the TDDFT method with range-separated functionals. This method is implemented in the NRLMOL code.[**69**][**197**][**198**][**199**]

Results and Discussion

The optimized geometry of the carbon was previously reported in Ref. [193] We here briefly summarize the results. The separation between the two-fullerene shells in optimized onion is 3.37 Å and show very small deviations from the fullerene shells in isolations. The vibrational frequencies calculated in harmonic approximation yielded positive frequencies indicating that the structure is a stationary point on the potential energy surface. The electronic structure of the onion is $2a_u$ $14a_g$ $28t_{2u}$ $28t_{1u}$ $30g_u$ $16t_{1g}$ $16t_{2g}$ $30g_g$ $44h_g$ $32h_u$ in agreement with

previously reported by Zope. The HOMO-LUMO gap in the onion in gas phase 0.9 eV. The isolated C60 and C240 have HOMO-LUMO gaps of 1.64 and 1.23 eV, respectively. These values are in agreement with recent report of Casella et. al. who used BLYP functional with TZVP basis set. The HOMO level in onion is at -0.1967 Hartree and the orbital is localized on the outer C_{240} shell. The threefold degenerate LUMO level is at -0.164 Hartree and the orbital is localized on the inner C_{60} shell. The isolated C_{60} has a LUMO level at -0.154 Hartree while the isolated C_{240} has HOMO level at -0.193 Hartree. Since the optimization does not show appreciable differences in the geometry of the shells, these small differences primarily result from weak mutual polarization of electron clouds. The isolated C_{60} has HOMO level at -0.214 Hartree. In onion this level is pushed down to 14th level below the HOMO and occurs at -0.221 Hatree. These eigenvalues show stabilization of energy levels upon formation of onion. However, the energy differences are very small and use of better approximations for the exchange-correlation such as recent Fermi orbital based self-interaction approaches may lead to reordering of the energy levels. The inspection of orbital molecular density plots of $C_{60}@C_{240}$, show that all molecular orbitals starting from the HOMO to HOMO-13 are mainly localized on C_{240} shell where as the HOMO-14 localized on C_{60}. Likewise, the first three LUMO levels are mainly localized on C_{60}. Next three higher LUMO levels above LUMO+2 are smeared over to both C_{60} and C_{240} with small contribution from the C_{60}. The LUMO+6 is the first molecular orbital, which is mainly contained on the C240, where as other low lying LUMOs are either on the C60 moiety or delocalized over the whole complex. The energy order and intermixing of the frontier orbitals of C_{60} and C_{240} can be seen from the density of states (DOS) plot shown in Fig. 6.2, from which it can be inferred that HOMO level is mainly contained in the C_{240} but for the LUMO level most contribution is due to C_{60} and little contribution by C_{240}.

Table 6.1: Transition spectra calculated between different HOMO(H) and LUMO(L) levels using perturbative delta self consistent field method and reported energies are in eV.

Transition	Energy spectra
H_L	1.16
H_L+1	1.15
H_L+2	1.15
H-1_L	1.14
H-5_L+3	1.74
H-14_L	1.62
H_L+6	1.50

Better estimates of energy removal energies can be obtained from the total energy differences using the approach called the delta SCF method. We have computed the electron removal energies from the total energy differences of the neutral fullerene and its cation, which typically give the first ionization energy. We compute the electron removal of the first molecular orbital that is primarily localized on inner C_{60} shell (HOMO-14) using the perturbative delta SCF method. The calculated electron removal energy of the least bound C_{60} orbital in onion is 7.29 eV. The calculated ionization energy of isolated C60 is 7.43 eV. The experimental ionization energy of C_{60} obtained using photoionization and photoelectron spectroscopy are in 7.54-7.61 eV energy range. The above values of C_{60} ionization energy show slight destabilization of C_{60} HOMO upon the onion formation, which is in disagreement with qualitative picture one gets from the Kohn-Sham eigenvalues. The ionization energy of the $C_{60}@C_{240}$, that is, the electron removal from the HOMO that is localized on outer fullerene shell is 6.25 eV. It agrees well with ionization of isolated C_{240} fullerene (6.24 eV). The inspection of isosurface plot of the LUMO

orbital which is 3 fold degenerate (Fig. 6.3) shows that it is localized on fullerene. The computation of electron affinity of C_{60} using delta SCF method gives 2.67eV. The electron affinity of $C_{60}@C_{240}$ onion is 3.45 eV which is comparable to that of isolated C_{240} fullerene (3.26 eV). Thus even though the molecular orbital plots show LUMO to be primarily localized on inner C_{60} fullerene, the addition of electron results in reordering of the energy levels. In order to understand the changes in the charge density due to the presence of an extra electron in an anion and depletion of charge density in a cation due to removal of electron, we have plotted the charge density differences of the neutral onion with its anion and cation. The Figs. 6.1, it has been observed that the extra electron in the anion is mainly localized inside the C_{240} cage and that the depletion of the charge density mainly occurs outside of the C_{240} cage. Thus it appears that the electron removal primarily occurs from the outer C_{240} shell while the extra electron localizes within the two-fullerene shells. anion and similarly for the cation too, we have carried out a atom-based site specific analysis of the charge density distribution. In this method, total volume of the complex is divided into a number of non-overlapping volumes containing the nucleus from each atom. The space closer to the nucleus of an atom compared with others is assigned to that specific atom and termed as Voronoi cell. When summed over the atoms of a fragment it provides the total charge associated with that fragment. It was found from the calculations on cation/anion of the whole complex that the charge corresponding to C_{60} and C_{240} fragments are 360.05/360.39 and 1438.95/1440.61 respectively. From this analysis it can be concluded that the removal of an electron takes place from the C240 moiety during ionization of the onion complex. This is also borne out by the fact that the IP of the complex is very similar to that of the C_{240} fragment. On the other hand, the extra electron in the anion is actually smeared over in the inside region between the C_{240} and C_{60} as seen from the density difference plot with substantial charge

both of the C_{240} and C_{60} fragments. The electron affinity of the onion is larger than both of the C_{240} and C_{60}. This result shows that even though the LUMO is located on the C_{60}, the electron affinity is not determined by the C_{60} component.

Table 6.2: The HOMO LUMO gap (H_L gap), vertical ionization potential(vIP), vertical electron affinity (vEA) and quasi particle gap of the isolated components and whole complex are presented and all reported energy are presented in eV. (Calc. =Calcualted)

Systems	**H-L gap**	**IP**		**EA**		**QP gap**
	Calc.	Calc.	Expt.	Calc.	Expt.	Calc.
C_{60}	1.64	7.38	7.6 [197]	2.67	2.69 [198]	4.71
C_{240}	1.23	6.24		3.26		2.98
$C_{60}@C_{240}$	0.90	6.25		3.42		2.83

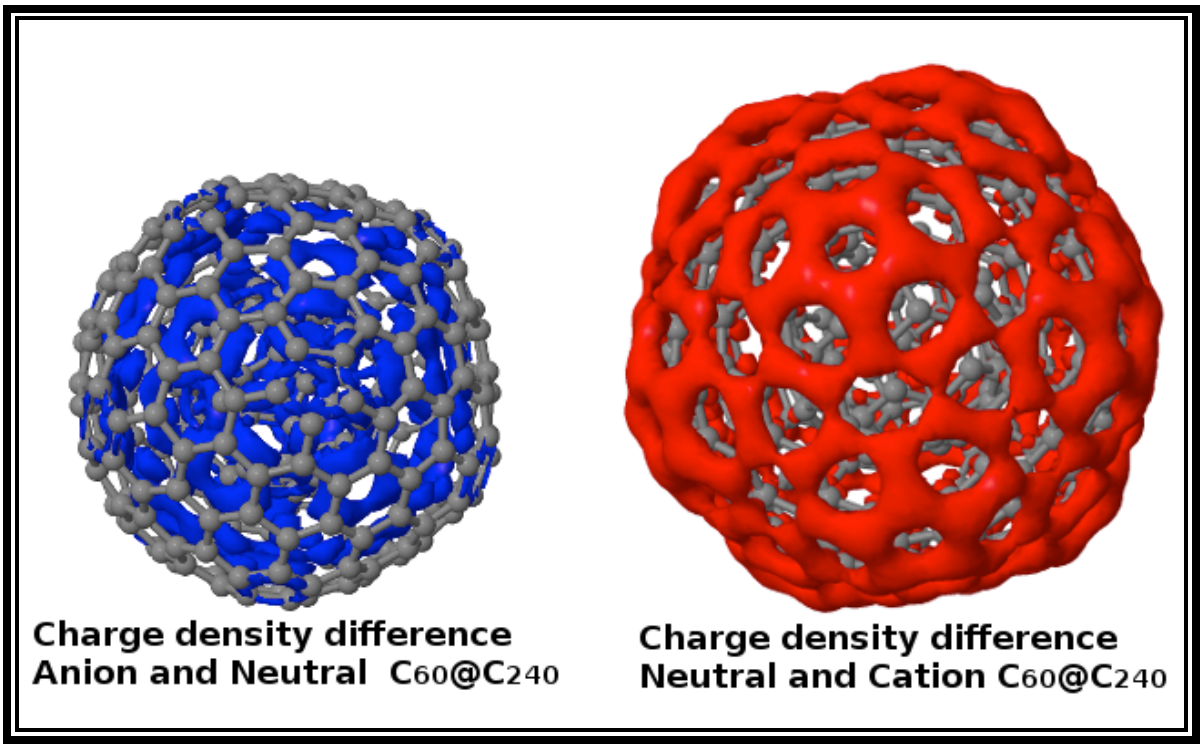

Figure 6.1: Charge density difference in $C_{60}@C_{240}$ onion.

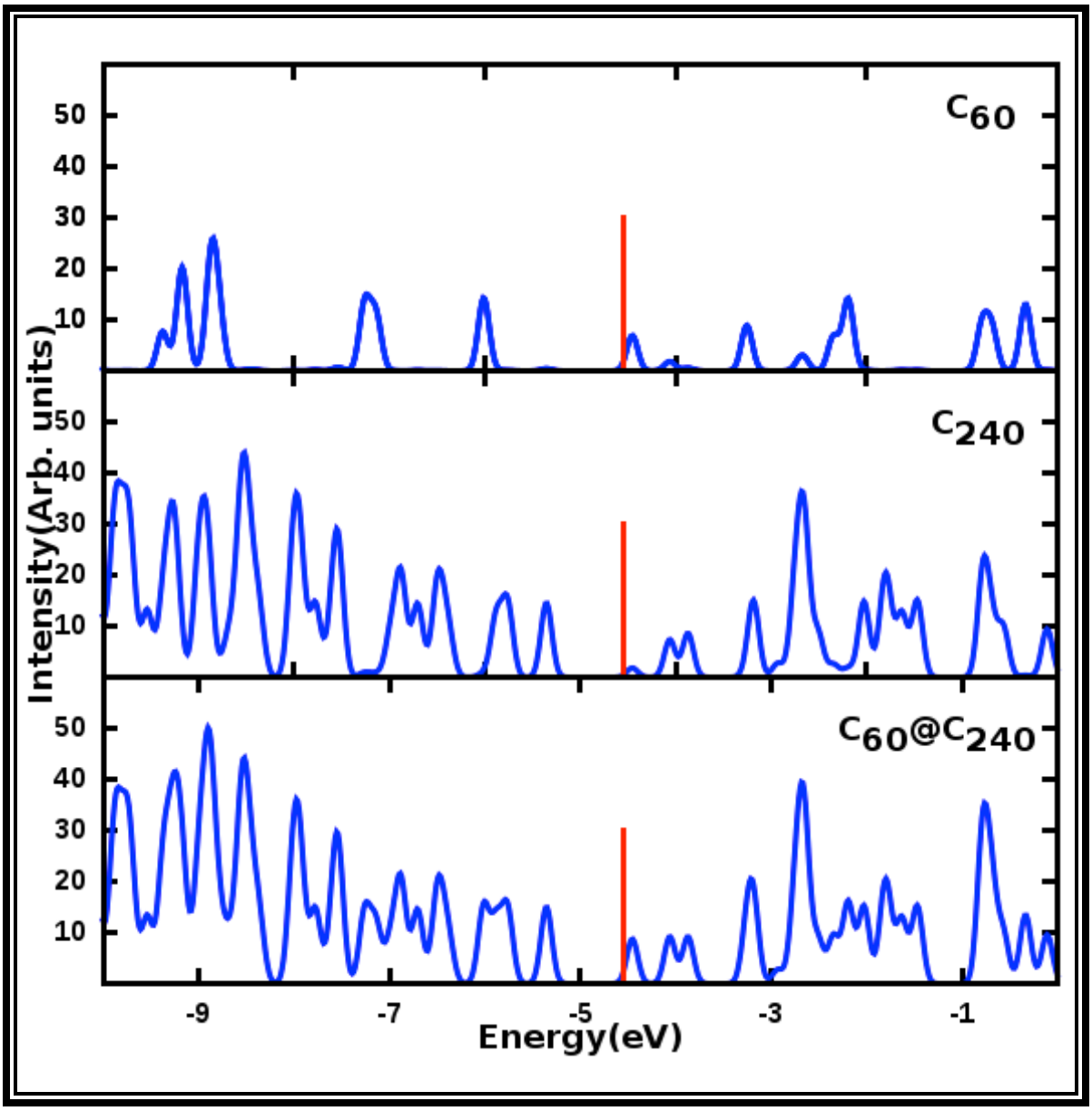

Figure 6.2: Density of states plot for the $C_{60}@C_{240}$ complex. Red line represents the Fermi level. Top and middle graphs represent the contribution of C_{60} and C_{240} components respectively to the total density of states on the bottom graph.

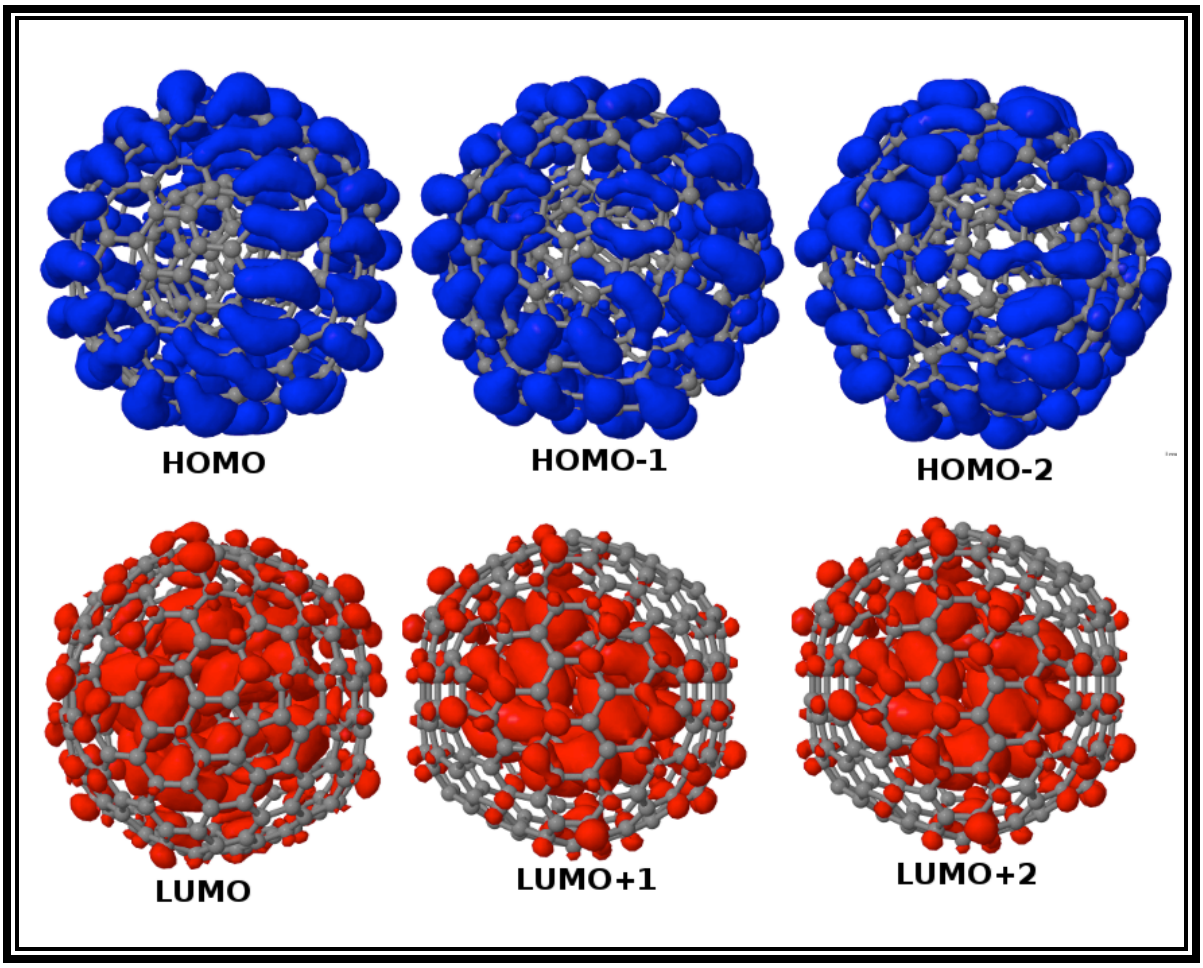

Figure 6.3: The shallow HOMO LUMO plots for the $C_{60}@C_{240}$ carbon onion.

To summarize, the electronic structure of $C_{60}@C_{240}$ is explored using density functional theory at all electron level, in which density of states, molecular orbital and charge density difference of cation and anion with neutral complex were plotted. From analysis, it can be inferred that during removal of an electron in $C_{60}@C_{240}$ onion, it mostly occurs in C_{240} component, where as in the addition of an electron C_{60} component shows the prominent effect. The five and three fold degeneracy of HOMO and LUMO levels respectively in isolated components (i.e. C_{60} and C_{240}) remains intact even in the onion complex $C_{60}@C_{240}$. The ionization

potential of the complex is very similar to that of C_{240} component, where as onion complex has higher electron affinity as compared with the isolated ones (i.e C_{60} and C_{240}).

Chapter 7: Electronic and Structural Study of Zn_xS_x [x = 12, 16, 24, 28, 36, 48, 96, and 108] Cage Structures

Introduction

II-VI compound materials are of significant interest in semiconducting industry due to their potential technological applications such as photovoltaic solar cells, quantum devices, optical sensitizers, sensors, photo-catalysts, etc.[1] [200] Amongst the II-VI compounds, ZnS are perhaps one of the most studied systems because of their unique electronic and optical properties. Over the last couple of decades, a large variety of ZnS nanostructures have been synthesized from zero-dimensional nanoparticles to nanoribbons, nanowires, nanorods, nanotubes, nanosheets etc.[2-8] [201] [202] [203] [204] [205] [206] [207] The most stable structure of bulk ZnS at room temperature is known as sphalerite (zinc blende or cubic phase), and above 1000 degree Celsius the less dense hexagonal form wurtzite structure is also stable. Both sphalerite and wurtzite are intrinsic, wide-bandgap semiconductors that adopt structures related to many other semiconductors, such as gallium arsenide. The cubic form of ZnS has a band gap of about 3.54 eV at 300 kelvin, but the hexagonal form has a band gap of about 3.91 eV[9] [208] and ZnS can be doped as either an *n*-type semiconductor or a *p*-type semiconductor.

Hollow nanoparticles are interesting from the possible range of their applications. The internal cavity of these particles offer opportunities to host other elements or small clusters. Such possibilities have been explored for their applications in catalysis, delivery of drugs, development of artificial cells, and protection of biologically active agents such as proteins, enzymes, or DNAs. Experimentally, various methods such as coaxial nozzle techniques,[10] [209] microemulsion, reverse microemulsion,[11] [210] exchange-resin,[12] [211] and self-organization methods,[13] [212] have been employed to prepare hollow spheres. Hollow nanostructures of ZnS

have also been observed in experiments. Dong *et.al* reported large scale fabrication of ZnS hollow vessels, short tubes, and hollow spheres using a simple micelle method.[14] [213] They observed large blue shift in the UV–vis spectrum of hollow nanostructures pointing to their quantum confinement effect. On the other hand, Yongjun He used a novel emulsifier-free emulsion route to synthesize ZnS hollow microspheres.[15] [214] Using this technique he reported ZnS hollow microspheres made up of ZnS nanoparticles which had cubic structures (β-ZnS). The author also noted that ZnS hollow microspheres became smaller and more compact when reaction temperature is increased.[15] [214] Liu *et al*. also reported semiconductor ZnS micrometer hollow spheres obtained by a solvothermal route. In this case the ZnS spheres were formed through the aggregation of ZnS nanocrystals and showed strong photoluminescence properties.[16] [215] Further, using a one-step hydrothermal process, Panda and Chaudhari recently reported synthesis of crystalline ZnS hollow spheres. These ZnS spheres had diameters in the range 1.5 to 3.5 μm and shell thickness from 230 to 700 nm.[17] [216] Smaller hollow nanocages in the nanometer range have also been synthesized. Dong and coworkers fabricated small and monodisperse ZnS hollow nanospheres by a simple surfactant polyethylene glycol (PEG) assisted method. The outer diameters of these nanospheres ranged from 60 to 70 nm and had wall thickness of 15–20 nm.[18] [217] Furthermore, a large scale synthesis of ZnO/ZnS hollow nanocages was recently reported by Yu, X-L *et al*. through a combination of hydrothermal and etching processes. Interestingly, the authors proposed the use of the hollow cages as efficient sensors to detect ethanol with fast response and good reproducibility.[19] [218] In addition, the synthesis of ZnS nano-cages by laser ablation of Zn was documented by Wang *et al*. using ultra-rapid acid etching in order to benefit on the porous surface structure by removing the Zn from the early nucleation stage.[20] [219]

The properties of elements at the atomic scale present a non-scalable behavior where the variation is highly nonmonotonic.[21-22] [220] [221] In this size regime (for example, atomic clusters) unusual things often arise because of quantum confinement, boundary effects. The bulk ZnS occurs commonly in two phases - Zinc Blende and Wurzite. The WZ phase has a higher band gap 3.77 eV compared to the ZB phase (3.68 eV). The ZnS nanocrystals show phase transitions between ZB, WZ and rock-salt structures under pressure and temperature change.[23-27] [222] [223] [224] [225] [226] Kole et *al*. have shown that ZnS nanocrystals of size 1.1-1.5 nm can undergo transformation from cubic to hexagonal forms at a much smaller temperature of 250ºC.[28] [227] Theoretical calculations of bulk-like ZnS clusters predict a band gap ranging from 2.6 to 3.3 eV[29] [228] which is an intermediate value between the gap of cubic and hexagonal bulk phases. Moreover, structural, electronic, and optical information about small nanoparticles can be obtained using computer simulations to gain insight into the properties and potential uses of ZnS. Early calculations using density functional theory on small (ZnS)n clusters showed a growth pattern of forming planar, ring-like structures for very small nanoclusters of sizes n=2-5 but as the size increases the tendency is more towards forming spheroids or bubble clusters.[30-40] [229] [230] [231] [232] [233] [234] [235] [236] [237] [238] [239] Even though hollow ZnS nanocages with a radius below 30-35 nm have not yet been observed, theoretical calculations indicate formation of ZnS nanocages for this smaller size range. For instance, Spano and co-workers reported the spontaneous formation of ZnS bubble clusters, i.e. hollow cages, in classical molecular dynamics simulations Zn_xS_x [x = 10-47, 50, 60, 70, and 80] for which onion like or "double bubble" structures[33-34] [232] [233] like the one for $Zn_{60}S_{60}$ were predicted. These cages presented "bubble" like polyhedral structures with atoms in threefold coordination rather than a densely packed bulk-like structure. Remarkably, Spano's density functional theory calculations of the cage structures showed that the bubble

clusters are more stable than the bulk-like species. Following Spano's work, Yong *et al*. theoretically investigated the possibility of formation of low-density Zn_nS_n (n=12,16) using density functional theory[41] [240] and found large HOMO-LUMO gaps in highly symmetric structures. The authors propose these energetically favorable clusters for applications in gas storage, heterogeneous catalysis, and filtration given their nanoporous structure nature. On the other hand, a tight-binding DFT study for n = 10, 16, 37, 57 and 68 showed that the most stable structures are ring-, or band-like configurations, with large radii.[35] [234] The tight binding DFT calculations predict that bubble clusters are more stable than bulk-like clusters for n<17, whereas the larger clusters such as n=58,68 prefer bulk-like configuration.[35] [234] But same group also showed that starting with a different set of hollow and bulk-like cluster led to the result that for clusters with n = 10, 16, 37, 57, 68, 86 and 116, the hollow clusters are more stable than bulk-like clusters.[42] [241] Using molecular dynamics technique Khalkhali *et al*. have shown that free standing ZnS nanocrystals of WZ and ZB structure of size 1-5 nm can undergo structural change.[32] [231] Motivated by these observations we designed several threefold coordinated ZnS hollow Zn_xS_x [x = 12, 16, 28, 36, 48, and 108] cage nanoparticles and $Zn_{96}S_{96}$ onion with the aim to investigate their chemical and vibrational stability. Several of these cage structures have not been studied before. Using accurate density functional calculations we show that these systems are electronically, energetically, and chemically stable. More importantly, we show that these structures are also vibrationally stable (local minima on the potential energy surface) and posit that they may host endohedral elements and small clusters. The vibrational frequencies can indicate about the structural stability of the clusters. We investigate the quasiparticle gap (transport gap) and optical gap for selected nanoparticles. The quasi-particle gaps of ZnS cages studied herein show quantum-confinements effects and have not been reported earlier. We note

that the cages studied here are similar in structural aspect to those reported of boron nitride ($B_{24}N_{24}$ and $B_{36}N_{36}$).[43-44] [242] [243] Such pattern has also been observed in a recent theoretical study of a ZnS monolayer[45] [244] and in a recent observation of a nonpolar structure of 2 monolayer thick ZnO(0001) films on Ag(111) by surface x-ray diffraction and scanning tunneling microscopy.[46] [245]

Computational Method

All electron theoretical calculations were carried out within the density functional formalism and the generalized gradient approximation of Perdew, Burke and Ernzerhof (PBE96) to describe the exchange-correlation effects.[47] [246] The electronic orbitals and eigenstates were determined using a linear combination of Gaussian atomic type orbital molecular orbital (LCGTO) approach as implemented in the NRLMOL code.[48-49] [247] [248] A 6*s*, 5*p*, and 3*d* basis set for the S atom, and a 7*s*, 5*p*, and 4*d* basis set for the Zn atom was used.[50] [249] In each case, the basis set was supplemented by a diffuse *d*-type polarization function. The integrals were accurately and efficiently calculated using a variational mesh and the self-consistency cycle was carried out till the energies converged to 10^{-6} Hartree. We performed symmetry restricted geometry optimization using the LBFGS scheme till reaching convergence when the forces were smaller than 0.001 a.u. The vibrational frequencies were calculated by introducing small perturbations to the equilibrium geometry in every Cartesian direction for all the atoms and calculating the energy and forces of the distorted geometries. From these, the dynamical matrix was calculated by the finite difference method, diagonalization of which yielded the frequencies.[51] [250] Partial charges were determined using a natural bond orbital (NBO) analysis.[52] [251]

Discussion and Results

Geometries

Figure 1 and 2 presents the Zn_xS_x optimized geometries. We confirmed that the studied clusters are local minima in the potential energy landscape as attested by the vibrational analysis that showed only real frequencies for $Zn_{12}S_{12}$, $Zn_{16}S_{16}$, $Zn_{28}S_{28}$(O, S_4 and S_8 symmetry) and $Zn_{36}S_{36}$. The optimized coordinates of the inequivalent atoms are given in Table S1 in the supporting information and the vibrational modes of various cages are presented in Fig. S1 to S6. An analysis of NBO electronic charges show that the partial charges on the S range from -1.27 to -1.38 e while that for the Zn range from +1.28 to +1.34 e. Thus the charge transfer occurs from the Zn to S leading to the ionic character of the Zn-S bond. Following the observation of Spano *et al*. on three-fold coordination of Zn and S atoms in cage structures [33,34] [232] [233] in their molecular dynamics simulations, the atoms in the cage structures chosen herein have three-fold coordination.

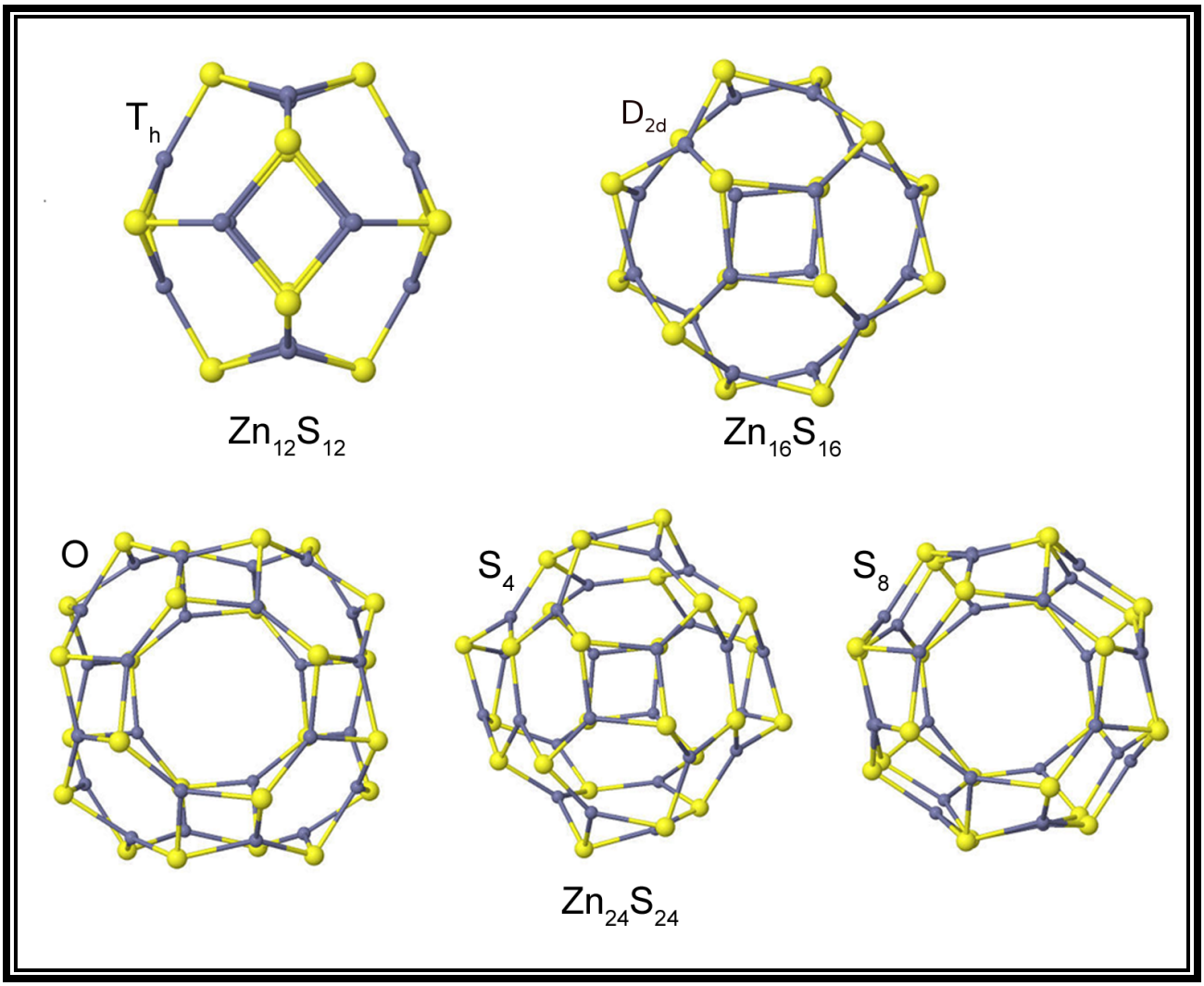

Figure 7.1: Optimized structures of $Zn_{12}S_{12}$, $Zn_{16}S_{16}$ and $Zn_{24}S_{24}$. Zn and S atoms are represented by gray and yellow circles. Molecular symmetry is also given.

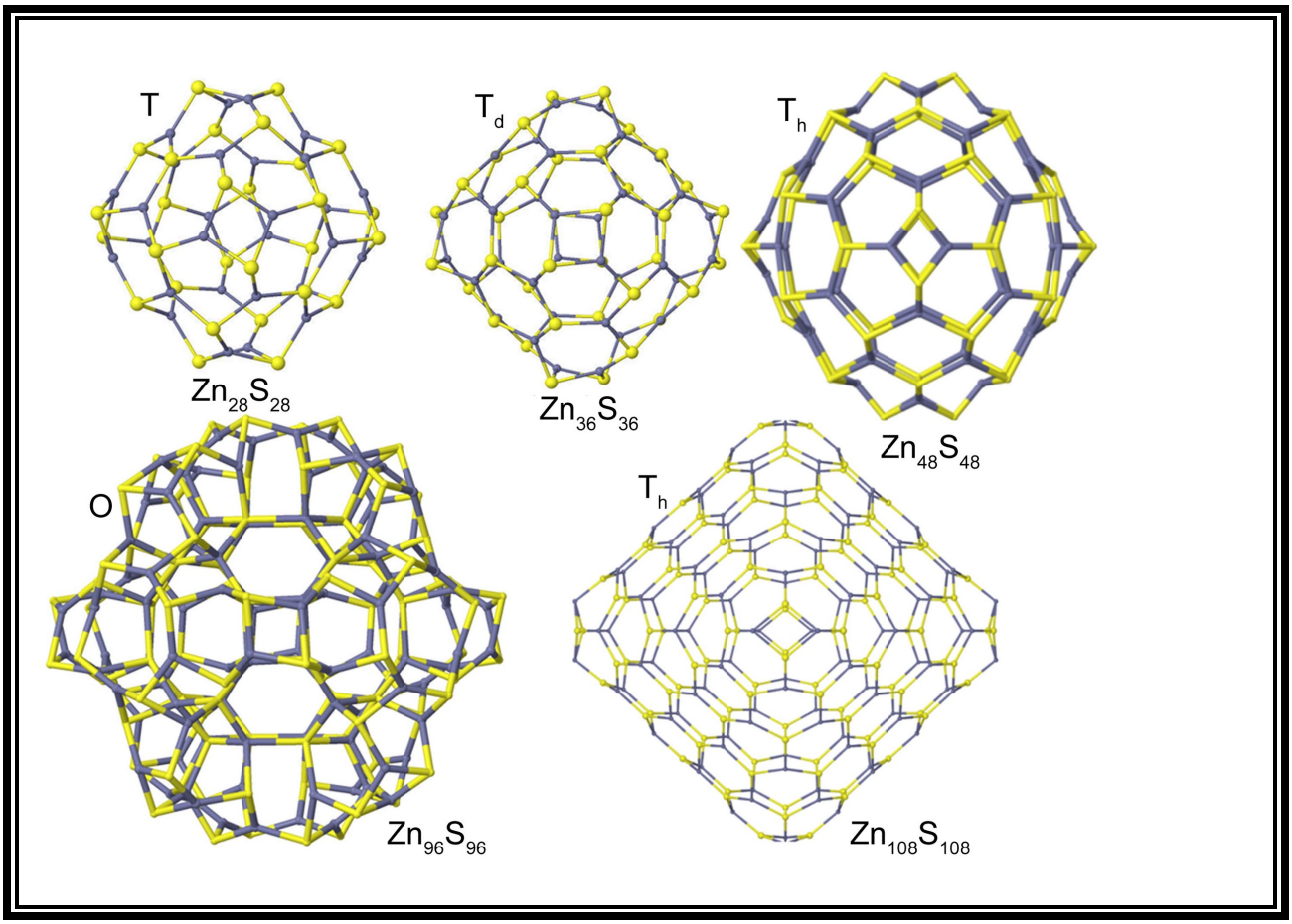

Figure 7.2: Optimized structures of $Zn_{28}S_{28}$, $Zn_{36}S_{36}$, $Zn_{48}S_{48}$, $Zn_{96}S_{96}$ and $Zn_{108}S_{108}$. Zn and S atoms are represented by gray and yellow circles, respectively. Molecular symmetry is also given.

The atoms in the onion-like structures, on the other hand, have predominantly four fold coordination. Since ZnS is a heteroatomic system, the stoichiometric cage structures of ZnS cannot be obtained using carbon fullerene cages as a template due to the presence of five member rings (pentagons) in it. In fullerenes, the pentagons introduce curvature to form a closed structure. However, the presence of pentagons precludes alternative arrangement of Zn and S atoms. Closed structures can also be obtained using four member (squares) instead of five member rings. Using Euler's polyhedral formula it can be shown that for three-fold coordinated

systems exactly six squares are required which permit alteration of Zn and S atoms. Most cages structures reported herein contains squares (four member rings).

$Zn_{12}S_{12}$ Cage (T_h)

The smallest cage structures in which six squares are isolated is the $Zn_{12}S_{12}$ cage. The six squares in it are isolated from each other by eight hexagonal rings. It has T_h point group symmetry with two inequivalent atoms. The full $Zn_{12}S_{12}$ cage structure can be generated using the point group symmetry operations. This cage structure is similar to the sodalite cage that is the naturally occurring structural unit in zeolites. The cage has an average radius of 3.5 Å (Table 1). Spano and coworkers have reported onion-like clusters ($Zn_{12}S_{12}@Zn_{48}S_{48}$) whose inner core is $Zn_{12}S_{12}$ cage. They noted the radius of the inner $Zn_{12}S_{12}$ bubble clusters in this onion to be 3.75 Å which is in good agreement with 3.5 Å reported here, considering the differences in the $Zn_{12}S_{12}$ cage environment.

The (4,6) ZnS bond, shared by the square and hexagons, of 2.34 Å is slightly longer than the (6,6) bonds of 2.25 Å shared by two hexagons. In their study on small ZnS cages, Hamad and coworkers examined the radial distribution function to obtain geometrical properties of clusters[36] [235]. Their analysis of computed radial distribution functions indicated that the first neighbor Zn-S bond distance in the cages is approximately 2.25Å which is shorter than 2.34Å in bulk polymorphs . They also noted that the ZnS- bond distances to be more or less independent of the size of as observed from the shift in the first neighbor peak with respect to the size of the cluster. Our (6,6) Zn-S bond distance of 2.25Å in $Zn_{12}S_{12}$ cage is consistent with the findings of Hamad and coworkers. For the larger ZnS cages discussed below, the first nearest neighbor distances are in the range 2.25-2.29 Å in excellent agreement with distances reported by Hamad and coworkers[36] [235] with the exception of $Zn_{108}S_{108}$ cage for which the shortest distance is 2.03Å.

$Zn_{16}S_{16}$ Cage (D_{2d})

The $Zn_{16}S_{16}$ cage has D_{2d} point group symmetry. The (4,6) bond is 2.32 Å long, the (6,6) bond is 2.28 Å long, and the atoms in this cage are on the shells with radii ranging from 3.61-4.16 Å. The $Zn_{16}S_{16}$ cage can be built by adding four Zn and four S atoms bringing the exterior ring of $Zn_{12}S_{12}$.

$Zn_{24}S_{24}$ Cages (O, S_4 and S_8)

The structures considered for $Zn_{24}S_{24}$ are octahedral O, S_4 and S_8 symmetric cages as shown in Figure 1. The octahedral O round cage contains six octagons, eight squares, and eight hexagons and it is defined by only two symmetry inequivalent atoms.

Table 7.1: Molecular symmetry, bond lengths, angles between Zn and S atoms and cage radii for the optimized Zn_xS_x cages.

Systems	Symmetry	Zn-S(Å)	Zn-S-Zn (º)	S-Zn-S (º)	Cage radius (Å)
$Zn_{12}S_{12}$	T_h	2.25, 2.34	76.7, 100.0	97.3, 130.7	3.22-3.83
$Zn_{16}S_{16}$	D_{2d}	2.28, 2.32	76.4, 104.4	97.6, 131.1	3.61-4.16
$Zn_{24}S_{24}$	O	2.24, 2.32	79.2, 104.9,	95.5, 126.0	4.78-5.28
	S_4	2.25, 2.31	74.3, 104.9,	113.9, 131.2	4.38-5.83
	S_8	2.27, 2.32	77.7, 102.0	113.4, 139.8	4.35-5.51
$Zn_{28}S_{28}$	T	2.28, 2.38	75.8, 103.6	118.6, 125.2	4.37-6.02
$Zn_{36}S_{36}$	T_d	2.28, 2.32	76.5, 104.0	117.4, 124.8	5.78-6.83
$Zn_{48}S_{48}$	T_h	2.05, 2.58, 2.66	93.8, 108.0, 113.5	106.6, 111.5, 131.2	6.99-7.60
$Zn_{96}S_{96}$	O	2.34, 2.46, 2.70	89.5, 99.2, 108.2	87.3, 112.5, 133.7	3.40-5.56,
$Zn_{108}S_{108}$	T_h	2.03, 2.17, 2.25	78.6, 116.2, 124.1	118.1, 125.9, 148.9	12.14-12.52

This round cage has been proposed as candidate structure for carbon,[53] [252] silicon hydrides,[54] [253] boron oxides,[54] [253] aluminum hydrides,[54] [253] aluminum nitrides,[55] [254] and for the experimentally observed $B_{24}N_{24}$ species.[56] [255] On the other hand, the S_4 symmetric cage does not contain any octagon and satisfies the isolated square rule.[57] [256] This rule is similar to the isolated pentagon rule for carbon fullerenes. The S_4 cage contains 20 hexagons and six squares and is a

fullerene like analog of a boron nitride fullerene. Finally, the S_8 cage contains two octagons, eight squares, and 12 hexagons and can be defined as a very short closed capped (4,4) nanotube. The S_4 cage was found to be the most stable structure followed by the S_8 and O cages which are 0.43 and 2.21 eV higher in energy. Zn-S bond lengths range from 2.24-2.32 Å and all three structures have atoms on shells with radii of 4.8 to 5.8 Å as summarized in Table 1.

$Zn_{28}S_{28}$ Cages (T) and $Zn_{36}S_{36}$ Cages (T_d)

The $Zn_{28}S_{28}$ cage of T symmetry and the tetrahedral $Zn_{36}S_{36}$ (T_d) cages shown in Figure 2 also satisfy the isolated six square rule. $Zn_{28}S_{28}$ contains 24 hexagons and it has six fourfold rings that are isolated by hexagonal rings, while $Zn_{36}S_{36}$ has 32 hexagons. The boron nitride counterparts of both these structures have been proposed as candidate structures for the abundant boron nitride clusters detected in mass spectrum. Zn-S bond lengths range from 2.28-2.38Å for both cages and the cage radius of $Zn_{28}S_{28}$ of 4.4-6.0 Å is comparable to the one of the $Zn_{24}S_{24}$ cages. The atoms in the $Zn_{36}S_{36}$ cage are on the shell with a larger radii of 5.8 to 6.0 Å (Table 1).

$Zn_{48}S_{48}$ Cage (T_h)

The point group symmetry of $Zn_{48}S_{48}$ cage is T_h. It is the second hollow cage structure from the $24n^2$ family of octahedral (tetrahedral for ZnS) cages. The first cage in this series is the $Zn_{12}S_{12}$ cage. The $Zn_{48}S_{48}$ cage can be obtained from the $Zn_{12}S_{12}$ cage structure by addition of hexagons and maintaining the symmetry point group. The positions of the other atoms can be determined from the symmetry group operations of an octahedral point group with symmetry axes along the coordinate axes. The cage has three ZnS bond lengths of 2.05, 2.58 and 2.66 Å. The atoms in this cage are on the shells with radii ranging from 7.0 to 7.6 Å.

$Zn_{96}S_{96}$ Cage (*O*)

$Zn_{96}S_{96}$ cluster is a larger cage that can be built by surrounding all square and octagonal defects of $Zn_{24}S_{24}$ (*O* symmetry) by rings of hexagons like leapfrogging in fullerenes,[58] [257] species that are necessarily closed electronic shells with large HOMO-LUMO gaps like in the present case. $Zn_{96}S_{96}$ presents an onion-like or "double bubble" structure containing 18 defects: 12 squares and six octagons and has squares sticking out as it is evident from the structure shown in Figure 2. The cage has an average radius of 3.4-5.5 Å and the squares protrude out by roughly 3.6 Å from the average radius. The average Zn-S bond lengths range from 2.34-2.70 Å and shows that this larger cage would prefer a solid-like cage structure rather than be a hollow cage.

$Zn_{108}S_{108}$ Cages (T_h)

The $Zn_{108}S_{108}$ cage is the largest hollow cluster we have studied. Because of its symmetry, the optimized $Zn_{108}S_{108}$ cage has three characteristic ZnS bond lengths of 2.03, 2.17 and 2.25 Å with atoms on the shells with radii of 10.0-12.52 Å. As compared to the C_{60} fullerene which has radius of 3.5 Å, $Zn_{108}S_{108}$ cage had a radius 3 times as large and an inner volume 9 times larger. Such larger cavity means the cage can easily accommodate rather large clusters and organic molecules.

Chemical Stability and Optical Properties

The chemical inertness of the clusters correlates with the gap between the highest occupied and the lowest unoccupied molecular orbitals, HOMO-LUMO gap. A large value of HOMO-LUMO gap is the indicative of chemical stability, where the system resists for both the change in number of electrons and the deformation of electronic cloud. All clusters considered here have closed shell structures with a relatively large HOMO–LUMO gaps, as shown in Table 2. In practical density functional theory applications, the HOMO-LUMO gaps as estimated from

the Kohn-Sham eigenvalues are often underestimated by as much as by 50% if standard local density approximation (LDA) or generalized gradient approximation (GGA) functionals are used due to the fact that the approximations made in modeling the exchange-correlation effects by these functional do not capture the so called derivative discontinuity in the exchange-correlation potential, and also these functionals suffer from self-interaction errors.

Table 7.2: Molecular symmetry, HOMO-LUMO gaps (HL gap), vertical electron affinity (vEA), vertical ionization potential (vIP), binding energies (BE), fundamental gaps (Eg), and optical transitions for the optimized Zn_xS_x clusters. All values are reported in units of eV.

	Symmetry	**HL gap**	**vEA**	**vIP**	**BE**	**Eg (quasi)**	**TDDFT Optical**
$Zn_{12}S_{12}$	T_h	3.25	1.79	7.94	5.49	6.15	4.38
$Zn_{16}S_{16}$	D_{2d}	3.18	1.65	8.06	5.54	6.40	4.01
$Zn_{24}S_{24}$	O	3.27	2.17	7.63	5.48	5.47	
	S_4	3.06	2.18	7.54	5.60	5.36	
	S_8	3.17	2.39	7.31	5.55	4.92	
$Zn_{28}S_{28}$	T	3.17	2.95	6.81	5.58	3.87	
$Zn_{36}S_{36}$	T_d	2.97	2.43	7.29	5.59	4.86	
$Zn_{48}S_{48}$	T_h	3.07	2.50	7.3	5.60	4.79	
$Zn_{96}S_{96}$	O	2.48	2.58	6.80	5.54	4.21	
$Zn_{108}S_{108}$	T_h	2.97	2.73	6.92	5.63	4.19	

Recent formulations for correcting for the self-interaction corrections using Fermi orbitals offer a promising route,[59-62] [258] [259] [260] [261] however, these are not yet available for routine calculations. The theoretically calculated band gaps (Kohn-Sham gaps) for the cubic bulk ZnS are in the range 1.7-2.1 eV depending on the type of functional used,[63-66] [262] [263] [264] [265] while the experimental gap for the most stable cubic form of ZnS is 3.54 eV.[67] [266]

An accurate estimate of the fundamental gap can be obtained using the GW approximation. However, these calculations are computationally very expensive. On the other hand, the fundamental gap (E_g^{quasi}) concerns energy differences in the electron removal energy and the energy released when an electron is added to the system. Experimentally, E_g^{quasi} can be measured using scanning tunneling microscope and ultraviolet photoelectron spectroscopy. For finite systems, the quasiparticle gap can be obtained from the total energy differences of the charged (cation, anion) and neutral clusters according to the following equation:

$$E_g^{quasi} = E(N+1) + E(N-1) - 2E(N)$$

where E(N) is the self-consistent total energy of an N electron system. Notably, density functional theory, even within the standard exchange-correlation functionals such as GGA, can provide accurate estimates of the total energy differences in the above equation.[68-69] [267] [268] The computed HOMO-LUMO gaps (Kohn-Sham eigenvalues), vertical electron affinities (vEA) and ionization energies (vIE), and fundamental gaps (E_g) are presented in Table 2.

A number of observations can be made from this table. All cage structures are characterized by large HOMO-LUMO gap. The smallest $Zn_{12}S_{12}$ cage has a HOMO-LUMO gap of 3.25 eV while the $Zn_{96}S_{96}$ cage has the smallest value (~2.5eV). These values are larger than the band gap (1.7-2.1 eV) for the bulk ZnS indicating the finite size (quantum confinement) effects in these cages. Hamad and coworkers[36] have also examined the HOMO-LUMO gaps for the bubble clusters (cages), onion-like clusters, and bulk-like clusters in the size range of 10 to 80 atoms. They scaled the HOMO-LUMO gap values by adding 1.5 eV energy shift estimated from the difference between the calculated band gap (2.1 eV) for the bulk and the experimental value of the ZnS band gap (3.6 eV). They noted that the band gap of bubble clusters does not change substantially with the cluster size. They furthermore observed that the band gaps of

double bubble (onion-like) clusters are smaller than those of single cages. Our results essentially corroborate these observation. Our calculated values of the HOMO-LUMO gaps are in the range 2.5 to 3.25 eV which agree with those reported by Hammad and coworker (2.7 to 3.3 eV after subtraction of the *ad hoc* shift). Furthermore, in agreement with their results, $Zn_{12}S_{12}$ is found to posses one of the highest values of HOMO-LUMO gap (3.25 eV) while the onion-like $Zn_{96}S_{96}$ has the smallest (~ 2.5 eV) value. The E_g^{quasi} range from 6.4 eV (for $Zn_{16}S_{16}$) to 3.9 eV (for $Zn_{28}S_{28}$). The rather larger values of these gaps are indicators of the chemical stability of these cage clusters. For the smallest two clusters, we have computed the optical gaps using the linear response formulation of the time dependent DFT. The restriction to the small system was due to the computational cost of these calculations using high quality basis sets (such as those used in ground state and vibrational calculations). The optical gaps are 4.38 eV for $Zn_{12}S_{12}$ and 4.01 eV for the $Zn_{16}S_{16}$ cages (Table 2). These results allow us to estimate the exciton binding energies in these two systems. Between these two cages, the larger fundamental gap of 6.4 eV and smaller optical gap of 4.01 eV results in larger exciton binding energy in the $Zn_{16}S_{16}$ cage. The exciton binding energy in the cage of $Zn_{12}S_{12}$ is 1.47 eV.

To further visualize the electronic spectrum we calculated the density of states (DOS) which is shown in Figure 3. The DOS shows that the position of the Fermi level in all cages are nearly aligned except for the $Zn_{96}S_{96}$ cage. The HOMO-LUMO gap of this cluster is smaller compared to the other clusters by nearly 0.5 eV. We point out that some of the atoms in this cage are in 4-fold coordination whereas the atoms in all the other cages are only in 3-fold coordination. The distinct bonding in $Zn_{96}S_{96}$ is reflected in the density of states with a high lying HOMO level. The partial DOS of $Zn_{12}S_{12}$ and $Zn_{96}S_{96}$ are provided in the supplementary information section. The partial DOS of the these two cages show that the valence orbitals are

predominantly of *p*-character originating from the S *p* orbitals. The *d*-orbitals of Zn lie deep in energy. The contribution of the 4s orbitals of Zn is also seen in the occupied orbitals near Fermi level. This feature also confirms that the charge transfer from the Zn 4s orbitals to the p-orbitals of S atoms is not complete as also seen from the NBO analysis.

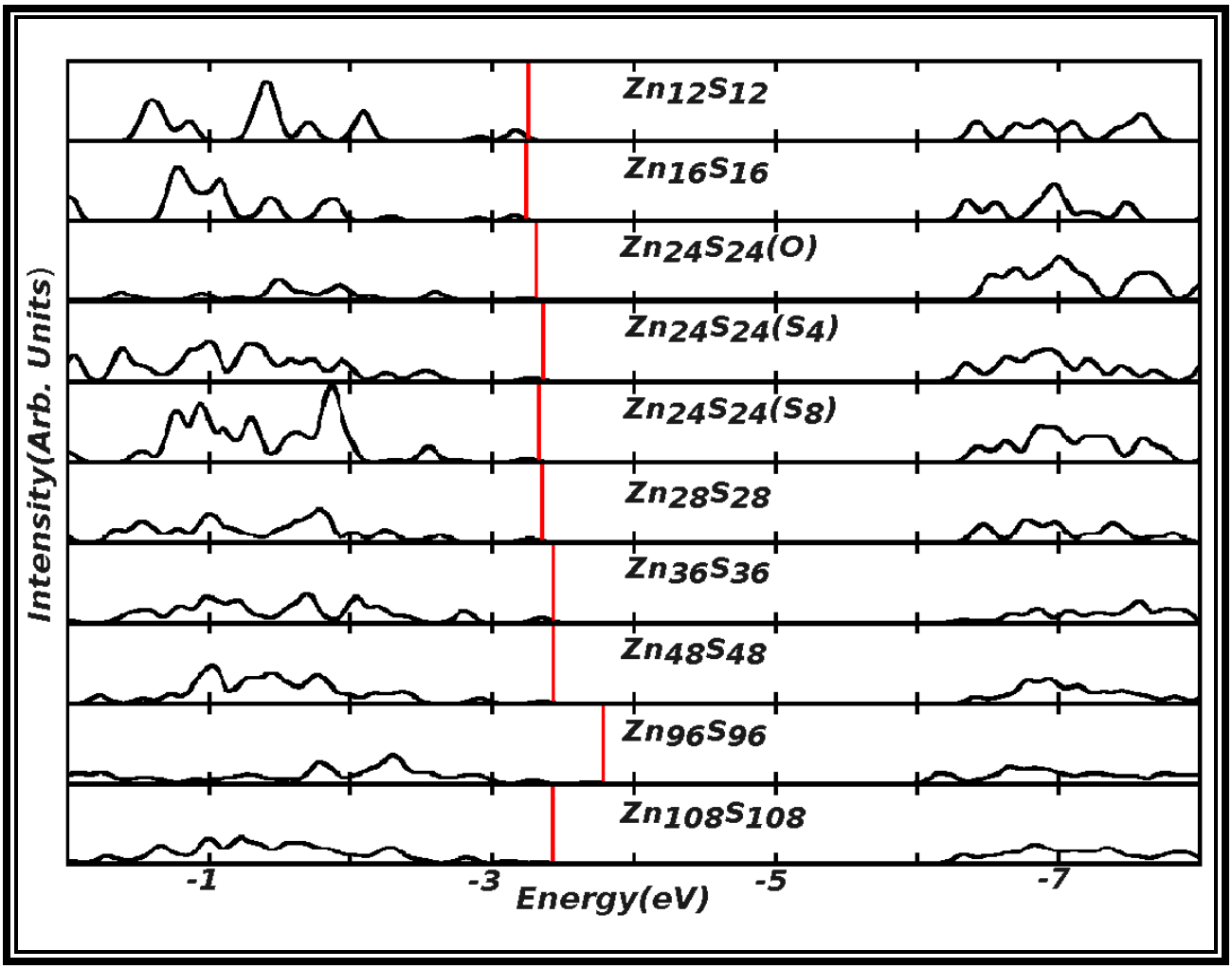

Figure 7.3: The density of states (DOS) plot of the Zn_xS_x clusters as a function of the cluster size.The red lines are the fermi levels. The levels plotted on the right side of the fermi levels are unoccupied states and to those at the right are the occupied levels. They are plotted in the order of Zn_xS_x clusters (x= 12, 16, 24-O, 24-S_4, 24-S_8, 28, 36, 48, 96, and 108) from top to bottom.

Energetic Stability

To investigate the energetic stability of the ZnS bubble-cages we computed the binding energy per ZnS pair atom of the Zn_xS_x clusters according to the equation:

$$BE = -\frac{[E(Zn_xS_x) - xE(Zn) - xE(S)]}{x}$$

where E(Zn_xS_x), E(Zn), and E(S) are the total energies of the Zn_xS_x, Zn and S species respectively. Note that according to this definition the larger the binding energy, more energy is required to separate the cluster into its atomic components, and therefore, the more stable is the species. The binding energies per atom of the clusters were all found to be positive around 5.0 eV per ZnS pair, and increased with cage size from 5.49 eV for $Zn_{12}S_{12}$ to 5.58 eV for the larger species as shown in Table 1. Further, the binding energy increases slowly towards the cohesive energy (6.3 eV) of the zinc-blende bulk ZnS.

Vibrational Frequency and Infrared Spectra

The analysis of the vibrational frequencies show that the bubble clusters studied here are local minima on the potential energy surface and are viable structures for ZnS clusters. Several of these clusters possess soft modes below 50 cm^{-1} which may indicate low structural stability compared to the other clusters and possible structural transition under elevated temperature or pressure. These calculations are carried out at T=0K which does not include any temperature effects. The large HOMO-LUMO and optical gaps of these clusters however show that the free-standing clusters are chemically stable species.

The predicted infrared (IR) of the Zn_xS_x (x= 12, 16, 24, 28 and 36) cages are presented in Figs. 4. All the cages showed five main IR active modes centered around 250, 280 and 310, 360 and 380 cm^{-1}. The intensity of the high frequency, modes decreased for the larger sizes. On the contrary, the larger cages have more dispersion in their bond-lengths and hence their lower

spring constants resulted in more IR active modes at low frequencies. All modes and its degeneracy are given in supplemental informationS1-S6.

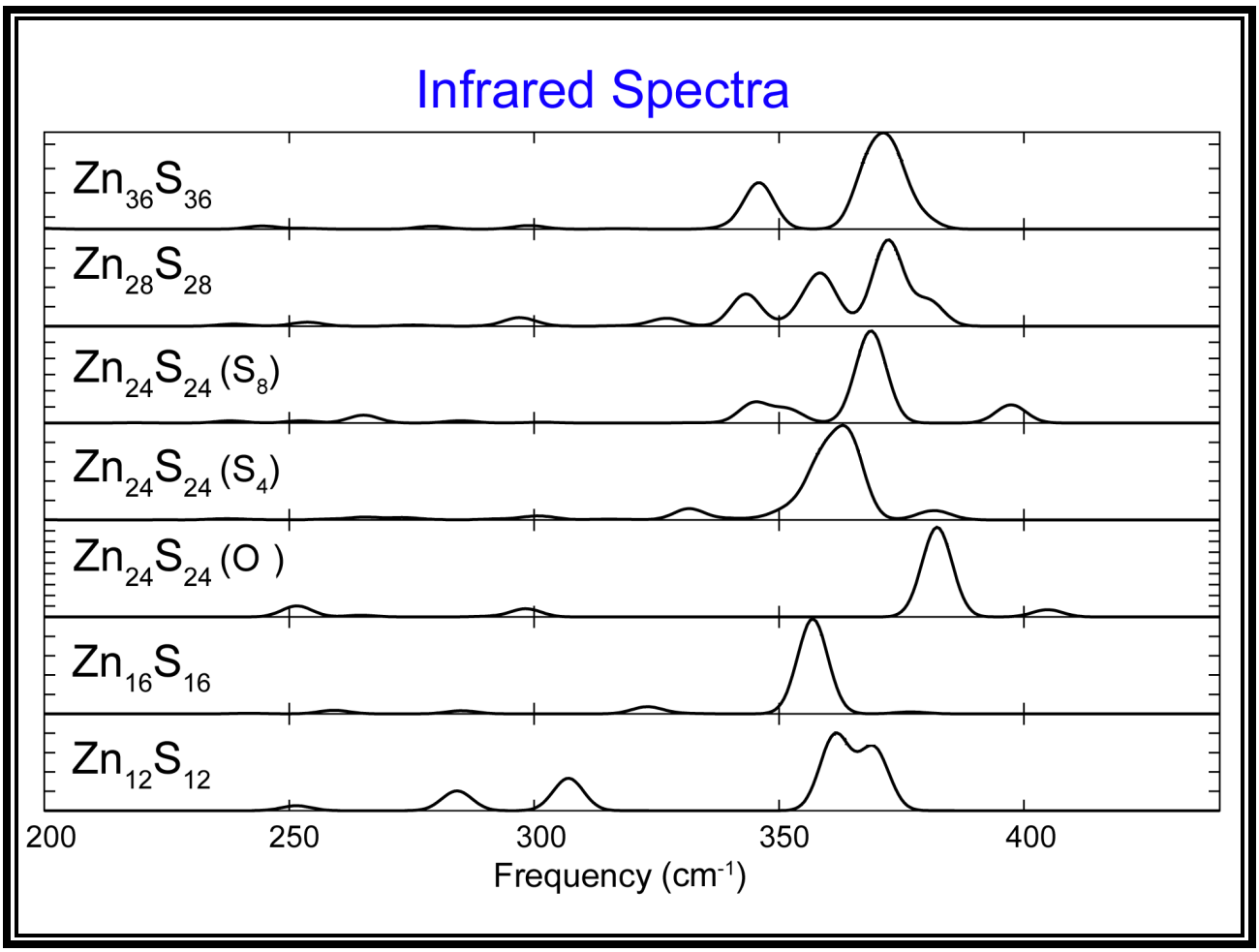

Figure 7.4: Infrared spectra of the Zn_xS_x clusters (x= 12, 16, 24, 28 and 36)

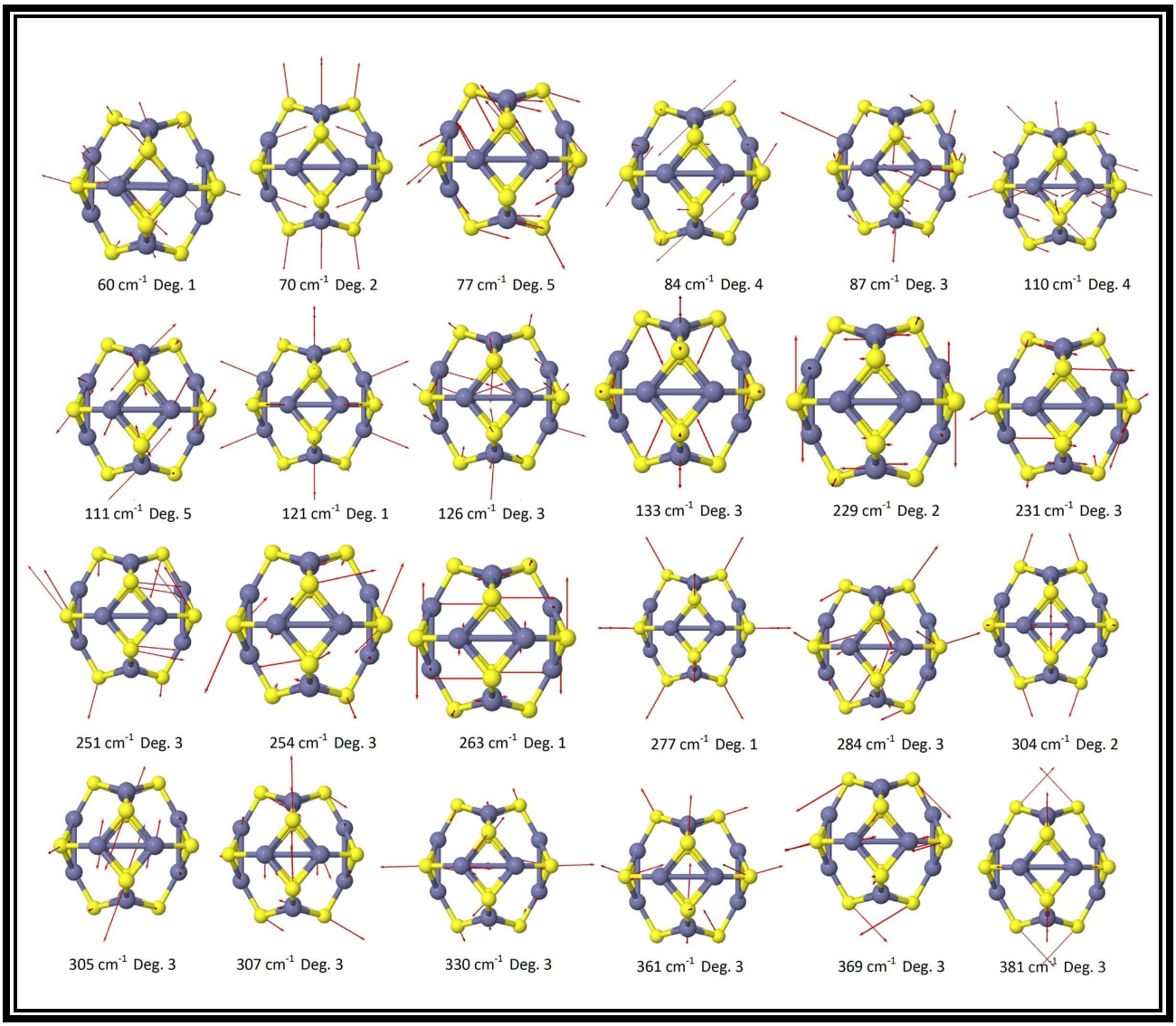

Figure 7.S1: Vibrational modes and frequencies for the $Zn_{12}S_{12}$ cage

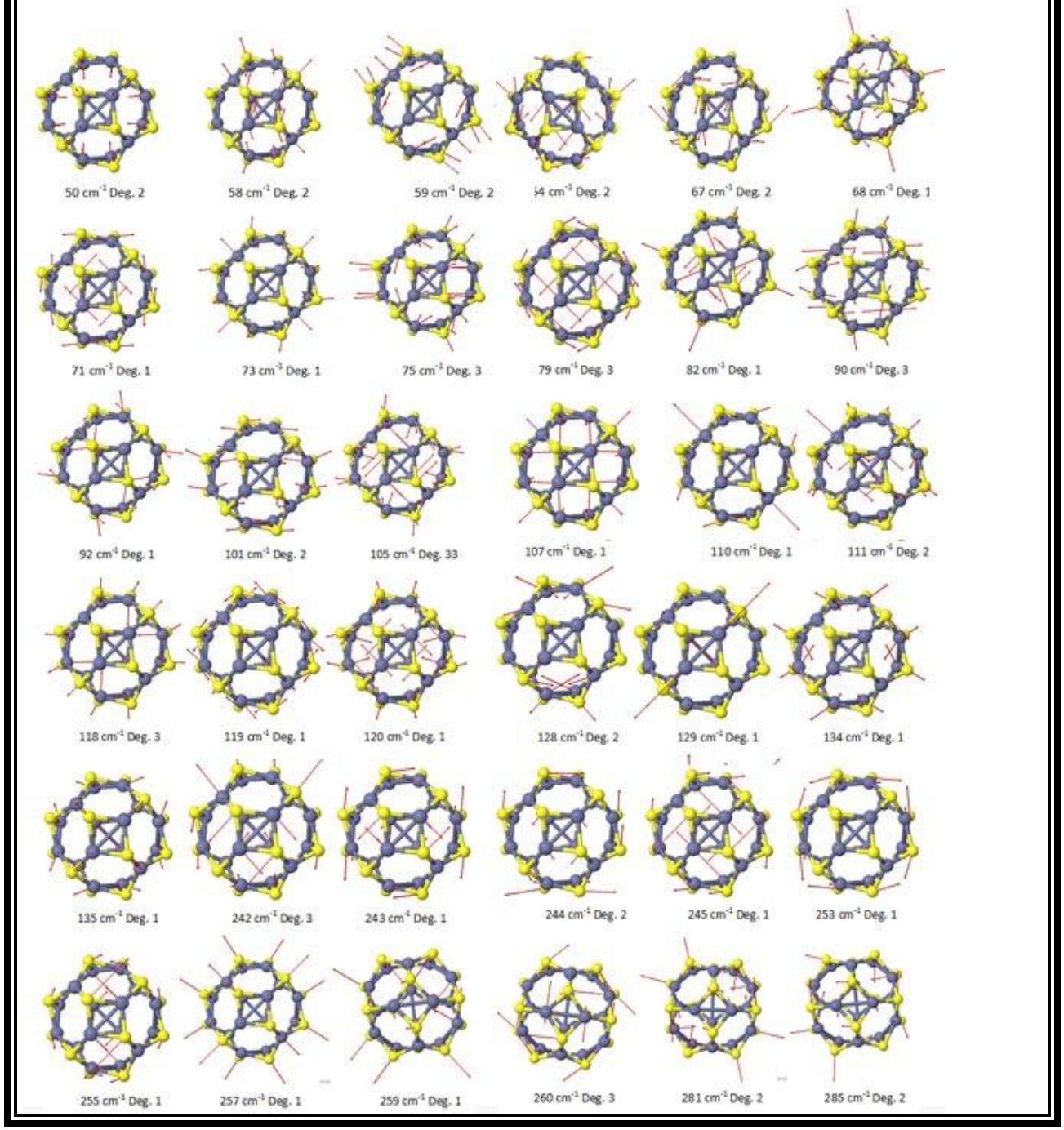
50 cm-1 Deg. 2
58 cm-1 Deg. 2
59 cm-1 Deg. 2
64 cm-1 Deg. 2
67 cm-1 Deg. 2
68 cm-1 Deg. 1
71 cm-1 Deg. 1
73 cm-1 Deg. 1
75 cm-1 Deg. 3
79 cm-1 Deg. 3
82 cm-1 Deg. 1
90 cm-1 Deg. 3
92 cm-1 Deg. 1
101 cm-1 Deg. 2
105 cm-1 Deg. 33
107 cm-1 Deg. 1
110 cm-1 Deg. 1
111 cm-1 Deg. 2
118 cm-1 Deg. 3
119 cm-1 Deg. 1
120 cm-1 Deg. 1
128 cm-1 Deg. 2
129 cm-1 Deg. 1
134 cm-1 Deg. 1
135 cm-1 Deg. 1
242 cm-1 Deg. 3
243 cm-1 Deg. 1
244 cm-1 Deg. 2
245 cm-1 Deg. 1
253 cm-1 Deg. 1
255 cm-1 Deg. 1
257 cm-1 Deg. 1
259 cm-1 Deg. 1
260 cm-1 Deg. 3
281 cm-1 Deg. 2
285 cm-1 Deg. 2

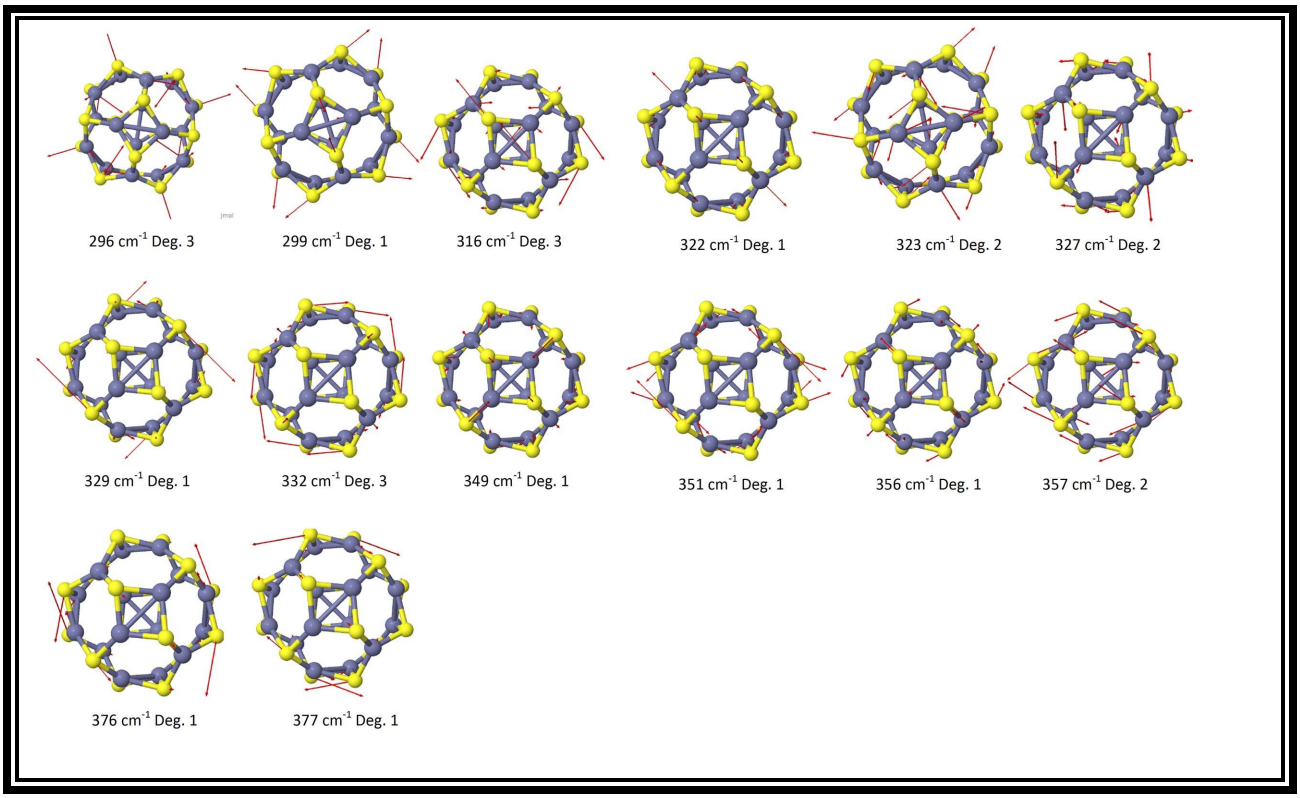

Figure 7.S2: Vibrational modes and frequencies of the $Zn_{16}S_{16}$ cage

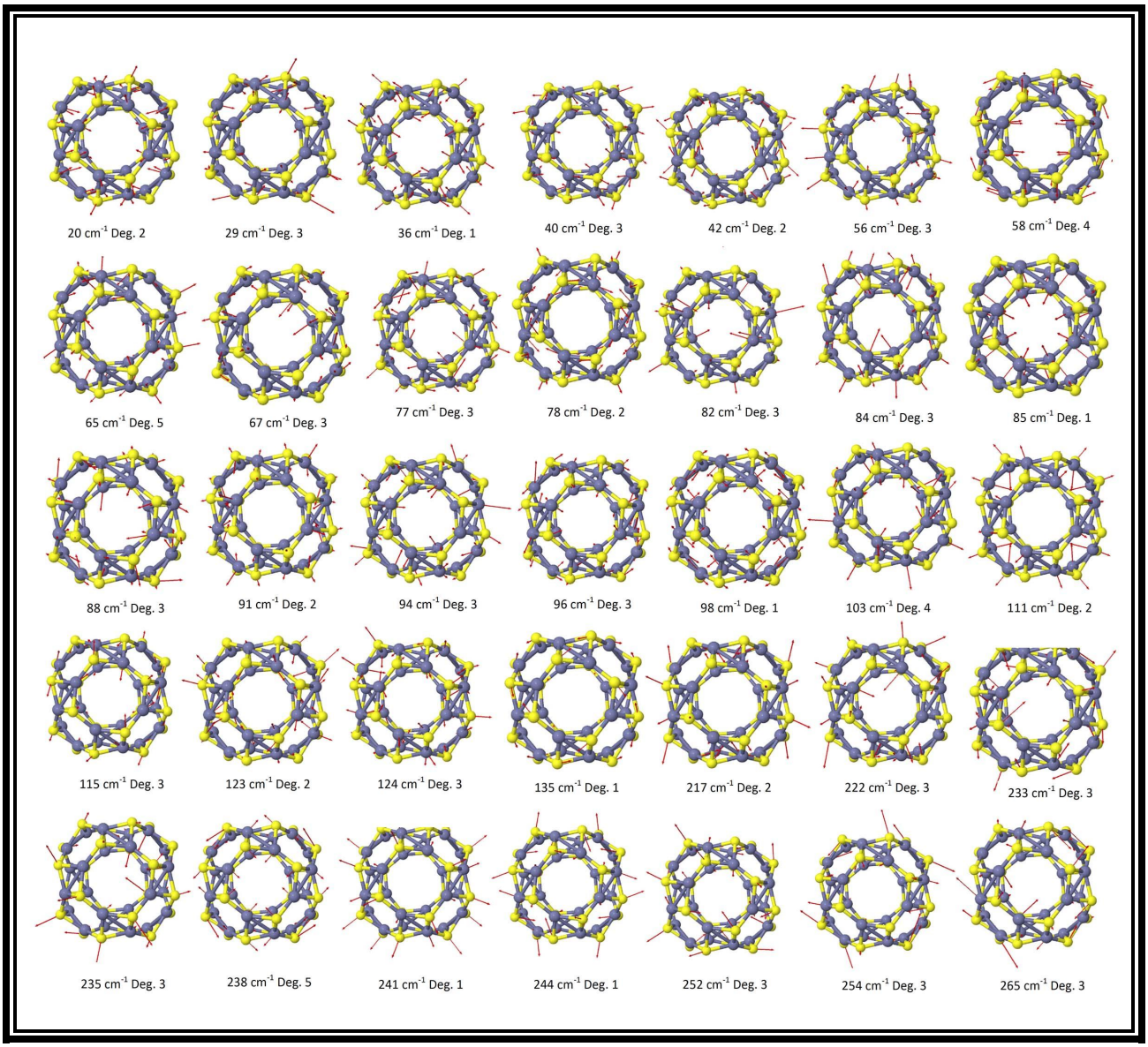
20 cm-1 Deg. 2
29 cm-1 Deg. 3
36 cm-1 Deg. 1
40 cm-1 Deg. 3
42 cm-1 Deg. 2
56 cm-1 Deg. 3
58 cm-1 Deg. 4
65 cm-1 Deg. 5
67 cm-1 Deg. 3
77 cm-1 Deg. 3
78 cm-1 Deg. 2
82 cm-1 Deg. 3
84 cm-1 Deg. 3
85 cm-1 Deg. 1
88 cm-1 Deg. 3
91 cm-1 Deg. 2
94 cm-1 Deg. 3
96 cm-1 Deg. 3
98 cm-1 Deg. 1
103 cm-1 Deg. 4
111 cm-1 Deg. 2
115 cm-1 Deg. 3
123 cm-1 Deg. 2
124 cm-1 Deg. 3
135 cm-1 Deg. 1
217 cm-1 Deg. 2
222 cm-1 Deg. 3
233 cm-1 Deg. 3
235 cm-1 Deg. 3
238 cm-1 Deg. 5
241 cm-1 Deg. 1
244 cm-1 Deg. 1
252 cm-1 Deg. 3
254 cm-1 Deg. 3
265 cm-1 Deg. 3

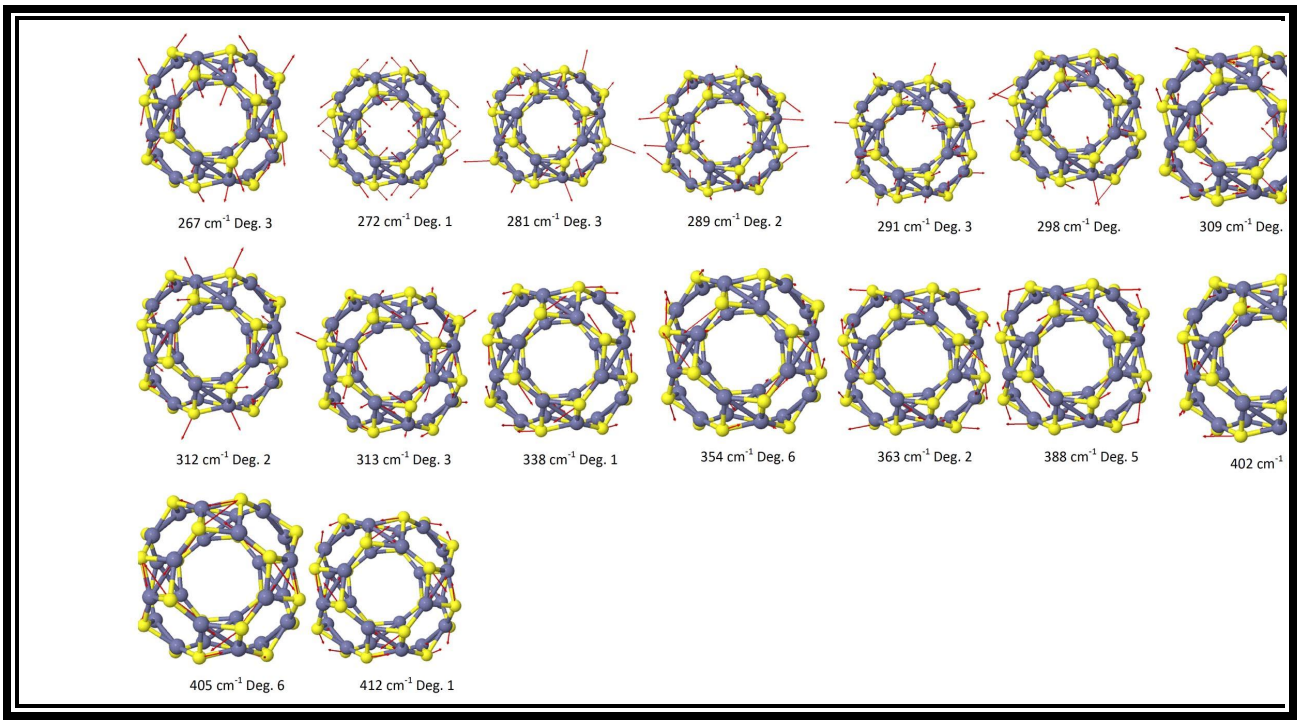

Figure 7.S3: Vibrational modes and frequencies for the $Zn_{24}S_{24}$ (*O* symmetry) cage.

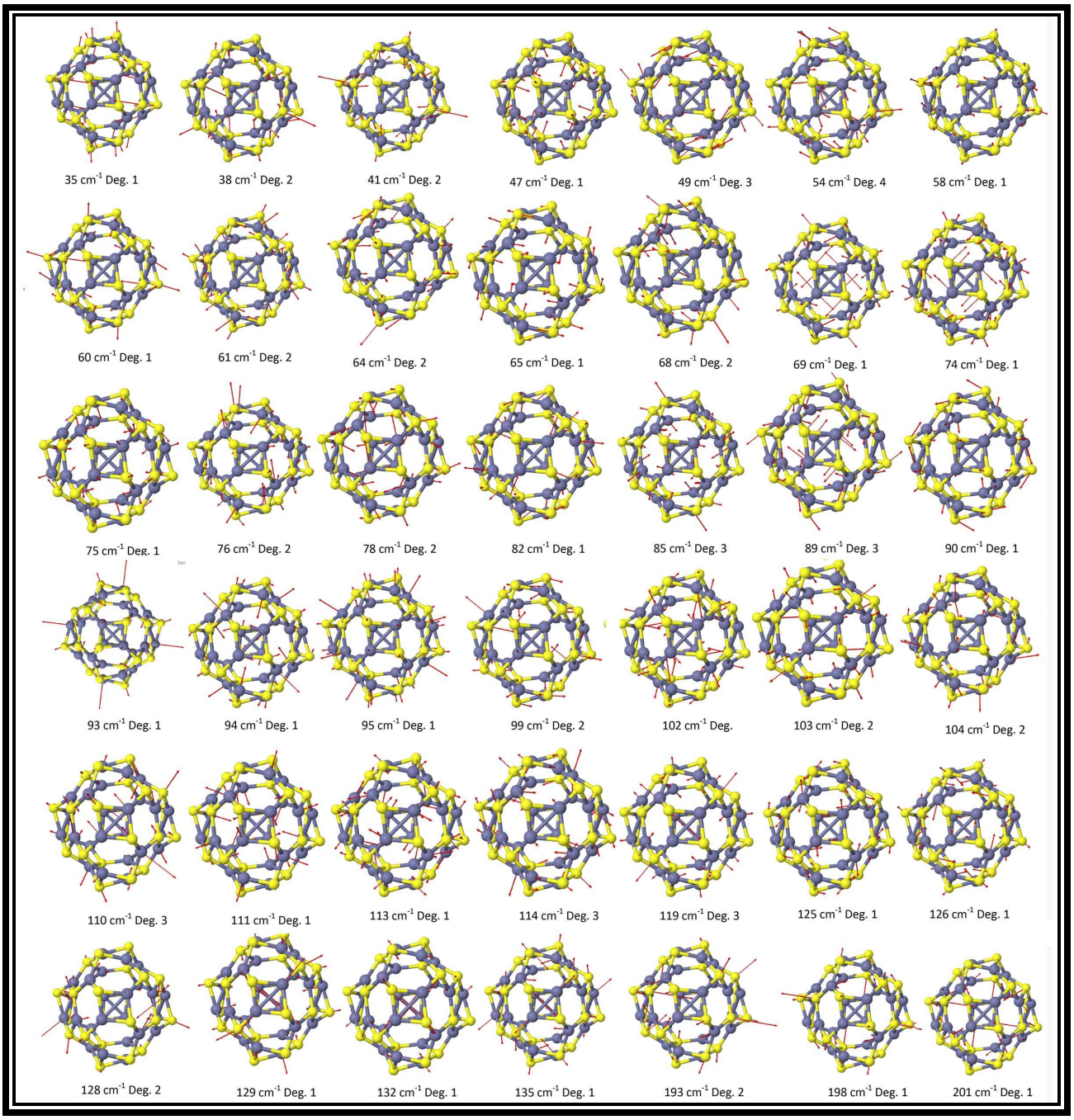
35 cm-1 Deg. 1
38 cm-1 Deg. 2
41 cm-1 Deg. 2
47 cm-1 Deg. 1
49 cm-1 Deg. 3
54 cm-1 Deg. 4
58 cm-1 Deg. 1
60 cm-1 Deg. 1
61 cm-1 Deg. 2
64 cm-1 Deg. 2
65 cm-1 Deg. 1
68 cm-1 Deg. 2
69 cm-1 Deg. 1
74 cm-1 Deg. 1
75 cm-1 Deg. 1
76 cm-1 Deg. 2
78 cm-1 Deg. 2
82 cm-1 Deg. 1
85 cm-1 Deg. 3
89 cm-1 Deg. 3
90 cm-1 Deg. 1
93 cm-1 Deg. 1
94 cm-1 Deg. 1
95 cm-1 Deg. 1
99 cm-1 Deg. 2
102 cm-1 Deg.
103 cm-1 Deg. 2
104 cm-1 Deg. 2
110 cm-1 Deg. 3
111 cm-1 Deg. 1
113 cm-1 Deg. 1
114 cm-1 Deg. 3
119 cm-1 Deg. 3
125 cm-1 Deg. 1
126 cm-1 Deg. 1
128 cm-1 Deg. 2
129 cm-1 Deg. 1
132 cm-1 Deg. 1
135 cm-1 Deg. 1
193 cm-1 Deg. 2
198 cm-1 Deg. 1
201 cm-1 Deg. 1

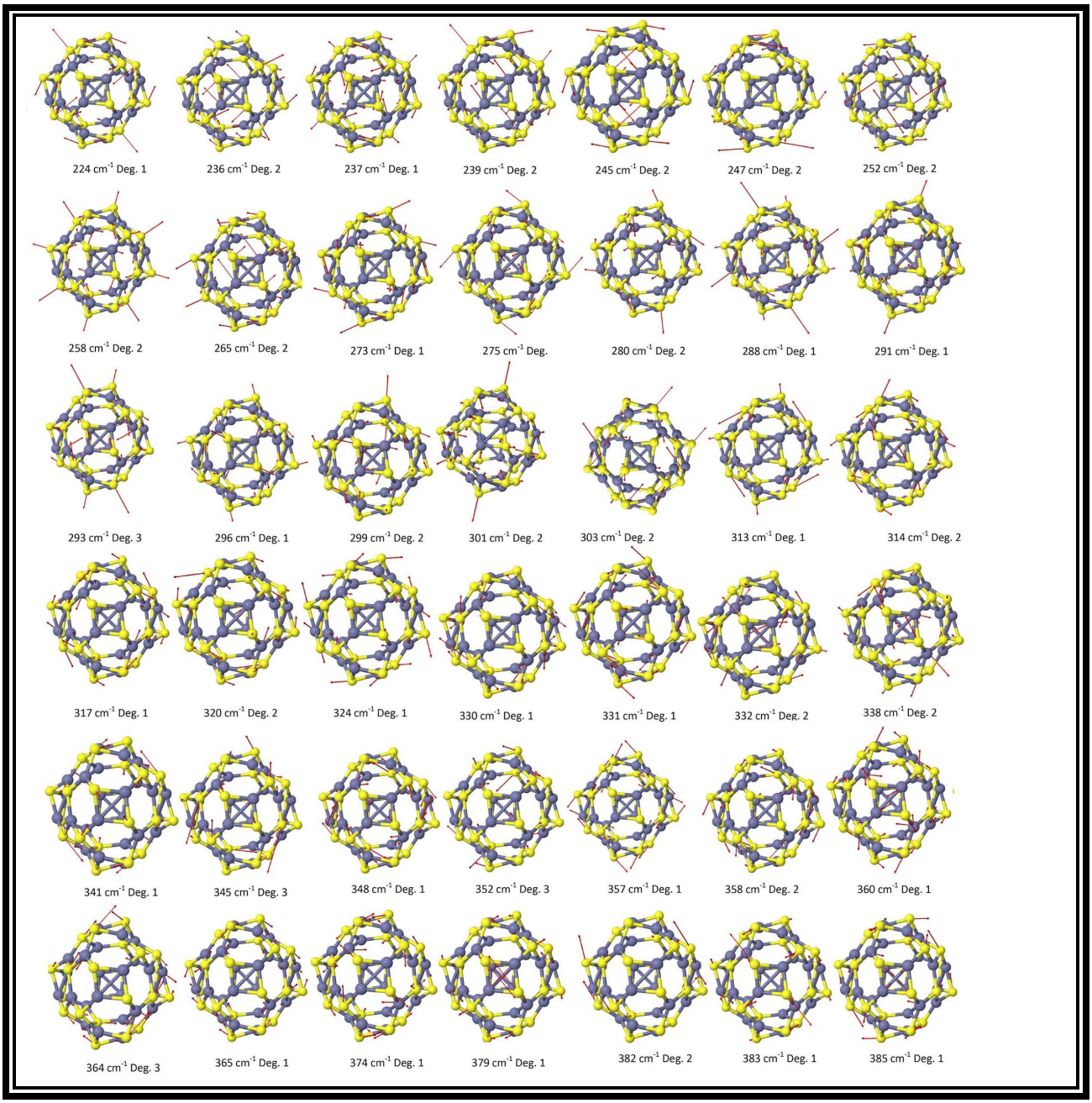

Figure 7.S4: Vibrational modes and frequencies for the $Zn_{24}S_{24}$ (S_4 symmetry) cage.

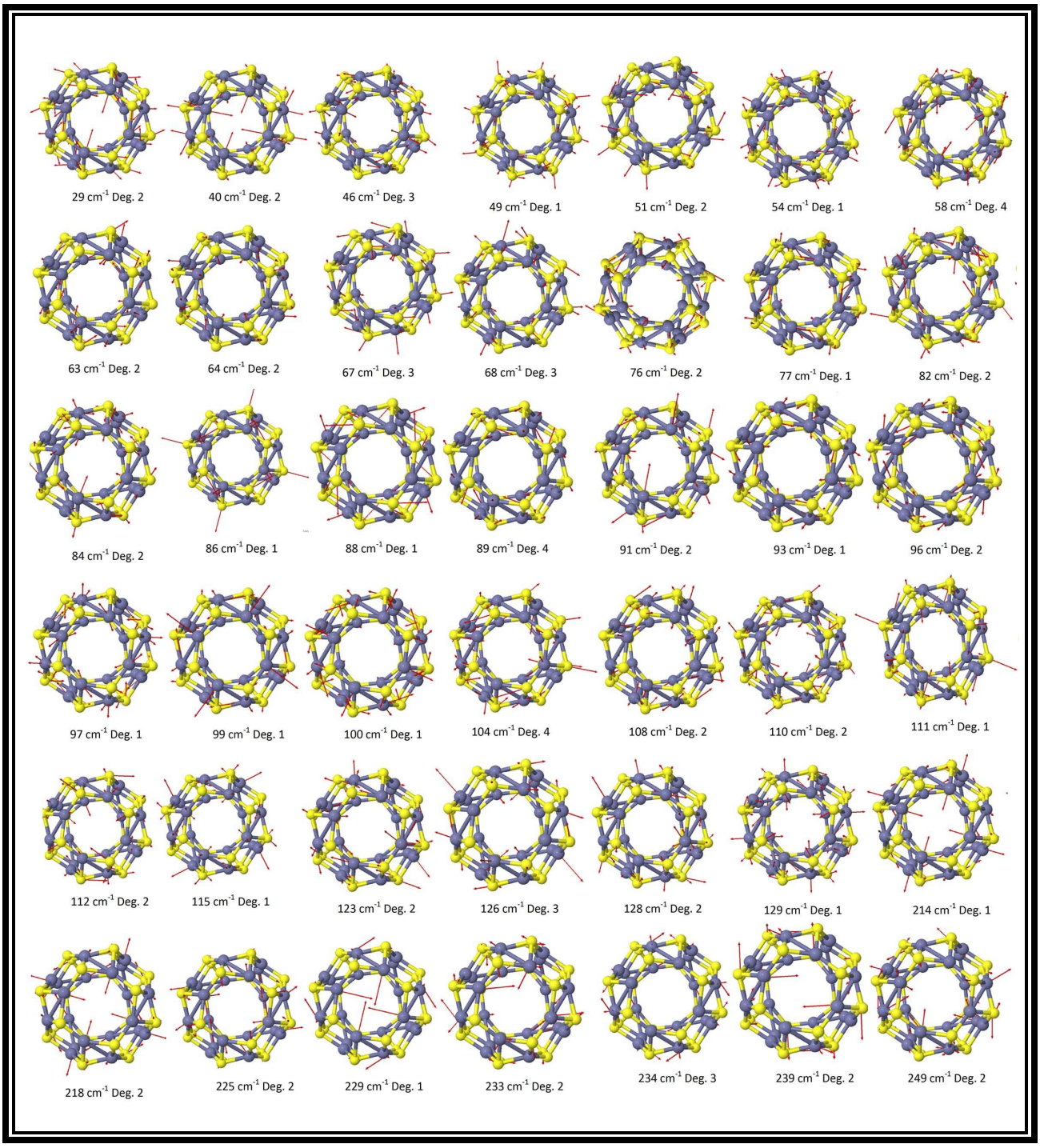
29 cm-1 Deg. 2
40 cm-1 Deg. 2
46 cm-1 Deg. 3
49 cm-1 Deg. 1
51 cm-1 Deg. 2
54 cm-1 Deg. 1
58 cm-1 Deg. 4
63 cm-1 Deg. 2
64 cm-1 Deg. 2
67 cm-1 Deg. 3
68 cm-1 Deg. 3
76 cm-1 Deg. 2
77 cm-1 Deg. 1
82 cm-1 Deg. 2
84 cm-1 Deg. 2
86 cm-1 Deg. 1
88 cm-1 Deg. 1
89 cm-1 Deg. 4
91 cm-1 Deg. 2
93 cm-1 Deg. 1
96 cm-1 Deg. 2
97 cm-1 Deg. 1
99 cm-1 Deg. 1
100 cm-1 Deg. 1
104 cm-1 Deg. 4
108 cm-1 Deg. 2
110 cm-1 Deg. 2
111 cm-1 Deg. 1
112 cm-1 Deg. 2
115 cm-1 Deg. 1
123 cm-1 Deg. 2
126 cm-1 Deg. 3
128 cm-1 Deg. 2
129 cm-1 Deg. 1
214 cm-1 Deg. 1
218 cm-1 Deg. 2
225 cm-1 Deg. 2
229 cm-1 Deg. 1
233 cm-1 Deg. 2
234 cm-1 Deg. 3
239 cm-1 Deg. 2
249 cm-1 Deg. 2

Figure 7.S5: Vibrational modes and frequencies for the $Zn_{24}S_{24}$ (S_8 symmetry) cage.

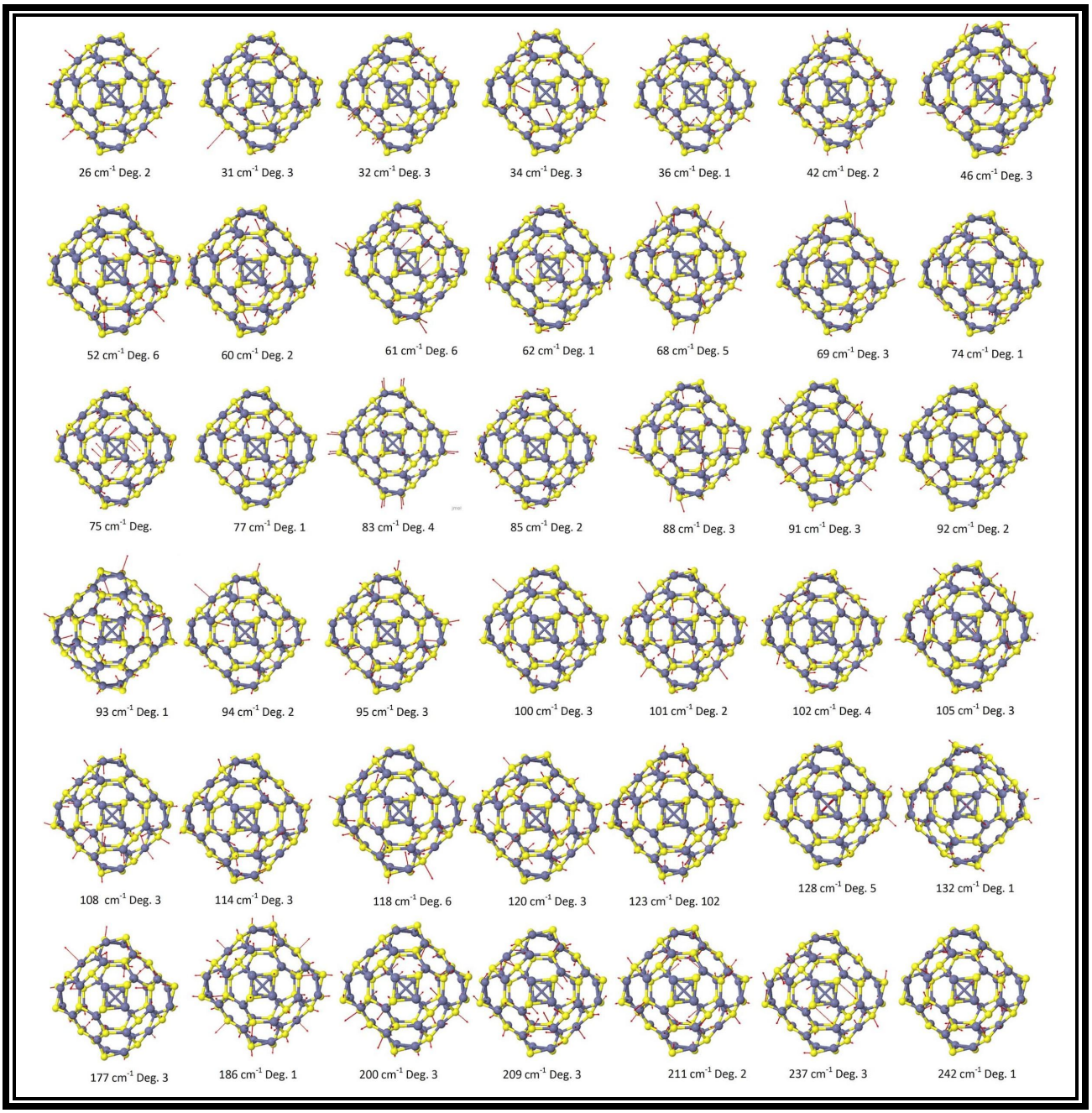
26 cm-1 Deg. 2
31 cm-1 Deg. 3
32 cm-1 Deg. 3
34 cm-1 Deg. 3
36 cm-1 Deg. 1
42 cm-1 Deg. 2
46 cm-1 Deg. 3
52 cm-1 Deg. 6
60 cm-1 Deg. 2
61 cm-1 Deg. 6
62 cm-1 Deg. 1
68 cm-1 Deg. 5
69 cm-1 Deg. 3
74 cm-1 Deg. 1
75 cm-1 Deg.
77 cm-1 Deg. 1
83 cm-1 Deg. 4
85 cm-1 Deg. 2
88 cm-1 Deg. 3
91 cm-1 Deg. 3
92 cm-1 Deg. 2
93 cm-1 Deg. 1
94 cm-1 Deg. 2
95 cm-1 Deg. 3
100 cm-1 Deg. 3
101 cm-1 Deg. 2
102 cm-1 Deg. 4
105 cm-1 Deg. 3
108 cm-1 Deg. 3
114 cm-1 Deg. 3
118 cm-1 Deg. 6
120 cm-1 Deg. 3
123 cm-1 Deg. 102
128 cm-1 Deg. 5
132 cm-1 Deg. 1
177 cm-1 Deg. 3
186 cm-1 Deg. 1
200 cm-1 Deg. 3
209 cm-1 Deg. 3
211 cm-1 Deg. 2
237 cm-1 Deg. 3
242 cm-1 Deg. 1

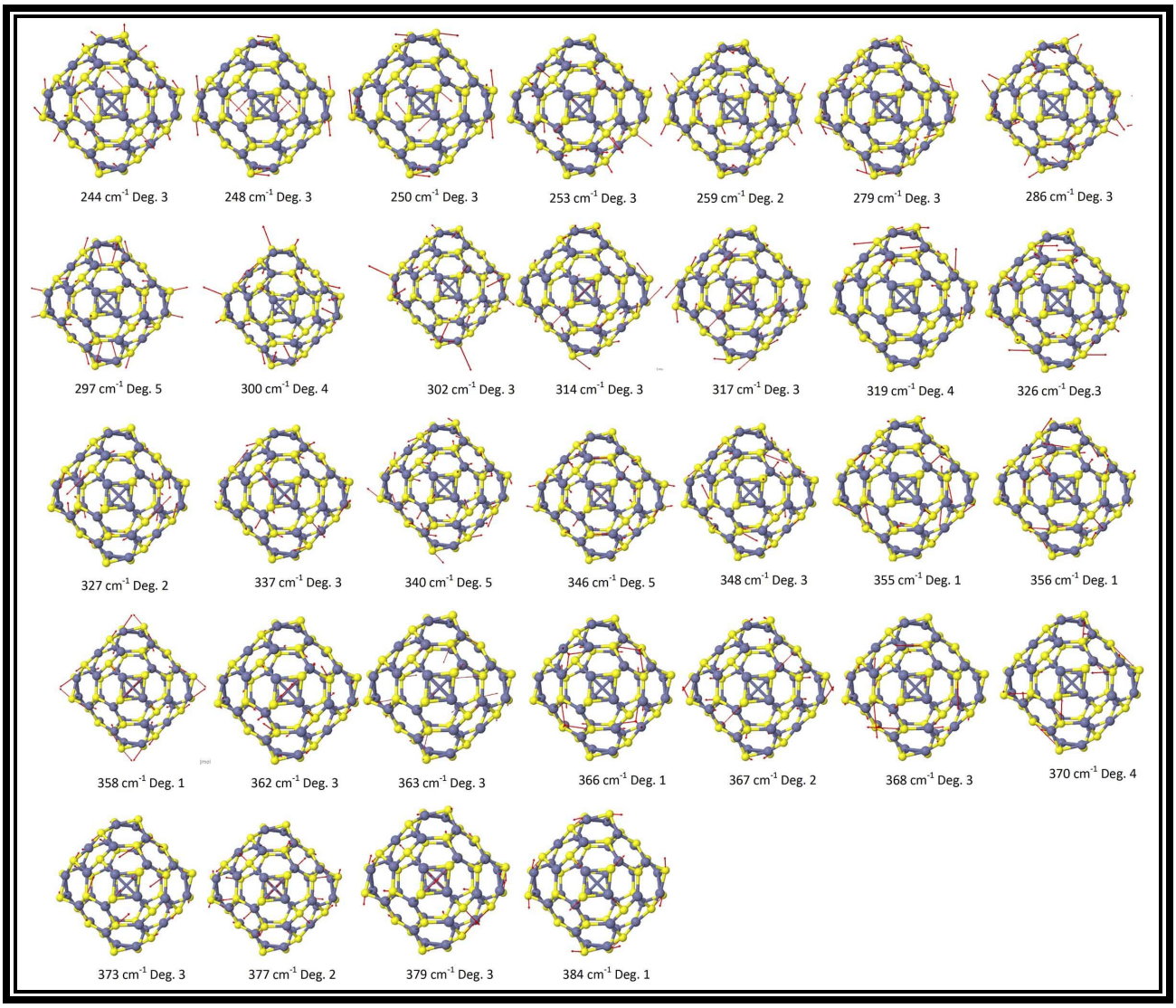

Figure 7.S6: Vibrational modes and frequencies for the $Zn_{36}S_{36}$ (S_4 symmetry) cage.

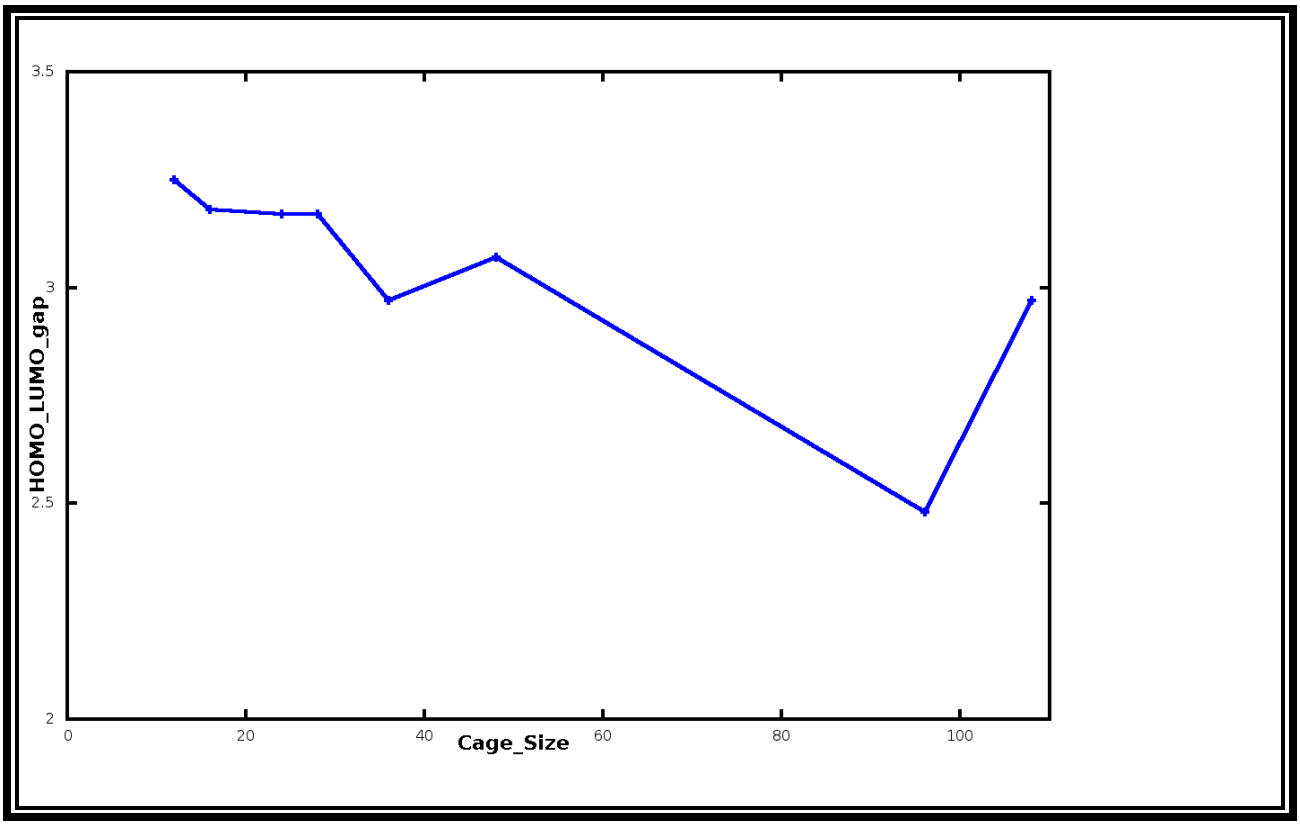

Figure 7.S7: Plot of HOMO_LUMO gap as a function of cage size

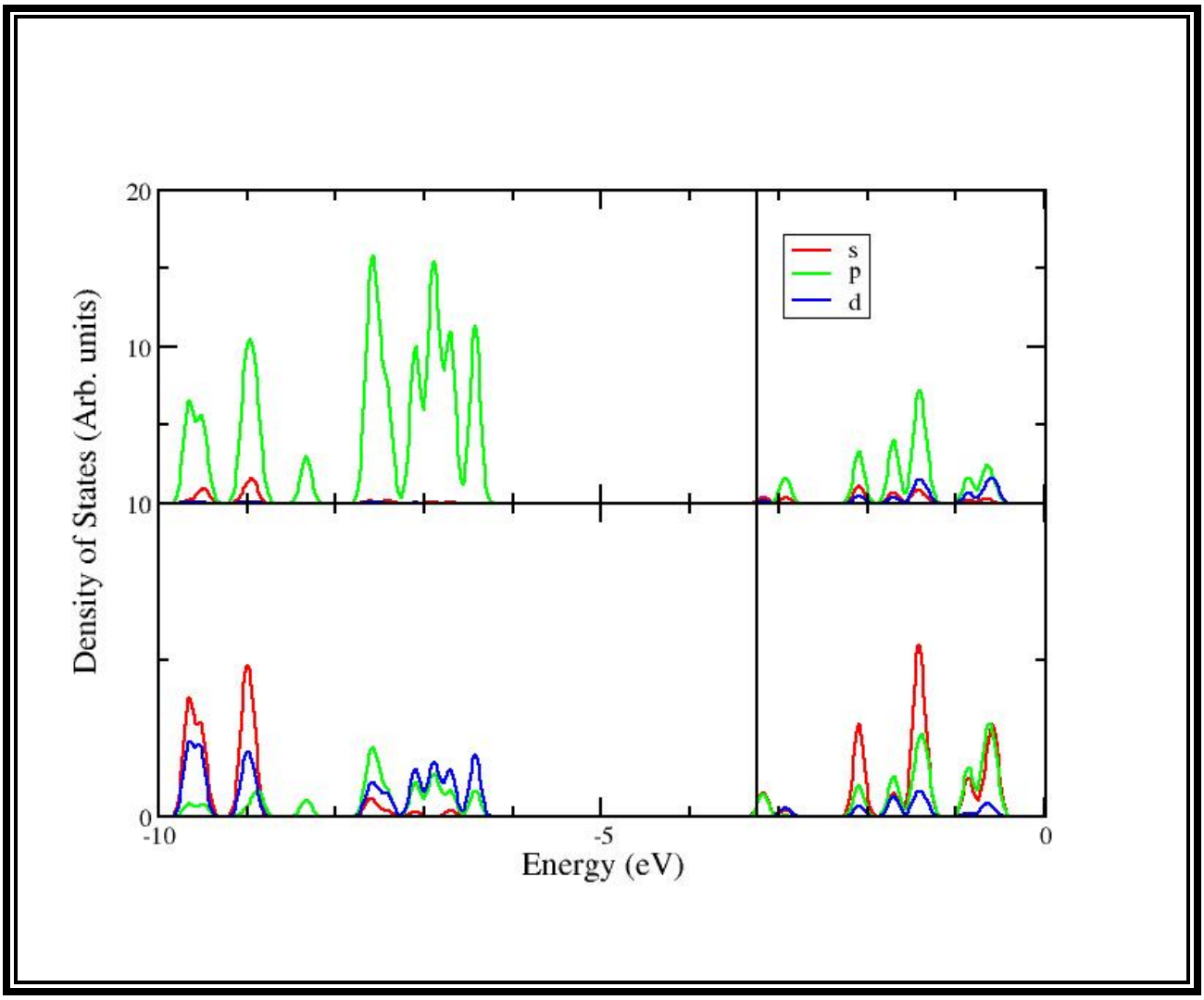

Figure 7.S8: The partial density of states of Zn12S12 cage

Summary and Conclusions

To summarize, the present study examines if the ZnS cages as observed in the classical molecular dynamics simulations are viable. Our DFT calculations using large polarized basis sets show that the hollow Zn_xS_x cages are chemically and energetically stable, and the vibrational analysis indicate that such hollow cage structures are local minima on the potential energy surface. The calculated HOMO-LUMO gaps are smaller than the bulk cubic form of ZnS being consistent with the expected quantum confinement effects on the cages. These cages have high

ionization potentials and relatively low electron affinities. The binding energies of these cages show a small variation in the range 5.49-5.63 eV with the trend that in general it increases with the cage size. The quasiparticle (transport) gaps vary from 6.15 eV in $Zn_{12}S_{12}$ to 3.9 eV in $Zn_{28}S_{28}$ with overall decrease in its value with increase in the cage size that is indicative of the quantum size effect. The analysis of partial charges show the ionic nature of bonding in these systems with an average of 1.3 e charge transfer from S to Zn atoms. Finally, we have also presented infrared spectra which may be useful in possible identification of these clusters in the experimental studies. The internal cavity of the studied cages with radius ranging from 3 to 12 Angstroms offer opportunities to host elements and small clusters with potential applications in catalysis, delivery of drugs, development of artificial cells, and protection of biologically active agents such as proteins, enzymes, or DNAs, and we hope that our work motivates future experimental studies.

References

[1] Yan Chai et al., "Fulleren with Metals Inside," *Journal of Physical Chemistry*, vol. 95, no. 20, pp. 7564-7568, 1991.

[2] Elkind J L, O'Brien S C et al. Weiss F D, "Photophysics of metal complexes of spheroidal carbon shells ," *J. Am. Chem. Soc.* , vol. 110, 1988.

[3] W. Kratschmer, L. D. Lamb, K. Fostiropoulos, and D.R. Huffman, *Nature*, 1990.

[4] Guo T, Jin C et al. Chai Y, "Fullerenes with metals inside ," *J. Phys. Chem.*, vol. 95, p. 7564, 1991.

[5] Gillan E G, Holczer K et al Alvarez M M, "La2C80: a soluble dimetallofullerene ," *J. Phys. Chem.* , vol. 95, p. 10561, 1991.

[6] Hansen K, Alvarez M M et al. Yeretzian C, "Collisional probes and possible structures of La2C80 ," *Chem. Phys. Lett.* , vol. 196, p. 337, 1992.

[7] Nelson H H, Callahan J H and McElvany S W Ross M M, "Production and characterization of metallofullerenes ," *J. Phys. Chem.* , vol. 96, p. 5231, 1992.

[8] McElvany S W, "Production of endohedral yttrium-fullerene cations by direct laser vaporization ," *J. Phys. Chem.* , vol. 96, p. 4935, 1992.

[9] Sato H, Ohchochi M et al. Shinohara H, "Encapsulation of a scandium trimer in C82 ," *Nature* , vol. 357 , p. 52, 1992.

[10] Nakane T and Shinohara H Xu Z, "Production and isolation of Ca@C82 (I-IV) and Ca@C82 (I, II) metallofullerenes ," *J. Am. Chem. Soc.* , vol. 118 , p. 11309, 1996.

[11] L. S. Wang et al., *Chem. Phys. Lett.* , vol. 1993, no. 207, p. 354.

[12] Y. Chai et al., *J. Phys. Chem. 1991, 95, 7564.*, vol. 95, p. 7564, 1991.

[13] D. S. Bethune, R. D. Johnson, J. R. Salem, M. S. Devries, and C. S. Yannoni, *Nature 1993, 366, 123.*, vol. 366, p. 123, 1993.

[14] H. Funasaka et al., "Preparation of Fullerene Derivatives by Resistive Heating With Graphite Crucible. In Taylor & Francis: 1993; Vol. 1, p 437.," in *In Taylor & Francis: 1993; Vol. 1, p 437.*, 1993, vol. 1, p. 437.

[15] K. Yoshie, S. Kasuya, K. Eguchi, and Yoshida, *T. Appl. Phys. Lett.* , vol. 61, p. 2782, 1992.

[16] Y., Rubin, "Ring opening reactions of fullerenes: Designed approaches to endohedral metal complexes. In Fullerenes and Related Structures; ," *Springer-Verlag Berlin*, vol. 199, p. 67, 1999.

[17] Conceicao J, Chibante L P F. et al. Haufler R E, "Efficient production of C60 (Buckminsterfullerene), CH60H36, and the solvated buckide ion," *J. Phys. Chem.* , vol. 94, p. 8634., 1990.

[18] Chai Y, Chibante L P F et al. Haufler R E, *Cluster-Assembled Materials,* J Bernhoc and D L Nelson eds R S Averback, Ed. Pittsburgh, PA: (Materials Research Society), , 1991, vol. 206,.

[19] Jin C, Hettich R L et al. Ying Z C, *Fullerenes: Recent Advances in the Chemistry and*

Physics of Fullerenes and Related Materials, eds K Kadish and R Ruoff, Ed. Pennington, , NJ: (Electrochemical Society), , 1994 , vol. 1,.

[20] Hinsanori Shinohara and Nikos Tagmatarchis, *ENDOHEDRAL METALLOFULLERENES*.: WILEY.

[21] Shinohara H, Saito Y et al. Bandow S, "High yield synthesis of lanthanofullerenes via lanthanum carbide ," *J. Phys. Chem.* , p. 97, 1993.

[22] Yokoyama S, Inakuma M and Shinohara H Saito Y, "An ESR study of the formation of La@C82 isomers in arc synthesis ," *Chem. Phys. Lett.*, vol. 250 , p. 80, 1996.

[23] S. Stevenson et al., *Nature* , vol. 401, p. 55, 1999.

[24] L. Dunsch, P. Georgi, M. Krause, and C. R. Wang, *Synth. Met.* , vol. 135, p. 761, 2003.

[25] Ohno M and Shinohara H Inakuma M, "Fullerenes: Recent Advances in the Chemistry and Physics of Fullerenes and Related Materials, eds (, NJ:)," *Electrochemical Society*, vol. 2, pp. 330–342, 1995.

[26] Funasaka H, Takahashi T and Akasaka T Yamamoto K, "Isolation of an ESR-active metallofullerene of La@C82 ," *J. Phys. Chem.* , vol. 98, p. 2008, 1994.

[27] Prato M and Wudl F Khemani K C, "A simple Soxhlet chromatographic method for the isolation of pure C60 and C70 ," *J. Organomet. Chem.* , vol. 57 , p. 3254, 1992.

[28] Y. Chai et al., *J. Phys. Chem.* , vol. 95, p. 7564, 1991.

[29] C. Yeretzian et al., *J. Phys. Chem. 1993, 97, 10097.*, vol. 97, p. 10097, 1993.

[30] T. Ogawa, T. Sugai, and H. J. Shinohara, *Am. Chem. Soc.* , vol. 122, p. 3538, 2000.

[31] H. Shinohara et al., *J. Phys. Chem.* , vol. 97, p. 4259, 1993.

[32] K. Jinno and Y. Saito, *Separation of fullerenes by liquid chromatography: Molecular recognition mechanisms in liquid chromatographic separation. In Advances in Chromatography; Marcel Dekker: New York*. New York, 1996, vol. 36.

[33] H. Shinohara, "Endohedral metallofullerenes," *Rep. Prog. Phys.*, vol. 63, p. 843, 2000.

[34] L. J. Wilson et al., *Chem. Rev.* , vol. 192, p. 199, 1999.

[35] P. Anilkumar et al., *Curr. Med. Chem.* , vol. 18, p. 2045, 2011.

[36] H. C. Dorn and P. P. Fatouros, *Nanosci. Nanotechnol. Lett.* , vol. 2, p. 65, 2010.

[37] E. B. Iezzi, J. C. Duchamp, K. R. Fletcher, T. E. Glass, and H. C. Dorn, *Nano Lett.* , vol. 2, p. 1187, 2002.

[38] J. X. Wang et al., *Biochem. Pharmacol.* , vol. 71, p. 872, 2006.

[39] L. Yan, F. Zhao, S. Li, Z. Hu, and Y. Zhao, *Nanoscale* , vol. 3, p. 362, 2011.

[40] R. B. Ross et al., *Nat. Mater.*, vol. 8, p. 208, 2009.

[41] M. Krause, F. Ziegs, A. A. Popov, and L. Dunsch, *Chem. Phys. Chem*, vol. 8, p. 537, 2007.

[42] S. Stevenson et al., *J. Am. Chem. Soc*, vol. 130, p. 11844, 2008.

[43] T. S. Wang et al., *J. Am. Chem. Soc.*, vol. 132, p. 16362, 2010.

[44] L, Dunsch et al., *J. Am. Chem. Soc.*, vol. 132, p. 5413, 2010.

[45] S. Stevenson et al., *Nature* , vol. 408, p. 427, 2000.

[46] C. R. Wang et al., *Nature* , vol. 408, p. 426, 2000.

[47] T. K. Zywietz, H. Jiao, R. Schleyer, and A. de Meijere, *J. Org. Chem.* , vol. 63, p. 3417,

1998.

[48] R. D. Johnson, M. S. Devries, J. Salem, D. S. Bethune, and C. S. Yannoni, *Nature* , vol. 355, p. 239, 1992.

[49] A. Rosen and B. Wastberg, *J. Am. Chem. Soc.* , vol. 110, p. 8701, 1988.

[50] Tao and Wang, Song and Lu, Xing and Tan, Yuanzhi and Huang, Jing and Liu, Fupin and Li, Qunxiang and Xie, Suyuan and Yang, Shangfeng Wei, "Entrapping a Group-VB Transition Metal, Vanadium, within an Endohedral Metallofullerene: VxSc3–xN

[51] S. Iijima, "Direct observation of the tetrahedral bonding in graphitized carbon black by high resolution electron microscopy," *J. Cryst. Growth*, vol. 50, no. 3, pp. 675-683, 1980.

[52] S. Iijima, *Nature* , vol. 354, pp. 56–58, 1991.

[53] S. Iijima and T. Ichihashi, *Nature* , vol. 363, , pp. 603–605, 1993,.

[54] K. S. Novoselov et al., *Science* , vol. 306, , pp. 666–669., 2004,.

[55] Shangfeng Yang, and Lothar, Dunsch Alexey A. Popov, "Endohedral Fullernes," *Chem. Rev.*, vol. 113, pp. 5989-6113, 2013.

[56] 2014, 5(1), 1980–1998. J. Bartelmess and S. Giordani, "Carbon nano-onions (multilayer fullerenes): chemistry and applications," *Beilstein J. Nanotechnol.*, vol. 5, no. 1, pp. 1980-1998, 2014.

[57] I. Puente-Lee, L. Rend´on-Vazquez P. Santiago, F. del Rio, D. Morales-Morales, et al., M. G. Crestani, "The catalytic reduction of carbon dioxide to carbon onion particles by platinum catalysts," *Carbon, 2005, 43(12), 2621–2624.*, vol. 43, no. 12, pp. 2621-2624, 2005.

[58] G. Yushin and Y. Gogotsi, C. Portet, "Electrochemical performance of carbon onions, nanodiamonds, carbon black and multiwalled nanotubes in electrical double layer capacitors," *Carbon*, vol. 45, no. 13, pp. 2511-2518, 2007.

[59] L. Borchardt, M. Oschatz, M. Bryjak, J. Atchison, K. Keesman, et al., S. Porada, "Direct prediction of the desalination performance of porous carbon electrodes for capacitive deionization," *Energy Environ. Sci.*, vol. 6, no. 12, pp. 3700-3712, 2013.

[60] M. Brunet, H. Durou, P. Huang, V. Mochalin, Y. Gogotsi, et al., D. Pech, "Ultrahigh-power micrometre-sized supercapacitors based on onion-like carbon, ," *Nat. Nanotechnol., 5(9),* , vol. 5, no. 9, pp. 651–654., 2010.

[61] Delano P. Chong, *Recent Advances in Density functional Methods*.: World Scientific Publishing Co. Pte. Ltd, 1995, vol. 1.

[62] Efthimions Kaxiras, *Atomic and Electronic Structure of Solids*.: Cambride University Press, 2003.

[63] J.C Slater, *Phys. Rev. B*, vol. 34, p. 1293, 1929.

[64] J. Kohanoff, *Electronic Structure Calculations for Solids and Molecules: Theory and Computational Methods*. Cambridge, UK: Cambridge University Press, 2006.

[65] R. M. Martin, *Electronic Structure*. U.K.: Cambridge University Press.

[66] K. Burke, M. Ernzerhof J.P. Perdew, *Phys. rev. Lett.*, vol. 77, p. 3865, 1996.

[67] M. R. Pederson and K. A. Jackson, "Variational Mesh for Quantum- Mechanical Simulations. ," *Phys. Rev. B: Condens. Matter Mater. Phys.* , vol. 41, p. 7453–7461., 1990.

[68] D. Porezag and M. R. Pederson, "Infrared Intensities and Raman- Scattering Activities Within Density-Functional Theory. ," *Phys. Rev. B: Condens. Matter Mater. Phys.* , vol. 54, p. 7830–7836., 1996.

[69] D. Porezag and M. R. Pederson, "Optimization of Gaussian Basis Sets for Density-Functional Calculations. ," *Phys. Rev. A: At., Mol., Opt. Phys.* , vol. 60, , p. 2840–2847., 1999.

[70] K. Jackson and M. R. Pederson, "Accurate Forces in a Local-Orbital Approach to the Local-Density Approximation. ," *Phys. Rev. B: Condens. Matter Mater. Phys.* , vol. 42, p. 3276–3281., 1990.

[71] J Furthmuller, G. Kresse, *Phy. Rev. B*, vol. 54, p. 11169, 1996.

[72] J. Furthmuller G. Kresse, *Comput. Mater. Sci*, vol. 6, p. 15, 1996.

[73] D. Joubert G. Kresse, *Phy. Rev. B*, vol. 59, p. 1778, 1999.

[74] P.E. Blochl, *Phys. Rev. B* , vol. 50, p. 17953 , (1994).

[75] R. Hirschl, M. Marsman, and G. Kresse, J. Paier, *J. Chem. Phys.*, vol. 122, , p. 234102 , (2005)..

[76] Santry DP, Segal GA Pople JA, *J Chem Phys* , vol. 43, pp. S129–S135, (1965).

[77] Thiel W Dewar MJS, *J Am Chem Soc*, vol. 99, pp. 4907–4917, (1977).

[78] Zoebisch EG, Healy EF, Stewart JJP Dewar MJS, *J Am Chem Soc* , vol. 107:, pp. 3902–3909, 1985.

[79] Stewart JJP, *J Comp Chem* , vol. 10, pp. 209–220, 1989.

[80] James J. P. Stewart, "Optimization of parameters for semiempirical methods V: Modification of NDDO approximations and application to 70 elements," *Journal of Molecular Modeling* , vol. 13, pp. 1173-1213, 2007.

[81] G. 36. Brinkmann and B. D. McKay, "Fast Generation of Planar GraphsMATCH ," *Commun. Math. Comput. Chem.* , vol. 58, , pp. 323–357 , 2007,.

[82] G. Brinkmann et al., "Generation of Simple Quadrangulations of the Sphere," *Discrete mathematics* , vol. 305, , pp. 33–5410, 2005.

[83] J. J. P. Stewart, "Optimization of Parameters for Semiempirical Methods V: Modification of NDDO Approximations and Application to 70 Elements," *J. Mol. Model.* , pp. 1173–121310, 2007, 13,.

[84] J. P. Perdew, K. Burke, and M. Ernzerhof, "Generalized Gradient Approximation Made Simple," *Phys. Rev. Lett.* , vol. 77, , pp. 3865–3868, 1996,.

[85] Y. et al. Chai, "Fullerenes with metals inside. ," *J. Phys. Chem.* , vol. 95, pp. 7564–7568 , (1991).

[86] W., Lamb, L. D., Fostiropoulos, K. & Huffman, D. R. Krätschmer, "Solid C60: a new form of carbon. ," *Nature* , vol. 347, pp. 354–358, (1990).

[87] G. Rice, T. Glass, K. Harlch, F. Cromer, M. R. Jordan, J. Craft, E. Hadju, R. Bible, M. M. Olmstead, K. Maltra, A. J. Fisher, A. L. Balch, H. C. Dorn. S. Stevenson, "Small-bandgap endohedral metallofullerenes in high yield and purity. ," *Nature* , vol. 401, p. 55, (1999)..

[88] L. S. et al. Wang, "The electronic structure of Ca@C60. ," *Chem. Phys. Lett.* , vol. 207, pp. 354–359, (1993)..

[89] D. S., Johnson, R. D., Salem, J. R., de Vries, M. S. & Yannoni, C. S. Bethune, "Atoms in carbon cages: the structure and properties of endohedral fullerenes. ," *Nature* , vol. 366, pp. 123–128, (1993).

[90] S. Kasuya, K. Eguchi, and Yoshida. K. Yoshie, "Novel method for C60 synthesis: A thermal plasma at atmospheric pressure. ," *T. Appl. Phys. Lett.* , vol. 61, p. 2782, (1992).

[91] Y. Rubin, *Ring Opening Reactions of Fullerenes: Designed Approaches to Endohedral Metal Complexes. Topics in Current Chemistry*., (1999).

[92] P. Georgi, M. Krause, and C. R. Wang. L. Dunsch, "New clusters in endohedral fullerenes: the metalnitrides," *Synth. Met.* , vol. 135, p. 761, (2003)..

[93] L. et al. J. Wilson, "Metallofullerene drug design. ," *Coord. Chem. Rev.* , pp. 190-192, 199–207, (1999)..

[94] Lu F, Cao L, Luo PG, Liu JH, Sahu S, Tackett KN, Wang Y, Sun YP. Anilkumar P1, "Fullerenes for applications in biology and medicine. ," *Curr. Med. Chem.* , vol. 18, p. 2045, (2011).

[95] H. C. & Fatouros, P. P. Dorn, "Endohedral Metallofullerenes: Applications of a New Class of Carbonaceous Nanomaterials. ," *Nanosci. Nanotechnol. Lett.* , vol. 2, pp. 65–72, (2010)..

[96] H. Shinohara, "Endohedral metallofullerenes. ," *Rep. Prog. Phys.* , vol. 63, pp. 843–892, (2000)..

[97] E. B., Duchamp, J. C., Fletcher, K. R., Glass, T. E. & Dorn, H. C. Iezzi, "Lutetium-based Trimetallic Nitride Endohedral Metallofullerenes: New Contrast Agents. ," *Nano Lett.* , vol. 2, pp. 1187–1190, (2002)..

[98] C Chen, B Li, H Yu, Y Zhao, J Sun, Y Li. J Wang, "Antioxidative function and biodistribution of [Gd@ C 82 (OH) 22] n nanoparticles in tumor-bearing mice. ," *Biochem. Pharmacol.* , vol. 71, , p. 872, (2006)..

[99] L., Zhao, F., Li, S., Hu, Z. & Zhao, Y. Yan, "Low-toxic and safe nanomaterials by surface-chemical design, carbon nanotubes, fullerenes, metallofullerenes, and graphenes. ," *Nanoscale* , vol. 3, pp. 362–382 , (2011)..

[100] R. B. et al. Ross, "Endohedral fullerenes for organic photovoltaic devices. ," *Nat. Mater.* , vol. 8, , pp. 208–212, (2009)..

[101] S. et al. Stevenson, "Materials science: A stable non-classical metallofullerene family. ," *Nature* , vol. 408, , p. 427, (2000)..

[102] C.-R., Sugai, T., Kai, T., Tomiyama, T. & Shinohara, H. Wang, "Production and isolation of an ellipsoidal C80 fullerene. ," *Chem. Commun.* , pp. 557–558, (2000)..

[103] S. S., Liu, D. & Hagelberg, F. Park, "Comparative Investigation on Non-IPR C68and IPR C78Fullerenes Encaging Sc3N Molecules. ," *J. Phys. Chem. A* , vol. 109, pp. 8865–8873, (2005).

[104] T. et al. Wei, "Entrapping a Group-VB Transition Metal, Vanadium, within an Endohedral Metallofullerene: V(x)Sc(3-x)N@I(h)-C80 (x = 1, 2). ," *J. Am. Chem. Soc.* , vol. 138, pp. 207–214 , (2016)..

[105] Rajendra R. Zope, Surendra Bhatta, and Tunna Baruah. Shusil Bhusal, "Electronic and Optical Properties of VSc2N@C68 Fullerene. ," *J. Phys. Chem. C* , vol. 120, p. 27813, (2016)..

[106] G., Goedgebeur, J. & McKay, B. D. Brinkmann, "The generation of fullerenes.," *J. Chem. Inf. Model.* , vol. 52, pp. 2910–2918, (2012)..

[107] J. J. P. Stewart, "'Optimization of Parameters for Semiempirical Methods V: Modification of NDDO Approximations and Application to 70 Elements.,'," *J. Mol. Model.*, vol. 13, p. 1173–1213, 2007.

[108] M. R. & Jackson, K. A. Pederson, "Variational mesh for quantum-mechanical simulations. ," *Phys. Rev. B: Condens. Matter Mater. Phys.* , vol. 41, pp. 7453–7461, (1990).

[109] K. & Pederson, M. R. Jackson, "Accurate forces in a local-orbital approach to the local-density approximation. ," *Phys. Rev. B: Condens. Matter Mater. Phys.* , vol. 42, pp. 3276–3281, (1990).

[110] D. & Pederson, M. R. Porezag, "Infrared intensities and Raman-scattering activities within density-functional theory. ," *Phys. Rev. B: Condens. Matter Mater. Phys.* , vol. 54, pp. 7830–7836, (1996)..

[111] D. & Pederson, M. R. Porezag, "Optimization of Gaussian basis sets for density-functional calculations. ," *Phys. Rev. A* , vol. 60, pp. 2840–2847, (1999)..

[112] T. A. & Limas, N. G. Manz, "Introducing DDEC6 atomic population analysis: part 1. Charge partitioning theory and methodology. ," *RSC Adv.* , vol. 6, , pp. 47771–47801, (2016).

[113] N. G. & Manz, T. A. Limas, "Introducing DDEC6 atomic population analysis: part 2. Computed results for a wide range of periodic and nonperiodic materials. ," *RSC Adv.* , vol. 6, pp. 45727–45747, (2016)..

[114] M. & Dunsch, L. Krause, "Gadolinium Nitride Gd3N in Carbon Cages: The Influence of Cluster Size and Bond Strength. ," *Angew. Chem. Int. Ed.* , vol. 44, pp. 1557–1560, (2005).

[115] S. & Dunsch, L. Yang, "A Large Family of Dysprosium-based Trimetallic Nitride Endohedral Fullerenes: Dy3N@C2n(39 ≤n≤ 44). ," *J. Phys. Chem. B* , vol. 109, pp. 12320–12328, (2005)..

[116] M. et al. Wolf, "Magnetic Moments of the Endohedral Cluster Fullerenes Ho3N@C80 and Tb3N@C80: The Role of Ligand Fields. ," *Angew. Chem. Int. Ed.* , vol. 44, pp. 3306–3309, (2005).

[117] O. M. M. de Bettencourt-Dias A. Duchamp J.C. Stevenson S. Dorn H.C. and Balch A.L., "Isolation and Crystallographic Characterization of ErSc2N@C80: an Endohedral Fullerene Which Crystallizes with Remarkable Internal Order.," *J. Am. Chem. Soc.* , vol. 122, p. 12220, (2000).

[118] X. et al. Wang, "Preparation and structure of CeSc2N@C80: an icosahedral carbon cage enclosing an acentric CeSc2N unit with buried f electron spin. ," *J. Am. Chem. Soc.* , vol. 128, pp. 8884–8889, (2006)..

[119] Alexey A. and Yang, Shangfeng and Dunsch, Lothar. Popov, "Endohedral Fullerenes. ," *Chem. Rev.* , vol. 113, pp. 5989–6113, (2013).

[120] S., Lee, H.M., Olmstead, M.M., Kozikowski, C., Stevenson, P. and Balch, A.L. Stevenson, "Preparation and Crystallographic Characterization of a New Endohedral, Lu3N@ C80· 5 (o-xylene), and Comparison with Sc3N@ C80· 5 (o-xylene).," *Chemistry-A European Journal,* , vol. 8, no. (19), pp. 4528-4535, (2002)..

[121] R. D. Shannon, "Revised effective ionic radii and systematic studies of interatomic

distances in halides and chalcogenides. ," *Acta Crystallogr. A* , , vol. A32, p. 751 , (1976).

[122] A. A., Chen, C., Yang, S., Lipps, F. & Dunsch, L. Popov, "Spin-Flow Vibrational Spectroscopy of Molecules with Flexible Spin Density: Electrochemistry, ESR, Cluster and Spin Dynamics, and Bonding in TiSc2N@C80. ," *ACS Nano* , vol. 4, pp. 4857–4871, (2010)..

[123] L., Amerikheirabadi, F., Zope, R. & Baruah, T. Basurto, "The electronic structure and charge transfer excited states of the endohedral trimetallic nitride C80(Ih) fullerenes–Zn-tetraphenyl porphyrin dyads. ," *Phys. Chem. Chem. Phys.* , vol. 17, pp. 5832–5839, (2015)..

[124] A. & Waestberg, B. Rosen, "First-principle calculations of the ionization potentials and electron affinities of the spheroidal molecules carbon (C60) and lanthanum carbude (LaC60). ," *J. Am. Chem. Soc.* , vol. 110, pp. 8701–8703, (1988)..

[125] A. H. An Atlas of Fullerenes By P. W. Fowler (University of Exeter), D. E. Manolopoulos (University of Nottingham). Oxford: New York. 1995. viii 392 pp. $98.00. ISBN 0-19-855787-6. Francis, *J. Am. Chem. Soc.* , vol. 118, pp. 5161–5161 , (1996)..

[126] A. A. & Dunsch, L. Popov, "Structure, stability, and cluster-cage interactions in nitride clusterfullerenes M3N@C2n (M = Sc, Y; 2n = 68-98): a density functional theory study. ," *J. Am. Chem. Soc.* , vol. 129, , pp. 11835–11849, (2007)..

[127] S., Popov, A.A. and Dunsch, L. Yang, "Violating the Isolated Pentagon Rule (IPR): The Endohedral Non-IPR C70 Cage of Sc3N@C70. ," *Angew. Chem. Int. Ed.* , vol. 46., p. 1256, (2007)..

[128] M. R., Li, F.-F. & Echegoyen, L. A. Cerón, "Endohedral fullerenes: the importance of electronic, size and shape complementarity between the carbon cages and the corresponding encapsulated clusters. ," *J. Phys. Org. Chem.* , vol. 27, pp. 258–264.

[129] S., Popov, A. A. & Dunsch, L. Yang, "Violating the Isolated Pentagon Rule (IPR): The Endohedral Non-IPR C70 Cage of Sc3N@C70. ," *Angew. Chem. Int. Ed.* , vol. 46, pp. 1256–1259, (2007)..

[130] W.-W. Wang, T. Yang, and S. Nagase, H. Zheng. X. Zhao, "'Sc2@C70 rather than Sc2C2@C68: Density functional theory characterization of metallofullerene Sc2C70,'. ," *J. Chem. Phys.* , vol. 137, pp. 014308, (2012)..

[131] and Lothar Dunsch, Shangfeng Yang. ' Alexey A. Popov, "The Role of an Asymmetric Nitride Cluster on a Fullerene Cage: The Non-IPR Endohedral DySc2N@C76,'. ," *American Chemical Society,* , vol. 111, pp. 13659–13663, (2007.)..

[132] T. et al. Yang, "Sc2O@Td(19151)-C76: Hindered Cluster Motion inside a Tetrahedral Carbon Cage Probed by Crystallographic and Computational Studies. ," *Chemistry - A European Journal* , vol. 21, pp. 11110–11117, (2015)..

[133] P. et al. Zhao, "Dimetallic sulfide endohedral metallofullerene Sc2S@C76: density functional theory characterization. ," *J. Comput. Chem.* , vol. 35, pp. 1657–1663, (2014)..

[134] M. M. et al. Olmstead, "Sc3N@C68: Folded Pentalene Coordination in an Endohedral Fullerene that Does Not Obey the Isolated Pentagon Rule. ," *Angew. Chem. Int. Ed.* , vol. 42, pp. 900–903, (2003).

[135] B. et al. Isolation, characterization, and theoretical study of La2@C78. Cao, *J. Am. Chem. Soc.* , vol. 126, pp. 9164–9165, (2004)..

[136] T., Sato, Y., Suenaga, K. & Iijima, S. Yumura, "Which do endohedral Ti2C80 metallofullerenes prefer energetically: Ti2@C80 or Ti2C2@C78? A theoretical study.," *J. Phys. Chem. B* , vol. 109, pp. 20251–20255, (2005)..

[137] M., Wong, J. and Dunsch, L. Krause, "Expanding the World of Endohedral Fullerenes—The Tm3N@ C2n (39≤ n≤ 43) Clusterfullerene Family. ," *Chemistry-A European Journal,* , vol. 11, , pp. 706–711. , (2005.)..

[138] F.-F. et al. Li, "Ti2S@D3h(24109)-C78: a sulfide cluster metallofullerene containing only transition metals inside the cage. ," *Chem. Sci.* , vol. 4, p. 3404, (2013)..

[139] O. M. M. de Bettencourt-Dias A. Duchamp J.C. Stevenson S. Marciu D. Dorn H.C. and Balch A.L., "Isolation and structural characterization of the endohedral fullerene Sc3N@ C78. ," *Angew. Chem. Int. Ed.* , vol. 40, , pp. 1223–1225., (2001)..

[140] T., Xu, L., Gibson, H.W., Dorn, H.C., Chancellor, C.J., Olmstead, M.M. and Balch, A.L. Cai, "Sc3N@ C78: Encapsulated cluster regiocontrol of adduct docking on an ellipsoidal metallofullerene sphere. ," *J. Am. Chem. Soc.* , vol. 129, pp. 10795–10800., 2007.

[141] P., Zhou, Z., Hao, C., Gao, Z., Tan, K., Lu, X. and Chen, Z. Jin, "NC unit trapped by fullerenes: a density functional theory study on Sc 3 NC@ C 2n (2 n= 68, 78 and 80). ," *Phys. Chem. Chem. Phys.* , vol. 12, pp. 12442–12449., 2010.

[142] J. R. Heath et al., *J. Am. Chem. Soc.*, vol. 107, p. 7779, 1985.

[143] R. Tellgmann, N. Krawea, S.-H. Lin, I.V. Hertel, and E.E.B. Campbell, *Nature*, vol. 382, p. 407, 1996.

[144] R. Tellgmann, N. Krawez, I.V. Hertel, and E.E.B. Campbell, *Fullerenes and Fullerene Nanostructure*. London: World Scientific, 1996.

[145] E.E.B. Campbell, R. Tellgmann, N. Krawez, and I.V. Hertez, *J. Phys. Chem. Solids*, vol. 58, p. 1763, 1997.

[146] Y. F. Lian, Z. J. Shi, X. H. Zhou, and Z. N. Gu, *Chem. Mater.* , vol. 16, , p. 1704., 2004.

[147] A. A. Popov, L. Zhang, and L. Dunsch, *ACS Nano* , vol. 4, p. 795., 2010.

[148] N. Tagmatarchis, E. Aslanis, K. Prassides, and H. Shinohara, *Chem. Mater.* , vol. 13, p. 2374., 2001.

[149] S. F. Yang and L. Dunsch, *Angew. Chem.-Int. Edit.* , vol. 45, p. 1299., 2006.

[150] J. Wong and L. Dunsch M. Krause, *Chem.-Eur. J.,* vol. 11, p. 706, 2005.

[151] S. F. Yang, M. Kalbac, A. Popov, and L. Dunsch, *ChemPHysChem*, vol. 7, p. 1990, 2006.

[152] M. M. Alvarez et al., *J. Phys. Chem.* , vol. 95, p. 10561., 1991.

[153] M. Yamada, N. Mizorogi, T. Tsuchiya, T. Akasaka, and S. Nagase, *Chem.□Eur. J.* , vol. 15, , p. 9486., 2009,.

[154] R.D. Johnson, M. S. Devries, J. Salem, D. S. Bethune, and C.S. Yannoni, *Nature*, vol. 355, p. 239, 1992.

[155] M. Krause and L. Dunsch, *Angew. Chem*, vol. 44, p. 1557, 2005.

[156] S.F. Yang and L. Dunsch, *J. Phys. Chem. B*, vol. 109, p. 12320, 2005.

[157] S. Stevenson et al., *Nature*, vol. 401, p. 55, 1999.

[158] Yang. S. et al., *Chem. Commun*, pp. 6391-6393, 2009.

[159] N. Chen et al., *J. Phys. Chem. C*, vol. 111, pp. 11823-11828, 2007.

[160] X. L. Wang et al., *J. Am. Chem. Soc.*, vol. 128, pp. 8884-8889, 2006.

[161] S. Yang, A. A. Popov, C. chen, and L. Dunsch, *J. Phys. Chem. C*, vol. 113, pp. 7616-7623, 2009.

[162] S. Yang, A. A. Popov, and L. Dunsch, *J. Phys. Chem. B* , vol. 111, p. 13659., 2007.

[163] S. F. Yang, A. A. Popov, and L. Dunsch, *Chem. Commun.* , p. 2885., 2008.

[164] S.F. Yang et al., *Chem. Commun.*, p. 6391, 2009.

[165] Shangfeng Yang and Lothar Dunsch Alexey A. Popov, "Endohedral Fullerenes," *Chem. Rev*, vol. 113, no. 8, pp. 6008-6014, 2013.

[166] J. J. P. Stewart, "Optimization of Parameters for Semiempirical Methods V: Modification of NDDO Approximations and Application to 70 Elements.," *J. Mol. Model.*, vol. 13, p. 1173–1213., 2007.

[167] J. P. Perdew, K. Burke, and M. Ernzerhof, "Generalized Gradient Approximation Made Simple.," *Phys. Rev. Lett.*, vol. 77, p. 3865–3868., 1996.

[168] T. A. & Limas, N. G. I Manz, "ntroducing DDEC6 atomic population analysis: part 1. Charge partitioning theory and methodology. ," *RSC Adv.* , vol. 6, pp. 47771–47801, (2016)..

[169] N. G. & Manz, T. A. Limas, "Introducing DDEC6 atomic population analysis: part 2. Computed results for a wide range of periodic and nonperiodic materials. ," *RSC Adv.* , vol. 6, pp. 45727–45747, (2016)..

[170] S. F. Yang, A. A. Popov, M. Kalbac, and L. Dunsch, *Chem.-Eur. J.*, vol. 14, p. 2084, 2008.

[171] S. Yang, A.A. Popov, C. Chen, and L. Dunsch, *J. Phys. Chem. C*, vol. 113, p. 7616, 2009.

[172] Y. Zhang, A. A. Popov, S. Schiemenz, and L Dunsch, *Chem.-Eur. J.*, vol. 18, p. 9691, 2012.

[173] Alexey A. Popov* and Lothar Dunsch, "Structure, Stability, and Cluster-Cage Interactions in Nitride Clusterfullerenes M3N@C2n (M = Sc, Y; 2n = 68–98): a Density Functional Theory Study," *Journal of the American Chemical Society* , vol. 129 , no. 38, pp. 11835-11849, 2007.

[174] Alexey A. Popov, and Lothar Dunsch, Shangfeng Yang, "The Role of an Asymmetric Nitride Cluster on a Fullerene Cage: The Non-IPR Endohedral DySc2N@C76," *American Chemical Society*, vol. 111, no. 13659-13663, 2007.

[175] Yajuan and Feng, Lai and Xu, Wei and Gu, Zhenggen and Hu, Ziqi and Shi, Zujin and Slanina, Zdeněk and Uhlík, Filip Author Hao, "Sm\char64C2v(19138)-C76: A Non-IPR Cage Stabilized by a Divalent Metal Ion," *Journal Inorganic Chemistry* , vol. 54, pp. 4243-4248 , 2015.

[176] M. H. Olmstead et al., "Isolation and Structural Characterization of the Endohedral Fullerenes Sc3N@C78," *Angew. Chem.*, vol. 40, pp. 1223-1225, 2001.

[177] M. Krause, J. Wong, and L. Dunsch, "Expanding the world of endohedral fullerenes--the Tm3N@C2n (39< or =n< or =43) clusterfullerene family.," *Chem. Eur. J.*, vol. 11, pp. 706-711., 2005.

[178] S. F. Yang and L. Dunsch, "A large family of dysprosium-based trimetallic nitride endohedral fullerenes: Dy3N@C2n (39

[180] FW., Xu, HL. & Su, ZM. (2016) 22: 174. doi:10.1007/s00894-016-3040-y Gao, "The

inner-induced effects of YCN in C76 on the structures and nonlinear optical properties," *J Mol Model* , vol. 22, p. 174, 2016.

[181] F. Diederich et al., *Science 1991, 254, 1768*., vol. 254, p. 1768, 1991.

[182] K. Kikuchi et al., *Nature* , vol. 357, p. 142, 1992.

[183] R. Taylor, G. J. Langley, T. J. S. Dennis, H. W. Kroto, and D. R. M. Walton, *J. Chem. Soc., Chem. Commun.* , vol. 1043, 1992.

[184] Ugarte, "Curling and closure of graphitic networks under electon-beam irradiation," *Nature*, vol. 359, no. 6397, pp. 707-709, 1992.

[185] X. G. Liu, D. J. Fu, P. D. Han and B. S. Xu A. B. Du, "Onion-like fullerenes sysnthesis from coal," *Fuel*, vol. 86, pp. 294-298, 2007.

[186] T. Füller, P. Redlich and P. Ajayan F. Banhart, "The formation, annealing and self-compression of carbon onions under electron irradiation," *Chem. Phys. Lett.* , vol. 269, no. 3, pp. 349–355, 1997.

[187] C. Labrugère, M. Trinquecoste, P. Chadeyron and P. Delhaès. B. Maquin, A. Derré, ""Submicronic powders containing carbon, boron and nitrogen: their preparation by chemical vapour deposition and their characterization," ," *Carbon, ,* vol. 38, pp. 145-156, 2000.

[188] "Highly curved carbon nanostructures produced by ball-milling," H. Yasuda and H. Mori J. Huang, *Chem. Phys. Lett.,* , vol. 303, pp. 130-134, 1999.

[189] S. Usuba, H. Yokoi, Y. Kakudate and O. Odawara A. V. Gubarevich, J. Kitamura, ""Onion-like carbon deposition by plasma spraying of nanodiamonds," ," *Carbon,* , vol. 41, pp. 2601-2606, , 2003.

[190] M. Sioda, A. Huczko, Y. Zhu, H. Kroto and D. Walton H. Lange, "Nanocarbon production by arc discharge in water," *Carbon*, vol. 41, no. 8, pp. 1617-1623, 2003.

[191] V.Z. Mordkovich, "The Observation of Large Concentric Shell Fullerenes and Fullerene-Like Nanoparticles in Laser Pyrolysis Carbon Blacks.," *Chem. Mater. 2000, 12, 2813-2818*., vol. 12, pp. 2813-2818, 2000.

[192] Rajendra R Zope., "Electronic structure and static dipole polarizability of C60@C240; ," *J. Phys. B: Mol Opt. Phys.* , vol. 41, 2008.

[193] Shusil Bhusal, Luis Basurto, Tunna Baruah, and Koblar Jackson Rajendra R. Zope, "Site specific atomic polarizabilities in endohedral fullerenes and carbon onions," *The Journal of Chemical Physics* , vol. 143, p. 084306 , (2015).

[194] Alessandro Bagno and Giacomo Saielli, Girolamo Casella, "Spectroscopic signatrues of the carbon buckyonions C60@C180 and C60@C240: a dispersion-corrected DFT study. ," *Phys. Chem. Chem. Phys.,* , vol. 15, p. 18030, 2013.

[195] and Miquel Sola Alexander A. Voityuk, "Photoinduced Charge Separation in the Carbon Nano-Onion C60@C240," *J. Phys. Chem A*, vol. 120, no. 29, pp. 5798-5804, 2016.

[196] " Diffuse interstellar bands in fullerene planetary nebulae: the fullerenes – diffuse interstellar bands connection," *Astronomy & Astrophysics Letter to the Editor*, 2013.

[197] D. Muigg, P. Scheier, K. Becker, and T.D., Mark, "Measured appearance energies of Cn+ ($3 \leq n \leq 10$) fragment ions produced by electron impact on C60, ," *J. Phys. B:,* , vol. 29, , p. 5193., 1996,.

[198] X.B. Wang, C.F. Ding, and L.S., Wang, "High resolution photoelectron spectroscopy of C-60(-), ," *J. Chem. Phys.,* , vol. 110, no. 17, pp. 8217-8220., 1999.

[199] John P. Perdew, "Density functional theory and the band gap problem," *Internation journal of quantum chemistry*, 1985.

[200] L. Brus, "Quantum crystallites and nonlinear optics," *Appl. Phys. A* , vol. 53, p. 465., 1991.

[201] W. Yu, P. F. Fang, and S. J. Wang, "ZnS nanorod arrays synthesized by an aqua-solution hydrothermal process upon pulse-plating Zn nanocrystallines," *Appl. Surf. Sci.*, vol. 255, pp. 5709–5713., 2009.

[202] L.W. Yin, Y. Bando, J.H. Zhan, M.S. Li, and D. Golberg, "Self-assembled highly faceted wurtzite-type ZnS single-crystalline nanotubes with hexagonal cross-sections," *Adv. Mater.*, vol. 17, pp. 1972–1976., 2005.

[203] J. Y. Li, Q. Zhang, L. An, L.C. Qin, and J. Liu, "Large-scale growth of millimeter-long single-crystalline ZnS nanobelts," *J. Solid State Chem.*, vol. 181, pp. 3116–3120., 2008.

[204] Y. Liu et al., "Triethylenetetramine (TETA)-assisted synthesis, dynamic growth mechanism, and photoluminescence properties of radial single-crystalline ZnS nanowire bundles," *J. Cryst. Growth*, vol. 311, pp. 1423–1429., 2009.

[205] S. Biswas, T. Ghoshal, S. Kar, S. Chakrabarti, and S. Chaudhuri, "ZnS nanowire arrays: synthesis, optical and field emission properties, ," *Cryst. Growth Design* , vol. 8, pp. 2171–2176. , 2008.

[206] C. Wang et al., "A simple method for large-scale preparation of ZnS nanoribbon film and its photocatalytic activity for dye degradation, ," *App. Surf. Sci.* , vol. 256, pp. 4125-4128. , 2010.

[207] S.-H. Yu and M. Yoshimura, "Shape and Phase Control of ZnS Nanocrystals: Template Fabrication of Wurtzite ZnS Single-Crystal Nanosheets and ZnO Flake-like Dendrites from a Lamellar Molecular Precursor ZnS·(NH2CH2CH2NH2)0.5.," *Adv. Mater.,* vol. 14, pp. 296–300., 2002.

[208] C., Introduction to Solid State Physics, Kittel,. New York: John Wiley, , 1986, , vol. 6th Ed.,.

[209] J. C. Bao, Y. Y. Liang, Z. Xu, and L. Si, "Facile synthesis of hollow nickel submicrometer spheres. ," *Adv. Mat.* , vol. 15, pp. 1832-1835. , 2003.

[210] M. Jafelicci, M. R. Davolos, F. J. Santos, and S. J. Andrade, "Hollow silica particles from microemulsion. ," *J. Non-Cryst. Solids* , vol. 247, , pp. 98-102. , 1999.

[211] A. Bourlinos, N. Boukos, and D. Petridis, "Exchange resins in shape fabrication of hollow inorganic and carbonaceous-inorganic composite spheres. ," *Adv. Mater.* , vol. 14, pp. 21-24. , 2002.

[212] Y. Hosokawa, T. Kawasea, and M. Oda, "8,16,24,32,40,48-Hexamethoxy[2.6]metacyclophane-1,9,17,25,33,41-hexayne: a novel near-planar ammonium-selective ionophore. ," *Chem. Commun.* , vol. 17, pp. 1948-1949. , 2001.

[213] L. H. Dong, Y. Chu, F. Y. Yang, Y. Liu, and J. L. Liu, "Fabrication and characterization of ZnS hollow nanostructures in micelle system. ," *Chem. Lett.* , vol. 34, , pp. 1254-1255. , 2005.

[214] Y. He, "A novel emulsifier-free emulsion route to synthesize ZnS hollow microspheres. ," *Mat. Research Bull.* , vol. 40, , pp. 629-634. , 2005,.

[215] X. Liu et al., "A solvothermal route to semiconductor ZnS micrometer hollow spheres with strong photoluminescence properties. ," *Mat. Letters* , vol. 60, no. (20), pp. 2465-2469. , 2006.

[216] S. K. Panda and S. Chaudhuri, "Chelating ligand-mediated synthesis of hollow ZnS microspheres and its optical properties.," *J. Colloid and Interface Sci.* , vol. 313, no. (1), pp. 338-344. , 2007.

[217] L. H. Dong, Y. Chu, Y. P. Zhang, Y. Liu, and F. Y. Yang, "Surfactant-assistant and facile synthesis of hollow ZnS nanospheres. ," *J. Colloid and Interface Sci.* , vol. 308, no. (1), pp. 258-264. , 2007.

[218] X-L. Yu, H-M. Ji, H.L. Wang, J. Sun, and X-M. Du, "Synthesis and Sensing Properties of ZnO/ZnS Nanocages. ," *Nanoscale Res Lett.* , vol. 5, no. (3), , pp. 644–648. , 2010.

[219] D. Wang, H. Zhang, L. Li, M. Chen, and X. Liu, "Laser-ablation-induced synthesis of porous ZnS/Zn nano-cages and their visible-light-driven photocatalytic reduction of aqueous Cr(VI). ," *Opt. Mater. Express* , vol. 6, , no. , pp. 1306-1312. , 2016.

[220] P. Jena and A.W. Jr. Castleman, "Clusters: A bridge across the disciplines of physics and chemistry.," *Proc Natl Acad Sci U S A* , vol. 103, no. (28), pp. 10560–10569. , 2006.

[221] J. U. Reveles et al., "Designer magnetic superatoms. ," *Nat. Chem.* , vol. 1, , pp. 310-315. , 2009,.

[222] C. S. Tiwary, P. Kumbhakar, A. K. Mondal, and A. K. Mitra, "Synthesis and enhanced green photoluminescence emission from BCT ZnS nanocrystals ," *Phys Status Solidi A* , vol. 207, , p. 1874. , 2010,.

[223] S. B. Qadri et al., "Size-induced transition-temperature reduction in nanoparticles of ZnS ," *Phys Rev B* , vol. 60, p. 9191. , 1999.

[224] A. D. Dinsmore et al., "Structure and luminescence of annealed nanoparticles of ZnS:Mn," *J. Appl. Phys.* , vol. 88, , p. 4985. , 2000,.

[225] D. Son et al., "Synthesis and photoluminescence of Mn-doped zinc sulfide nanoparticles ," *Appl. Phys. Lett.* , vol. 90, , p. 101910. , 2007,.

[226] C. Feigl, S. P. Russo, and A. S. Barnard, "Safe, stable and effective nanotechnology: Phase mapping of ZnS nanoparticles, ," *J. Mater. Chem.* , vol. 20, , pp. 4971-4980. , 2010,.

[227] A. K. Kole and P. Kumbhakar, "Cubic-to-hexagonal phase transition and optical properties of chemically synthesized ZnS nanocrystals, ," *Results in Phys.*, vol. 2, , pp. 150-155. , 2012,.

[228] Springborg, M. Editor, In Chemical Modelling,.: RSC Publishing, , 2012, vol. 9.

[229] J. M. Matxain, A. Irigoras, J. E. Fowler, and J.M. Ugalde, "Small clusters of group-(II-VI) materials: ZniXi, X=Se,Te, i=1-9.," *Phys. Rev. A*, vol. 64, p. 053201., 2001.

[230] P. Deglmann, A. Reinhart, and T. Kakha, "Theoretical studies of ligand-free cadmium selenide and related semiconductor clusters. ," *J. Chem. Phys.* , vol. 116, , pp. 1585-1597. , 2002,.

[231] M. Khalkhali, Q. Liu, H. Zeng, and H. Zhang, *Sci. Reports* , vol. 5, , p. 14267. , 2015,.

[232] E. Spano, S. Hamad, and C. R. A. Catlow, "Computational evidence of bubble ZnS clusters. ," *J. Phys. Chem. B* , vol. 107, , p. 1033710340. , 2003,.

[233] E Spano, S. Hamad, and C. R. A. Catlow, "ZnS bubble clusters with onion-like structures.

," *Chem. Comm.* , vol. 7, , pp. 864-865. , 2004,.

[234] S. Pal, B. Goswami, and P. Sarkar, "Size-dependent properties of ZnmSn clusters: A density-functional tight-binding study.," *J. Chem. Phys.* , vol. 123, , p. 044311. , 2005,.

[235] S. Hamad, C. R. A. Catlow, E. Spano, J. M. Matxain, and J. M. Ugalde, "Structure and properties of ZnS nanoclusters. ," *J. Phys. Chem. B* , vol. 109, , p. 2703–2709. , 2005,.

[236] J. M. Matxain et al., "Electronic excitation energies of ZniSi nanoparticles. ," *Nanotechnology* , vol. 17, , p. 4100–4105. , 2006,.

[237] S. Pal, R. Sharma, B. Goswami, P. Sarkar, and S. P. Bhattacharyya, "A search for lowest energy structures of ZnS quantum dots: Genetic algorithm tight-binding study. ," *J. Chem. Phys.* , vol. 130, , p. 214703. , 2009,.

[238] S. Hamad, S. M. Woodley, and C. R. A. Catlow, "Experimental and computational studies of ZnS nanostructures. ," *Mol. Simul.* , vol. 35, , p. 1015–1032. , 2009,.

[239] C. R. A. Catlow et al., "Modelling nano-clusters and nucleation. ," *Phys. Chem. Chem. Phys.* , vol. 12, , p. 786–811. , 2010,.

[240] Y. Yong, X. Li, X. Hao, J. Cao, and T. Li, "Theoretical prediction of low-density nanoporous frameworks of zinc sulfide based on ZnnSn (n = 12, 16) nanocaged clusters. ," *RSC Adv.,* , vol. 4, pp. 37333-373411. , 2014,.

[241] S. Pal, B. Goswami, and P. Sarkar, "Size-Dependent properties of hollow ZnS nanoclusters ," *J. Phys. Chem. C* , vol. 112, , p. 6307. , 2008,.

[242] R. R. Zope, T. Baruah, M. R. Pederson, and B.I. Dunlap, "Electronic structure, vibrational stability, infrared, and Raman spectra of B24N24 cages. ," *Chem. Phys. Lett.* , vol. 393, , pp. 300-304. , 2004,.

[243] R. R. Zope, T. Baruah, M. R. Pederson, and B. I. Dunlap, "Theoretical infrared, Raman, and optical spectra of the B36N36 cage. ," *Phys. Rev. A* , vol. 71, , p. 025201. , 2005,.

[244] H. Behera and G. Mukhopadhya, "Tailoring the structural and electronic properties of graphene-like ZnS monolayer using biaxial strain.," *J. Phys. D: Appl. Phys.* , vol. 47, , p. 075302. , 2014,.

[245] C. Tusche, H. L. Meyerheim, and J. Kirschner, "Observation of depolarized ZnO(0001) monolayers: Formation of unreconstructed planar sheets. ," *Phys. Rev. Lett.* , vol. 99, , p. 026102, 2007,.

[246] J. P. Perdew, K. Burke, and M. Ernzerhof, "Generalized Gradient Approximation Made Simple. ," *Phys. Rev. Lett.* , vol. 77, , p. 3865. , 1996,.

[247] M. R. Pederson and K. A. Jackson, "Variational mesh for quantum-mechanical simulations. ," *Phys. Rev. B* , vol. 41, pp. 7453-7461. , 1990.

[248] M. R. Pederson and K. A. Jackson, "Pseudoenergies for simulations of metallic systems. ," *Phys. Rev. B* , vol. 43, , pp. 7312-7315. , 1991,.

[249] D. Porezag and M. R. Pederson, "Optimization of Gaussian basis sets for density-functional calculations. ," *Phys. Rev. A* , vol. 60, , pp. 2840-2847. , 1999,.

[250] D. Porezag and M. R. Pederson, "Infrared intensities and Raman-scattering activities within density-functional theory. ," *Phys. Rev. B* , vol. 54, , pp. 7830-7836. , 1996,.

[251] E. D. Glendening et al., *Theoretical Chemistry Institute; University of Wisconsin: Madison, WI, http://www.chem.wisc.edu/~nbo5 [Accessed 07 April 2017].*

[252] B. I. Dunlap and R. Taylor, "Octahedral C48 and uniform strain.," *J. Phys. Chem.* , vol. 98, , pp. 11018-1109. , 1994,.

[253] R. A. LaViolette and M. T. Benson, "Density functional calculations of hypothetical neutral hollow octahedral molecules with a 48-atom framework: Hydrides and oxides of boron, carbon, nitrogen, aluminum, and silicon.," *J. Chem. Phys.* , vol. 112, , pp. 9269-9275. , 2000,.

[254] R. R. Zope and B. I. Dunlap, "Electronic structure of fullerene-like cages and finite nanotubes of aluminum nitride. ," *Phys. Rev. B* , vol. 72, , p. 045439. , 2005,.

[255] T. Oku, A. Nishiwaki, I. Narita, and M. Gonda, "Formation and structure of B24N24 clusters. ," *Chem. Phys. Lett.* , vol. 380, , p. 620. , 2003,.

[256] M. -L. Sun, Z. Slanina, and S. -L. Lee, "Square hexagon route towards the Boron-Nitrogen clusters. ," *Chem. Phys. Lett.* , vol. 233, , pp. 279-283. , 1995,.

[257] P. W. Fowler and D. B. Redmond, "Symmetry aspects of bonding in carbon clusters - The leapfrog transformation. ," *Theor. Chim. Acta* , vol. 83, , p. 367. , 1992,.

[258] M. R. Pederson, A. Ruzsinszky, and J. P. Perdew, "Communication: Self-interaction correction with unitary invariance in density functional theory. ," *J. Chem. Phys.* , vol. 140, , p. 121103. , 2014,.

[259] M. R. Pederson, "Fermi orbital derivatives in self-interaction corrected density functional theory: Applications to closed shell atoms.," *J. Chem. Phys.* , vol. 4142, , p. 064112. , 2015,.

[260] M. R. Pederson and T. Baruah, "Chapter Eight-Self-Interaction Corrections Within the Fermi-Orbital-Based Formalism. ," *Adv. in Atom. Mol. Opt. Phys.* , vol. 64, , pp. 153-180. , 2015,.

[261] M. R. Pederson, T. Baruah, D.-Y. Kao, and L. Self-interaction corrections applied to Mg-porphyrin, C60, and pentacene molecules. Basurto, *J. Chem. Phys,* , vol. 144, p. 164117., 2016.

[262] C. Chang, A.B.C. Patzer, E. Sedlmayr, T. Steinke, and D. Sülze, "Computational evidence for stable inorganic fullerene-like structures of ceramic and semiconductor materials. ," *Chem. Phys. Lett.* , vol. 350, , p. 399. , 2001,.

[263] M. K. Y. Chan and G. Ceder, "Efficient Band Gap Prediction for Solids. ," *Phys. Rev. Lett.* , vol. 105, , p. 196403. , 2010,.

[264] H. Gurel, O. Akinci, and H. Unulu, "First principles calculations of Cd and Zn chalcogenides with modified Becke–Johnson density potential. ," *Superlattice Microst.* , vol. 51, , pp. 725–732. , 2012,.

[265] O. Zakharov, A. Rubio, X. Blase, M.L. Cohen, and S. G. Louie, "Quasi-particle band structure of 6 II-VI-compounds = ZnS, ZnSe, ZnTe, CdS, CdSe, and CdTe. ," *Phys. Rev. B* , vol. 50, , pp. 10780-10787. , 1994,.

[266] N. 1. Üzar and M.C. Synthesis and investigation of optical properties of ZnS nanostructures. Arikan, *Bull. Mater. Sci.* , vol. 34, no. 2), , pp. 287–292. , 2011,.

[267] M. R. Pederson and A. A. Quong, "Polarizabilities, charge states, and vibrational modes of isolated fullerene molecules. ," *Phys. Rev. B* , vol. 46, , pp. 13584-13591., 1992,.

[268] M. Cardona and G. Guntherodt, *Light Scattering in Solids*.. Berlin, : Springer-Verlag , 1982..

[269] M. J. Frisch, *Gaussian09, Revision E.01*. Wallingford, CT,: Gaussian Inc.: , 2009.

[270] A. Derré, C. Labrugère, M. Trinquecoste, P. Chadeyron and P. Delhaès. B. Maquin, "Submicronic powders containing carbon, boron and nitrogen: their preparation by chemical vapour deposition and their characterization," *Carbon,* , vol. 38, no. 1, pp. 145-156, 2000.

[271] H. Yasuda and H. Mori J. Huang, "Highly curved carbon nanostructures produced by ball-milling," *Chem. Phys. Lett.*, vol. 303, no. 1, pp. 130-134, 1999.

[272] J. Kitamura, S. Usuba, H. Yokoi, Y. Kakudate and O. Odawara A. V. Gubarevich, "Onion-like carbon deposition by plasma spraying of nanodiamonds," *Carbon*, vol. 41, no. 13, pp. 2601-2606, 2003.

[273] Po-Liang Liu and Jia-Yang Hong, "Double-shell C60/C240 fullerenes with Stone-Wales defects for hydrogen storage: An ab initio study," *JOURNAL OF APPLIED PHYSICS* , vol. 114, p. 114301 , (2013).

[274] Marco Olguin and Rajendra R. Zope, Tunna Baruah, "Charge transfer excited state energies by perturbative delta self consistent field method, ," *J. Chem. Phys. 137, 084316 (2012).*, vol. 137, no. 084316, 2012.

[275] M. J. et al. Frisch,. Wallingford, CT,: Gaussian Inc.:, 2009.

Publications/preprints

- Site specific atomic polarizabilities in endohedral fullerenes and carbon onions
  Rajendra R. Zope, **Shusil Bhusal**, Luis Basurto, Tunna Baruah, and Koblar Jackson
  The Journal of Chemical Physics **143**, 084306 (2015).
- Optical Properties of $VSc_2N@C_{68}$ Fullerene.
  Shusil Bhusal, Rajendra R. Zope, Surendra Bhatta, and Tunna Baruah;Electronic
  The Journal of Physical Chemistry **120,** 27813 (2016)
- Electronic and Structural Study of Zn_xS_x [x = 12, 16, 24, 28, 36, 48, 96, and 108] Cage Structures
  Shusil, Bhusal, Jose A. Rodriguez Lopez; Jose, Reveles; Tunna, Baruah; Rajendra, Zope.
  The Journal of Physical Chemistry **121,** 3486 (2017)
- Electronic Structure Calculation of Vanadium, Scandium Based Endohedral Fullerenes $VSc_2N@C_{2n}$(2n=70,76,78,80)
  Shusil Bhusal, Tunna Baruah, Yoh Yamamoto, and Rajendra R. Zope
  The Journal of Physical Chemistry Submitted on 22 November 2017
- Electronic structure, vibrational properties and charge transfer excitations in the carbon onion $C_{60}@C_{240}$
  Shusil Bhusal, Carlos Diaz, Tunna Baruah and Rajendra R. Zope
- Electronic Structure Calculation of Vanadium, Scandium Based Endohedral Fullerenes $V_2ScN@C_{2n}$(2n=70,76,78,80)
  Shusil Bhusal, Tunna Baruah, Luis Basurto, and Rajendra R. Zope

Vita

Shusil Bhusal was born in Arghakhanchi, Nepal. He is the youngest son of the Dharma Bhusal and Ganga Bhusal. He graduated from the high school in 2001. After that he joined the graduate school at Butwal Multiple College and graduated from Trichandra College KTM in 2004. In addition he got the Master's degree in Physics from the Tribhuvan University in 2006. He joined the University of Texas at El Paso as a graduate student in 2013 and graduated in MS physics in 2104. He continued his study as a PhD student in Materials, Science and Engineering program in UTEP from 2014, where he got a chance to work as a RA and TA.

Permanent address: 1627 Monte Del Sol
El Paso, TX, 79911

The author typed this thesis.